12-2019

Bioresorbable Composite Stents for Enhanced Response of Vascular Smooth Muscle Cells

Hozhabr Mozafari

Bioresorbable Composite stents for enhanced response of Vascular Smooth Muscle Cells

By

Hozhabr Mozafari

A DISSERTATION

Presented to the Faculty of

The Graduate College at the University of Nebraska

In Partial Fulfilment of Requirements

For the Degree of Doctor of Philosophy

Major: Engineering

(Materials Engineering)

Under the Supervision of Professor Linxia Gu

Lincoln, Nebraska

December 2019

Bioresorbable Composite stents for enhanced response of Vascular Smooth Muscle Cells

Hozhabr Mozafari

University of Nebraska, 2019

Advisor: Linxia Gu

Formation of arterial plaque and stenosis is one of the main cardiovascular disease risk factors. Stenting is a popular approach to increase the inner diameter of the artery and provide an acceptable lumen gain. This is achieved by applying internal pressure to the arterial wall. Despite the desirable outcomes of this procedure, there are complexities and challenges that are being discussed among scholars in this area. Restenosis is one of these complications, in which smooth muscles cell start proliferation and remodeling in response of induced mechanical stresses. Another important issue is the placement of the stent and possible migration due to the continuous deformation and special contact state between tissue and stent struts. Finally, the mechanical properties of the stent and application of novel materials in order to improve its performance are the critical topics that also have been elaborated in the current research work. First of all, we developed a multi-scale model which is able to calculate load distribution in RVE scale and can be useful to assess the mechanical stresses experienced by smooth muscle cells. Moreover, stent migration has been simulated by using finite element modeling, and the effect of stent structure on this complication has been explained. Finally, the application of novel nano composite materials in stent design has been discussed. Developing 3D printed steel-PLLA and Mg-PLLA particle composites and the effect of added phases in micromechanical properties of composites has been evaluated.

Table of contents

List of Tables

List of figures

Chapter 1: Introduction

1.1. Introduction

Cardiovascular disease (CVD) is defined as an inclusive term for several linked pathologies, commonly defined as coronary heart disease (CHD), cerebrovascular disease, peripheral arterial disease, rheumatic and congenital heart diseases and venous thromboembolism. Globally CVD accounts for 31% of mortality, the majority of this in the form of CHD and cerebrovascular accident [1].

According to the World Health Organization (WHO), over 75% of CVD is preventable (when they are at initial stages), however, aging effect, which is a well-known risk factor, causes an inevitable development of CVD [1].

Formation of arterial plaque and stenosis is one of the main CVD risk factors. It has been reported that severe stenosis is observable among large percentage of aging population particularly elderly people with diabetes, hyperlipidemia, aortoiliac occlusive disease, coronary artery disease, or hypertension. [2]. Stenosis is a progressive disease that may happen alone or in combination with other diseases such as hypertension and ischemic kidney disease [3]. Two common strategies to treat the patients with severe stenosis are aggressive medical therapy and using medical tools such as angioplasty and stenting methods [4]. The later one focuses on increasing the inner diameter of artery to provide an

acceptable lumen gain. The is achieved by applying internal pressure to the arterial wall by using inflating balloon or expanding stent.

Another complication with stenosis treatment procedure is the occurrence of restenosis. It has been reported that for coronary angioplasty the rate of restenosis is 30 to 60 percent, which can be categorized by two parts. The first part, recoil and remodeling of interior wall of the treated artery. The second part is called intimal hyperplasia, which is the proliferative response to injury and consists of smooth muscle cells and matrix formation [5]. It is reported that stents provide a luminal scaffolding that decrease recoiling which can reduce the risk of restenosis. However, placement of stent cannot prevent the proliferative behavior of restenosis components.

Restenosis is a vascular repair mechanism as a response to vascular injury caused by expansion of angioplasty balloon or stent. The process is governed by cells proliferation, migration, remodeling, and extracellular matrix secretion [6]. The term of arterial remodeling used to know as any variations in arterial wall structure. In normal arteries, remodeling is a homeostatic response to alteration in the blood flow and circumferential stretch to restore normal shear stress and wall tension. There are many studies on the effect of flow shear stress on remodeling, however, the effect of stretch and arterial expansion on remodeling in not very well understood [7]. It has been reported that endothelial disruption, fracture of internal elastic lamina, and dissection of the media might cause the initiation of restenosis. Formation of thrombus is the first step of restenosis in which Vascular Smooth Muscle Cells migrate, synthesis matrix and collagen, and promoting neointimal formation. The mechanism of this phenomenon is not clear yet. Mechanical response of VSMC, endothelial denudation, release of mitogens and cytokines from platelets are among the

suggested mechanisms for VSMCs migration and proliferation [8]. Mechanical load is an important modulator of VSMC morphology and function in many tissues, especially cardiovascular system. It is reported that VSMC hypertrophy and proliferation is related with high mechanical loads. However, in order to identify the contribution of arterial expansion of VSMC mechanical load, researchers must relate the stretch of tissue and deformation in micro scale [9]. Due to the difficulties with experimental methods, computational modeling can be used to study the effect of arterial expansion of VSMC loading. In the current research a micro-structure model of media layer is developed which can help the scientists to determine mechanical response of VSMC under arterial expansion. The model can be coupled with a macro scale model of artery and treatments such as angioplasty and stenting can be performed.

Another important point about stenting is the placement and stent migration. The movement of stent after placement can cause many problems. This late complication happens for esophageal and biliary duct stenting (0-40 %). In most cases, the stent dislocates naturally because of contraction and relaxation of tissue wall [10]. An example of this complication is esophagus stenting. Palliative treatment of malignant tumor or obstruction of the esophagus has been observed among aging population. Using self-expandable metal stents have been suggested to keep the tract open. However, the risk of migration due to the peristalsis movement of tract wall was high. Therefore, a new design with larger proximal ends was suggested to provide an anchoring effect. The design focused on the inducing sufficient radial force. On the other side, high mechanical stresses can cause restenosis and tissue injury. Therefore, a study is needed to correlate the stent

design and induced reaction forces in tract wall, which will be helpful for designers and clinicians to come up with optimum stent structures [11].

The last but not the least topic that will be covered in this research work is the novel material application for stent design. By introduction of composite materials, at least two different materials could combine and make a novel material which benefits from the characteristics of each constituent. A composite material basically consists of a matrix and a filler phase which can come with different shapes such as long fibers, short mat, and particles [12]. Depends to the size of filler the resulted composite can be classified as a nanocomposite. In this work the application of nanocomposite as a suggested material for stents is discussed.

Chapter 2: Migration resistance force of Esophageal Stents: the role of stent design

2.1. Introduction

Esophageal cancer (EC) is the sixth most common cancer and rarely curable with high morbidity and mortality all over the world [13]. Mostly, the patients suffering from EC are diagnosed at later or advanced stage, which are unfavorable for surgical resection. The survival rate of patients accepting surgical resection is poor with a 5-year survival of 15–34% [14]. Moreover, palliative care of serious illness like malignant stricture is to relieve the symptoms but unable to inhibit the tumor cells, which is the prime concern in curing EC [15]. Stent, a mesh structure serving as a scaffold to open the palliate esophageal stricture and relieve dysphagia, is becoming a common EC treatment option for improving the quality of life of patients[16]. Various self-expanding metal stents have been developed for this purpose. Major complications include stent migration, tumor ingrowth, and tissue perforation [17, 18]. Homann et al. [19] investigated 164 self-expanding stents implanted in malignant strictures of the esophagus or the esophagogastric junction, and observed more stent migration and fewer food impactions in patients implanted with covered stents than with uncovered ones. Most existing efforts focus on the covered materials [20] and their anchoring technique [21]. For example, the endoscopic clip at the upper flare of the covered esophageal stent was considered as one promising means to reduce stent migration [21].

The stent shape was also considered as an important factor influencing stent migration. The most common implementation in the design of esophageal stents was the relatively

wider proximal and distal ends, which were used to increase the radial force and reduce the risk of stent migration [22]. Sharma et al. [23] have conducted a critical review of the efficacy of esophageal stents and implied that the underlying mechanism of stent migration and tumor in-growth could be clarified quantitatively. Kajzar et al. [24] illustrated the mechanics of the a stent-esophagus system with focus on the crimping and expansion of esophageal stent. Even though Park et al. [17] classified four levels of stent migration in patients with malignant esophageal stricture, the underlying mechanisms of stent migration away from the esophageal stricture, especially the initiation process, remained unclear. Moreover, the quantitative study of stent-esophagus interaction for evaluating stent migration was lacking [25], nonetheless computational modeling of stents has been extensively used for design and analysis [26-29]. Specifically, layered esophageal wall were modeled to illustrate the mechanics of the gastroesophageal junction [30] and the interface mechanics between the muscle layer and the mucosa–submucosa layer [31].

The goal of this work is to characterize the interactions between the stent and esophagus, to shed light on the mechanism of stent migration as well as to design better esophageal stents. We utilized the finite element approach to depict and compare the mechanics of the esophagus with a malignant stricture, after implantation of self-expanding nitinol stents, with and without flared ends. After stent deployment in the esophagus, the lumen gain, strut malapposition, Von Mises stress distributions on the wall of the esophagus, and radial contact force between the stent and esophagus were evaluated for both stents. Moreover, both stents were pulled longitudinally at one end to mimic the worst-case scenario for stent migration. The dynamic sliding forces versus the stent displacement

were monitored. The obtained results might lead to better design of the next-generation esophageal stents with reduced migration rates.

2.2. Materials and Methods

A three-dimensional geometry of the WallFlex stent (Boston Scientific, Massachusetts, USA) with and without flared ends was constructed as shown in Figure 2-1. For the stent without flared ends, the total length was 100 mm and the outer diameter was 18.22 mm. For the flared stent, the middle section had the same diameter as the straight stent with a length of 64 mm, while the flared ends had a diameter of 24.22 mm with a length of 9 mm at each end. Both esophageal stents were braided using 28-strand of wires with the diameter of 0.4 mm and pitch angle of 45º [23].

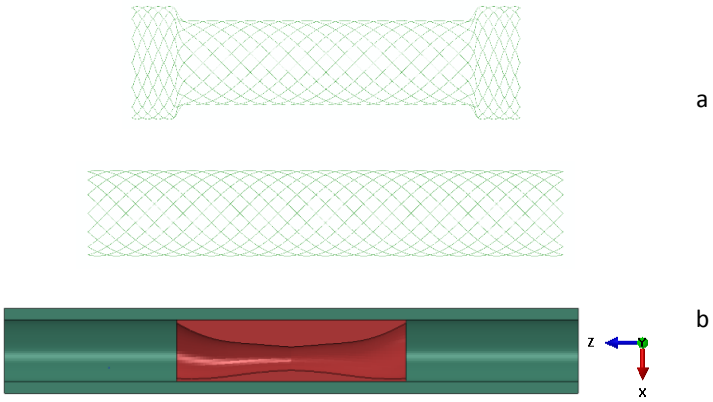

Figure 2-1 (a) Configurations of the flared stent and straight one; (b) Tumor restricted Esophagus.

The esophagus was assumed to be a uniform cylinder with a length of 150 mm, an inner diameter of 16 mm, and a wall thickness of 3 mm [25]. The simplified esophagus tube has been used for understanding the food transport [32], and stent-esophagus system [24]. The eccentric-shaped tumor with a maximum thickness ratio of 2:1 spanned across the 60 mm

of esophagus and resulted in a minimum lumen diameter of 6 mm, i.e., a diametrical stenosis ratio of 62.5 % (Figure 2-1b). The tumor length was shorter than the middle section of the flared stent, and this warranted the same stent-tumor interactions for both stent deployments. After preliminary simulations, we constructed half of the model by applying symmetry boundary conditions along the z plane (U_z=UR_x=UR_y=0) in order to reduce the computational time.

The stent was made of nitinol which underwent phase transformation between austenite and martensite during one loading cycle [33]. The superelastic behavior of shape memory alloys can be simply understood as the phase transformation of austenite and martensite under stress. Based on free energy function and dissipation potential, the model is assumed that there is a relationship between the martensitic constant ϕ_M and the austenite constant ϕ_A:

$$\phi_M + \phi_A = 1 \tag{1}$$

The elastic modulus of Nitinol can be represented as a linear function of martensite volume fraction

$$E_f = \phi_M E_M + (1-\phi_M) E_A \tag{2}$$

where E_f , E_M and E_A are the elastic modulus of alloy, martensite and austenite, respectively.

The stress-strain relation is given according to the generalized Hooke's law as follows:

$$\sigma_f = C_f(\varepsilon - \alpha(T - T_0) - \varepsilon_{tr}) \tag{3}$$

where ε is the total strain the SMA, T_0 is the reference temperature, ε_{tr} is the phase transformation strain, α is the thermal coefficient, σ_f and C_f are the stress and elastic tensor, respectively. Therefore, an incremental constitutive law can be expressed as:

$$\Delta\sigma_f = C_f(\phi_M)(\Delta\varepsilon - \alpha(\phi_M)\Delta T - \omega\Delta\phi_M) \tag{4}$$

The main parameters of the constitutive model of nitinol alloy under isothermal conditions were listed in Table 2-1 [34]. The constitutive model was implemented through a built-in ABAQUS user material subroutine (UMAT) [35].

Table 2-1 Material constants of Nitinol

Property	Value	Definition
E_A	50 GPa	Austenite elasticity
E_M	37 GPa	Martensite elasticity
σ_M^s	400 MPa	Starting transformation stress of loading
σ_M^f	650 MPa	End transformation stress of loading
σ_A^s	350 MPa	Starting transformation stress of unloading
σ_A^f	80 MPa	End transformation stress of unloading
ε_L	0.055	Maximum residual strain

The hyperelastic behaviors of the tissue, including both esophagus and tumor, were adopted from the published experimental datasets [34, 36], which were fitted using the reduced polynomial constitutive equation below:

$$U = \sum_{i,j=1}^{3} C_{ij}(I_1 - 3)^i(I_2 - 3)^j \tag{5}$$

where, I_1 and I_2 are the first and second invariants of the Cauchy-Green tensor and

$$I_1 = \lambda_1^2 + \lambda_2^2 + \lambda_3^2 \quad (6)$$

$$I_2 = 1/\lambda_1^2 + 1/\lambda_2^2 + 1/\lambda_3^2 \quad (7)$$

The obtained material coefficients C_{ij} are listed in Table 2-2.

Table 2-2 Material coefficients of both esophagus and tumor (units:MPa) [35]

Esophagus (Based on the axil testing of mucosa)	C_{10} = -0.0268 C_{01} = 0.0479 C_{20} = 0.81218 C_{11} = -1.7233 C_{02} = 0.98173
Tumor	C_{10} = 0.039 C_{20} = 0.0031 C_{30} = 0.02976

The stent crimping process was simulated by applying radial inward displacement on the outer surface of the stent. The self-expanding process was captured by removing the displacement constrains. No relative movement between braided wires was allowed to mimic the role of the cover on the stent. The residual stresses of the esophagus tissue under physiological loading conditions were not considered for this comparative study [37]. The friction coefficient of 0.1 was adopted for the contact between the stent wires and tissues [38]. The mesh convergence study was conducted, and the esophagus and tumor were

meshed with 125,000 and 21,456 elements (C3D8R), respectively. The stent was constructed by 11,200 B31 elements which are two-node elements with one integration point in the middle and have been used for modeling of stents [39, 40].

Following the stent deployment in the esophagus, a longitudinal displacement of 60 mm was prescribed on the left end of the stent till it slid through the esophagus. The required sliding force during the sliding process was monitored.

2.3 Results

2.3.1 Interactions among stent, tumor and esophagus

Stent lumen enlargement and stress distribution are shown in Figure 2-2. The minimal lumen diameter increased from 6 mm to 17.15 mm and 16.91 mm for the flared stent and straight one, respectively. The stent ends resulted in an increased lumen diameter from 16 mm to 24.09 mm and 18.06 mm for the flared stent and straight one, respectively. The incomplete stent strut apposition, also referred to as malapposition, was characterized by the area of the non-contact region between the stent and tissue. The malapposition area was 532.80 mm^2 and 171.04 mm^2 for the flared stent and the straight one, respectively. The corresponding maximum gap between the stent and the tissue was 2.29 mm and 0.746 mm for the flared and straight stents, respectively. It is clear that the flared stent induced more malapposition compared to the straight one.

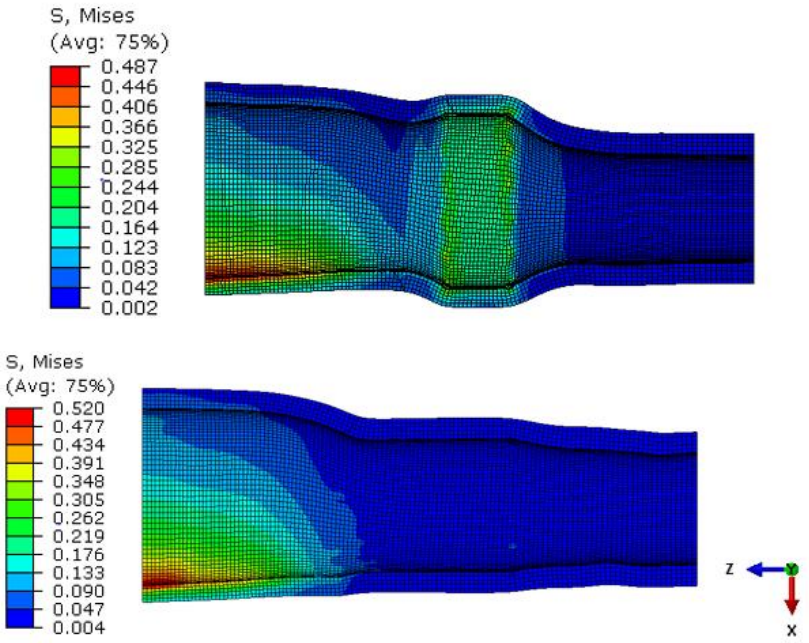

Figure 2-2 Stress distribution on the esophageal wall induced by flared stent or (top) or straight one (bottom).

The critical point based on Von Mises stress in the esophagus was located in the middle of the tissue, specifically at the narrowest lumen region, regardless of stent designs. The peak stress on the esophageal wall was approximately 520 kPa induced by the straight stent and 530 kPa by the flared stent. The stress distributions on the middle region of the stented esophagus were similar for both stents. However, the Von Mises stress at the flared-end region was up to 410 kPa, which was much higher than that induced by the straight stent. The peak stress of esophagus were within the reported ultimate tensile strength of muscle layer, i.e., 425-530 kPa [41].

2.3.2 Migration dynamics

The dynamics of stent migration were studied by pulling both expanded stents out of the esophagus as illustrated in Figure 2-3. The anchoring effect of the flared end and

straight one is demonstrated using snapshots. As the right end of the stent was about to pass the narrowest tumor location, the maximum pulling force, also referred to as the migration resistance force, occurred for both stents. Afterward, a decline in the magnitude of force was observable when the stent was leaving the tumor region.

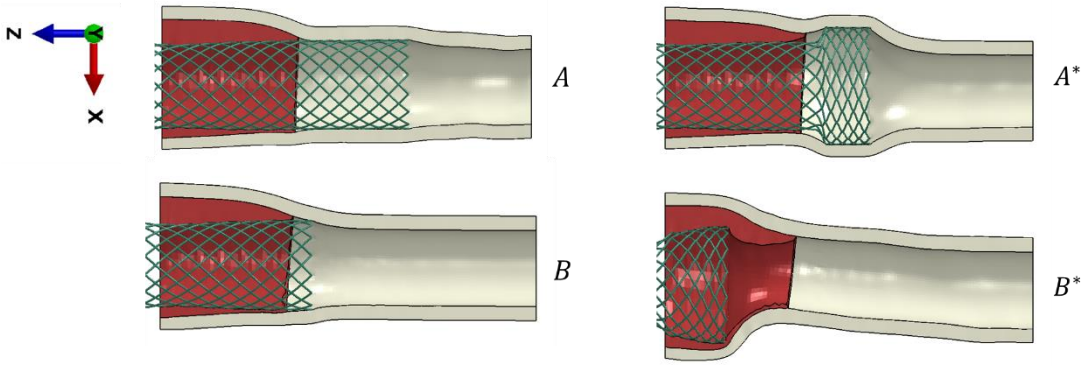

Figure 2-3 Snapshots of pulling both (a) flared stent and (b) straight stent, representing the initial configuration (A and A*) and peak resistance force (B and B*)

During the pulling, the contact forces at the stent-tissue interface were monitored as shown in Figure 2-4. The contact force here excluded the middle section of both stents with a length of 64 mm due to the minimal variations between stents. Clearly, the flared ends induced a higher contact force than the straight one. Before the stent migration initiated at 0.04 s, the contact forces were 31.5 N for the flared stent and 6.6 N for the straight one. The pulling motion dramatically increased the corresponding contact force up to 741 N and 273 N, respectively. Considering the flared end was only half the length of the straight one, the flared end design boosted the contact even more. The higher contact force implied a larger migration resistance potential.

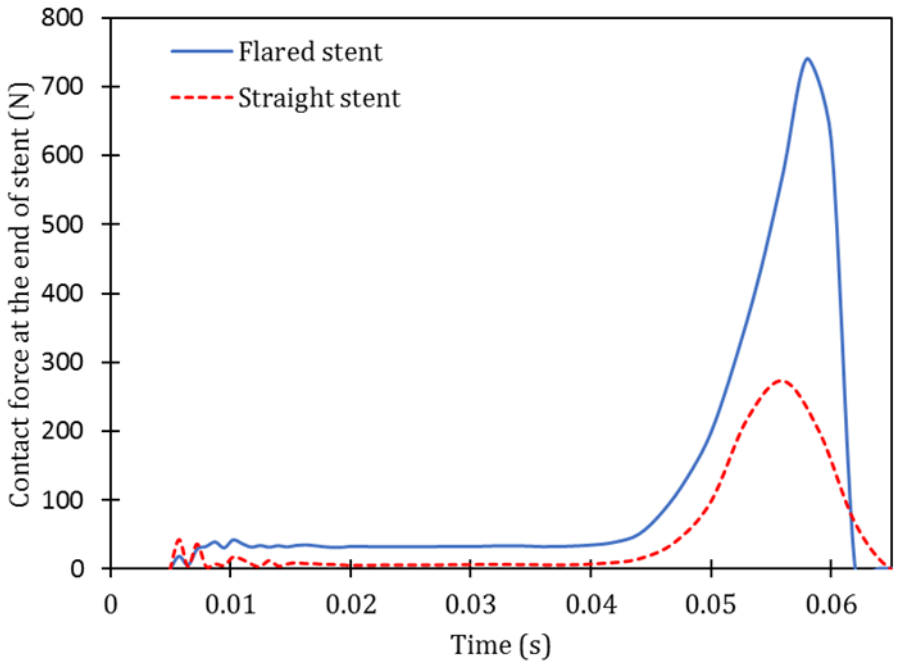

Figure 2-4 Contact force time history for both flared and straight stents.

Figure 2-5 depicts the migration resistance force during the pulling process. The flared stent exhibited a sharp increase in the migration resistance force. After reaching the peak magnitude, i.e., overcoming the tumor edges (Figure 2-3), an abrupt decline in resistance force was observed. The uniformity of the straight stent resulted in the gradual change in the migration resistance force. In addition, the peak migration resistance force for the flared and straight stents were 535 N and 310 N, respectively. This indicated that the required axial load to move the flared stent through the esophagus is 72.5 % higher than that for the straight stent. In addition, the anchoring effect could be calculated as the elastic strain energy, which was 9 J and 4.8 J for the flared and straight stents, respectively.

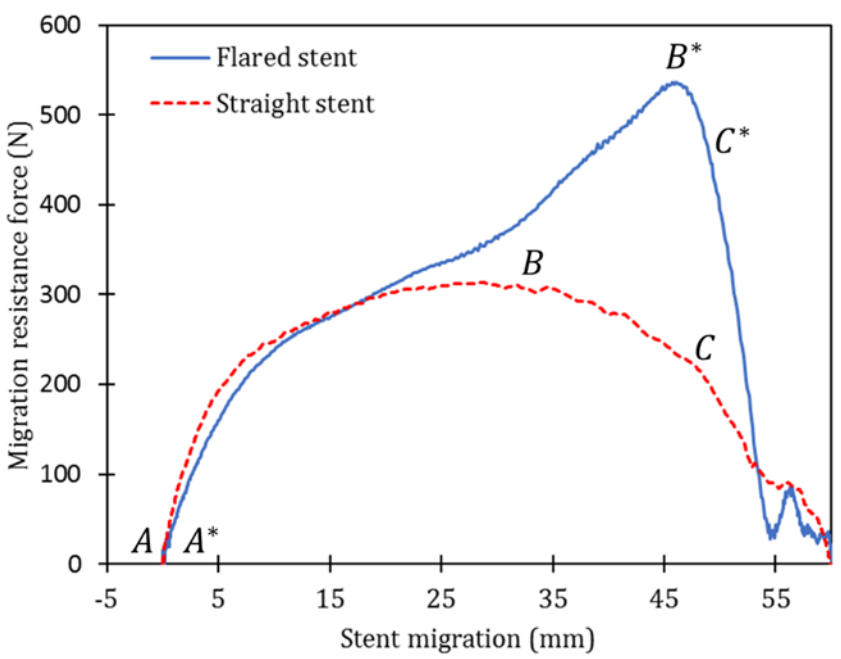

Figure 2-5 The migration resistance force in relation to the migration distance of stents.

The role of the nitinol wire diameter and the friction coefficient between stent wires and tissue on the migration resistance force were depicted to facilitate a better design of the stents (Figure 2-6). The wire diameter impacted the migration force dramatically. Specifically, the migration resistance force of the stent with a wire diameter of 0.6 mm was 834 N which is 56.5 % and 164 % greater than that for the stents with wire diameters of 0.4 mm and 0.3 mm, respectively. Moreover, the peak migration force was delayed with a thinner wire. This could be explained by the rigidity of the stent, which was reduced with a thinner wire.

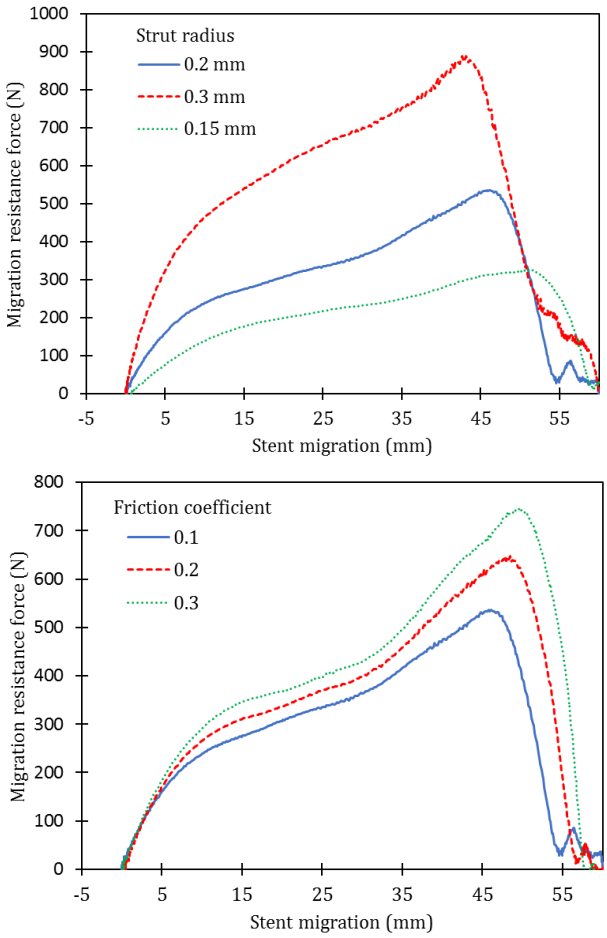

Figure 2-6 The migration resistance force of the flared stent in response to the wire diameter (Top) and the friction coefficient between stent wires and tissue (bottom)

The friction coefficient between the wires and tissue also influenced the migration risk of the stents. The migration resistance responses demonstrated the same trend. The maximum migration resistance forces for the friction coefficients of 0.1, 0.2 and 0.3 were 535 N, 639.42 N and 741.91 N, respectively. A larger friction coefficient of 0.3 caused 38.67 % enhancement of the migration resistance force, compared to the coefficient of 0.1.

2.4 **Discussion**

Esophageal stent insertion provides a substantial advantage in the management of dysphagia in patients with malignant esophageal obstruction. However, stenting complications compromise the quality of the patient's life. Stent migration is one of the major complications associated with esophageal stent implantations [42-44]. Figure 2-7 illustrates that the esophageal covered stent migrated downward 1 cm after 20 days of placement for treating the gastroesophageal anastomotic fistula of a 65-year old male patient. The informed consent was obtained from the patient to showing the image, which was achieved from digital subtraction angiography (DSA) during stenting procedure. Despite the extensive clinical observations regarding esophageal stent complications, there are limited studies on the mechanistic understanding of stent migration.

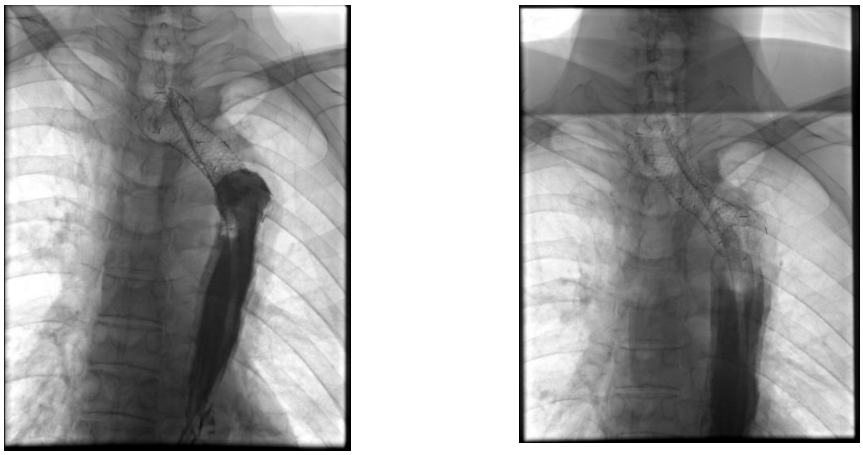

(a) **(b)**

Figure 2-7 Digital subtraction angiography of the esophageal stent placement (a) and migration down 1cm after 20 days (b).

This motivated us to test the role of flared ends, braided wire diameter, and the friction coefficient between wires and tissue on stent migration. We utilized the finite element

method, which has the advantage of replicating the physical problems with low-cost complex geometry, compared to both experimental tests and analytical methods. Experimental tests are usually expensive to conduct and difficult to isolate specific parameters. Analytical methods are limited to idealized geometries and boundary conditions. In this work, we have constructed finite element models to simulate the deployment of stents in the esophagus and then applied axial loading to characterize the migration risk of the stents.

Our modeling framework was validated against the published experimental data of a braided self-expandable Wallstent (Boston Scientific, Natick, MA) by Jedwab and Clerc [45]. The aforementioned modeling techniques were used to construct a braided Wallstent with a nominal length of 87.5 mm, braiding strand number of 24, braiding angle of 30.85^{o}, strand diameter of 0.22 mm, and outer diameter of 17.15 mm. The stent was made of Cobalt-Chromium-Nickel (Co-Cr-Ni) alloy with a Young's modulus of 206 GPa, shear modulus of 81.5 GPa, and yield strength of 2.5 GPa. Our simulation of the axial tension of the stent agreed very well with the experimental and theoretical data. Following the validation, our models could be used to delineate the interaction between the stents and tissue and to predict the tendency of stent migration.

Our results have demonstrated that the flared ends induced a much larger radial contact force (Figure 2-4). Following stent deployment, the contact force of the flared ends was 4.77 times more than that of the straight ones. The contact force of the flared ends per unit length was 9.54 times larger than that of the straight ones. This could be explained by the overstretch of the esophageal wall at the flared ends. This implied that the flared ends serve as anchors to maintain the deployment location and mitigate stent migration. However,

larger contact force led to higher stresses on the esophageal wall for both stents. This might cause the esophagus damage and failure. Stavropoulou et al. [46] studied the failure criteria for mucosa-submucosa and muscle layers of esophagus. The ultimate tensile strength of mucosa-submucosa and muscle layers were reported as 1149 kPa and 425-530 kPa, respectively. The stronger mucosa-submucosa layer was associated with its higher collagen content. The higher peak stress of esophagus induced by flared stent could lead to a higher probability of tissue failure.

The esophageal contraction is usually preceded by a transient variation of pressure in radial and longitudinal directions. This may represent tongue or laryngeal movement or changes in respiration coincident with the initiation of the swallow [47]. Even though the peristaltic contraction was essential for bolus transport through esophagus tube [48, 49], it could be simplified as the axial pulling of the stent through the esophagus for the comparative study of the migration risk.

During the pulling of the stents, much more work was required to initiate the sliding of the flared stent than the straight one (Figure 2-5). In addition, the straight stent sliding initiated gradually, and the flared stent exhibited a sharp resistance force with a larger magnitude. Again, this was due to the anchoring effect of the flared ends.

Our results provided the quantitative datasets for better understanding the observations in both clinical trials and animal studies. Els et al. [44] examined 46 patients and found that flared stents mitigated stent migration. A rabbit study also demonstrated that a flared prostatic stent helped to reduce migration compared to its straight counterpart [50].

Various sizes of wires have been used to braid the stent. Our results have shown that a doubled wire diameter increased the migration resistance force by 1.64 times. This indicates that a thicker wire for the stent could be adopted for reduced probability of migration. This could be explained by increased stiffness of the stent as fabricated using thicker wires.

We also tested how the friction coefficient between stent wires and tissue affects the migration resistance since this coefficient was rarely reported. Usually an assumed value was adopted [25]. It was found that the friction coefficient has a impact on the risk of stent migration. If we tripled the friction coefficients, the peak migration resistance force was 38.67 % larger. This indicated that the surface treatment of the stent wires, or struts, for increasing the friction coefficient, could also prevent the risk of stent migration.

In the present model, the relative movement of the braided wires was constrained to mimic the covering effect commonly used in commercial esophageal stents. The anatomical details of the esophagus including the stellate appearance of the inner esophageal layer [25] was simplified as an esophagus tube with a friction coefficient. A range of friction coefficients were used depending on relative movement between the stent and the esophageal wall [22]. A larger friction coefficient was commonly associated with the less migration risk. The feasibility of the model was validated in our previous work [51, 52]. The esophagus was modeled as a one-layer tube [24, 53], although it is assumed as two layer [54, 55] or three layer wall [56] depending on the aim of the study. The detailed configurations of esophageal wall could alter our results in terms of magnitudes, but the comparative results between two stent designs was expected to be the same. The material properties of the esophagus and cancerous tissue were assumed to be homogeneous

isotropic materials, although they are anisotropic [57]. The perfect plasticity for cancerous tissue was assumed due to lack of experimental data. More realistic models considering patient-specific geometry and anisotropic three-layered esophageal wall properties would change the contact force and the migration resistance force. The existence of pre-stretch along axial and circumferential directions at physiological conditions [37] as well as the esophageal muscle contraction were not explicitly incorporated in our model, we speculate that the both pre-stretch and wall contraction were associated with the reduced friction between stent and esophagus, and thus a higher migration rate. Despite these simplifications, this work demonstrated the importance of the stent design on the risk of migration, which might have significant clinical implications. This work could be used to provide a fundamental understanding of the behavior and impact of stent design on the esophageal wall, provide guidance for optimizing stent shape and surface profiles, and illuminate the possibilities for exploiting their potential to prevent migration.

Chapter 3: Mechanical contribution of vascular smooth muscle cells in the tunica media of artery

3.1 Load bearing filaments in VSMC cytoskeleton

The cytoskeletal of vascular smooth muscles encompasses filaments and organelles. The density and number of these components can vary with respect to different internal and external signals [58, 59]. The filaments inside cytoskeleton can be classified as actin stress fibers (SFs), microtubules (MTs), and intermediate filaments (IFs), as shown in Figure 3-1.

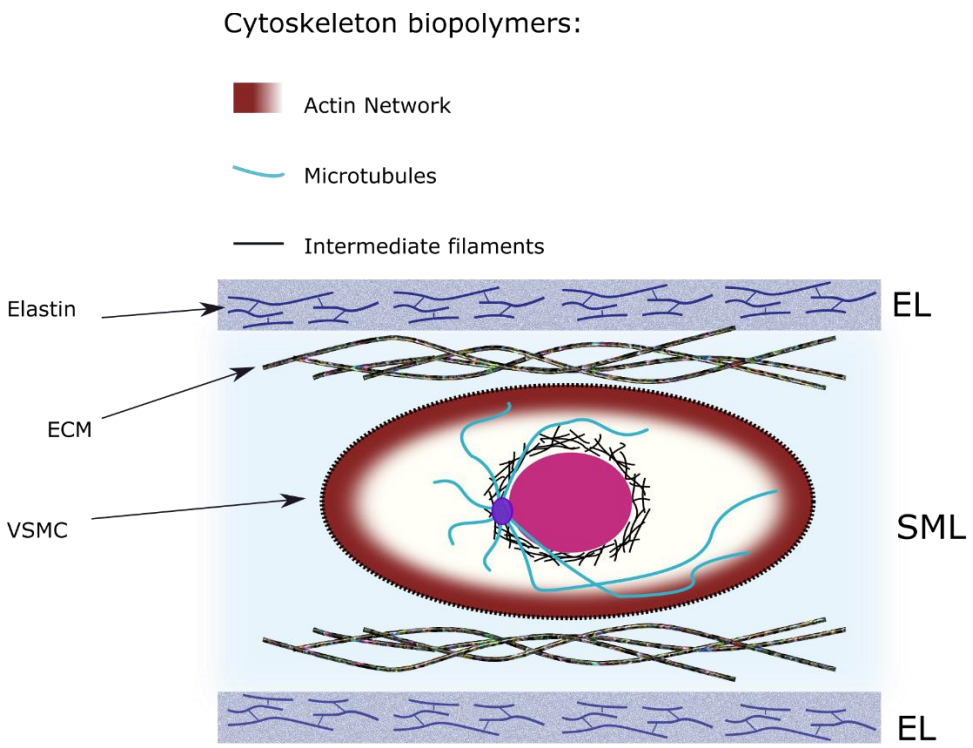

Figure 3-1 Cytoskeleton structure of the cell and the load carrying fibers

These filaments play a principal role in the mechanical properties of vascular smooth muscle cells including proliferation [60], differentiation [61, 62], cell migration [63], and

apoptosis [64, 65]. Therefore, mechanical properties of these fibers are critical for the deformation and stability of vascular smooth muscle cells.

3.1.1 Stress fibers (SFs)

It has been reported that stress fibers (SFs), which mainly aligned in major axis of the cell, are the principal contributor to contractile forces through actomyosin activation [66]. Deguchi et al. [67] performed tensile tests of SFs by isolating these fibers from cultured bovine VSMCs. Each SF is composed of a bundle of actin filaments (AFs). These bundles are held together by the actin-crosslinking protein α-actin. The elastic modulus of SFs was approximately 1.45 MPa which was three orders of magnitude lower than that of single AF (1.8-2.6 GPa) [68]. On the other hand, the breaking force of single AF was determined to be 600 pN, whereas the breaking force of a single SF is approximately 380 nN, i.e., 600 times higher. In addition, the stress-strain relation was linear for the single AF, although SFs exhibited a highly non-linear strain-induced hardening behavior [69]. Cell contraction is based on two vital structures, SFs and focal adhesion sites. Rho GTPase promotes the formation of SFs and cell adhesion sites, resulted in higher contractility [70]. It is reported that the tension applied to focal adhesions increased from 10 nN to 100 nN upon contraction of the VSMCs [71]. Moreover, disruption of SFs during the tensile tests decreased the cell's stiffness by 50 % [72].

3.1.2 Microtubules (MTs)

Microtubules (MTs) have a cylindrical shape with inner and outer diameters of 14 and 25 nm [73]. MTs are rigid filaments with bending stiffness of 100 times higher than that of AFs and with elastic modulus of 1.2 GPa [74]. MTs have a remarkable contribution in stabilization of cells elongation through attaching to the cell membrane via certain capping

proteins [75]. The contribution of MTs on cell locomotion and migration by regulating of actin polymerization has been reported [76]. Kato et al. [77] showed that tracheal fusion cells form polarized microtubule bundles oriented towards the leading edge of migrating cells. The function of these microtubules is twofold: to concentrate E-cadherin to the newly contacted cell interface and to initiate the formation of new adherent's junctions. Microtubule depolymerization enhances isometric contraction of vascular smooth muscle cell, which is not receptor dependent [78]. Besides the principal contribution of SFs in contractility and MTs in migration, MTs are acknowledged to indirectly affect the contractility of VSMCs. Specifically, MTs growth favors dissolution of focal adhesions, whereas disruption of MTs leads to enhanced cell contractility by formation of SFs and focal adhesions [79]. In addition, disruption of the MTs decreased the tensile stiffness of VSMCs by 30 % at large strain levels. Insignificant contribution of MTs was observed under small tensile strain which stem from wavy morphology of these fibers [72].

3.1.3 Intermediate filaments (IFs)

The intermediate filament (IF) network is one of three cytoskeletal systems. IFs are widely distributed from the plasma membrane to nucleus, providing mechanical and structural integrity for the cell [80]. In conjunction with associated proteins, IFs generate networks that serve to generate and support cell shapes. Spatial reorganization of IFs along with the development of SFs make VSMCs able to adjust their contraction/relaxation states. Moreover, the dynamic IFs play a crucial role in regulating various cellular functions including signal transduction; tension development; cell division and migration [81]. The IFs, with the diameter of approximate 10 nm, have been grouped into five types, or sequence homology classes (SHC), on the basis of amino-acid-sequence identity [82]. The

most prominent IFs in VSMC cytoskeleton is vimentin, which forms a dynamic network and varies during contraction [83]. The elastic modulus of IFs has been reported in the range of 300-900 MPa [84]. The contribution of IFs in tensile properties of SMCs is remained to be determined even though IFs play important roles in tensile properties of the cells during large deformation [85]. Green et al. [86] speculated that it is impossible to disrupt IFs themselves due to the interaction between IFs and AF structure.

Although the characteristics of each filament in the VSMCs cytoskeleton has been studied separately, the intracellular force balance, contraction, and cell stiffness are strongly influenced by the interaction of cytoskeleton with extracellular matrix (ECM) and signaling pathways as described below.

3.2 Interaction of VSMCs within the extracellular matrix (ECM)

Structural constituents of ECM, that regulate its passive mechanical behavior, are elastin fibers, collagens, and glycosaminoglycans (GAGs) [87]. Interaction of these structural constituents and VSMCs can trigger significant variations of stiffness of both ECM and VSMCs. The adhesive glycoproteins fibronectin and laminin form connections between ECM and VSMCs via specific integrin receptors. Fibronectin is a multifunctional adhesive protein present in the plasma and also synthesized by vascular cells [88]. VSMCs express both β-1 and β-3 integrins and [89] demonstrated greater functional significance in adhesive processes of β-3 integrin essential for SMC migration. On way to study the interaction between VSMC (and other cells in general) and ECM is to culture the cell on substrate and study the deformations under different circumstances [90]. Adhesion rate, spread area, cytoskeletal assembly, and focal adhesion signaling was evaluated by culturing VSMCs on substrates with different stiffness and coated with fibroactin- or laminin- [91].

When VSMCs were cultured on fibroactin substrates with varied mechanical gradient, it was found out that cells preferentially migrate toward stiffer regions [92, 93]. On the other side, Hartman et al. [94] observed the migration of VSMCs toward the stiffer region of gradient substrate coated with fibroactin, whereas the migration on laminin-coated gradient substrate appeared to be random. This observation indicated that the deformation and migration of VSMCs are not only dependent on the stiffness of ECM but also the type of interacting proteins and the engaged integrins [91].

The ECM stiffness can also affect the phenotype of VSMCs [95]. A stiffer ECM led to synthetic phenotype in the VSMC. Specifically, the VSMC decreases the number of cytoskeletal filaments and exhibits lower stiffness than that of contractile phenotype. Fibronectin drives cells away from the contractile phenotype *in vitro*, whereas laminin has been shown to conserve it [96]. Cell culture in 2D has been widely used to study the mechanotransduction of VSMCs due to ease of handling, maintenance, and application of mechanical loads [97-99]. However, culturing cells on a 2D substrate affects the cellular deformation, adhesion force and stiffness. To address this issue, engineering 3D gels [100] or scaffolds [101, 102] as the cell culture environment has been suggested.

Artery and its cellular components are continuously exposed to hemodynamic stimuli including cyclic strain, flow shear stress, and blood pressure [103, 104]. These mechanical loadings correlated with VSMC behaviors, ECM remodeling, and vasoregulation [105]. Cyclic mechanical stimulation possesses dual effect on proliferation of VSMC [106], enhance the collagen production [107], and increases the capability of transformation from synthetic SMC phenotype into contractile phenotype [108]. A cyclic tensile strain of 5% reduced SMC proliferation [109]. Conflicting variation of VSMCs phenotype with respect

to the level of cyclic loading has been reported [110], whereas over-expression of contractile phenotype proteins has been observed [111-115]. Solan et al. [116] showed that cyclic strain had a direct impact on increasing collagen content and organization in ECMs. Bono et al. [117] studied the effects of cyclic strain (7%) on the VSMCs behavior which were cultured on 2D substrates and in 3D matrix composed of type I collagen. It was demonstrated that in the 3D culture environment there are more VSMCs aligned in the direction of strain (nearly 60 %). Additionally, the level of SM α-actin in VSMCs cultured in the 3D collagen matrix was higher than that cultured on the monolayer 2D substrate. This research indicated that in 3D culture environment and under cyclic loading the density of contractile proteins inside VSMC's cytoskeleton increases remarkably. It is worth mentioning that in the cardiac cycle VSMCs are cyclically stretched by ~ 10 % with a 25-50 % mean strain, and their mechanical properties should be evaluated over a large range of deformations [118].

It was noted that the ECM mechanical properties including its heterogeneity are the key factors to impact the 3D VSMC contractility [119]. Novel hydrogels have been developed to resemble the composition of ECM and thus *in vivo* mechanical environment [120, 121]. Ding et al. [122] developed a biomimetic fibrous hydrogel with tunable structure and stiffness. The developed ECM array consisted of collagen I, III, IV, fibroactin, and laminin. The effect of ECM deposition and stiffening during vascular disease progression on VSMCs contraction/relaxation was investigated. Although, the developed hydrogel encompassed the composition of ECM components, the challenges lie in the control of the architecture and alignments of collagen fibers. It has been illustrated that fibers orientation affect their load sharing contribution to the media tunica [123]. Phillippi et al. [124]

reported that a remarkable variation of collagen fiber orientation distribution exists in the diseased aortic media. Considering the limitation in reproducing a complex *in vivo* ECM environment, the load sharing of VSMCs with respect to these structural components of ECM remained to be explored.

3.3 **Arterial constituents**

The artery wall exhibits three major layers: Intima, media and adventitia. The intima layer is predominantly populated with endothelial cells (ECs), which synthesize proteins, such as collagen IV and laminin, to create basal lamina. Its main function is to transmit signals that control vascular tone. It has a minimal contribution to the artery's mechanical properties. The adventitia mainly consists of fibroblast and a collagen-rich ECM. Adventitial fibroblasts respond to a variety of chemical and mechanical cues. For example, hypertensive environments result in increased fibroblast proliferation and collagens I and III synthesis. Adventitia bears over half of the load at abnormal pressure due to collagen's role as structural reinforcement [125]. The media is the thickest layer, between the intima and adventitia layers. It serves as the primary load bearing components. The media are composed by multiple lamellar units (LU), which consists elastic lamellae encompassing smooth muscle cells (SMC), interposed with collagen fiber network, as shown in Figure 3-1.

The LU was comprised of approximately 29% elastin, 24% SMCs, and 47% collagen and ground substance [126]. The volume of a single medial SMC was 1630±640 μm^3. The healthy aortic media SMC was in the shape of ellipse. The average length of minor and major axis is 3.1±0.8μm and 19.0 ±3.3μm, respectively. The average aspect ratio, i.e.,

major/minor axis is 6.2±1.4. At the relaxed state, the elastic modulus of the rat aortic VSMC (same microstructure with human's artery) in the major and minor direction is 14.8 KPa and 2.8 KPa, respectively [127]. Upon contraction, the elastic modulus in major and minor direction is 88.1 KPa and 59 KPa, respectively. The average density of SMCs within the media is $3.7\pm0.6 \times 10^5$ cells/mm^3 [126]. Between lamellae, the major axis of each nucleus aligned in the circumferential direction with a 19±3° radial tilt, resulting in cytoplasmic ends directed toward top and bottom of the lamellae. Collagen type I is the most abundant within blood vessels and had been proposed as the primary determinant of tensile properties [128]. Collagen was organized as bundles of fibers (numbering 24 ±15 fibers per bundle), thinner bundles or individual fibers. Collagen fibers aligned preferentially circumferential in the media but showed random orientation in the adventitia. The LU thickness ranges 13-15 μm [123] with an elastic lamellar thickness of 1.0-2.2 μm. The number of LUs of the media layer is established during arterial development and is directly related to the tension in the wall. It was noted that the tension per lamellar unit is constant across mammalian species and throughout the arterial tree [129].

Elastic modulus of elastin and collagen fibers was reported as approximately 0.6 MPa and 1GPa, respectively [130]. Collagen fibers have a wavy nature and low contributions to mechanical behaviors at low pressure load. This is due to the waviness of collagen fibers [131], which was gradually straightened under pressure. Only 6-7% of collagen fibers are engaged at physiological pressure [126]. Microscopy studies on male adult rats revealed that collagen fibers aligned in the longitudinal-circumferential plane of the media layer of aorta. On the other hand, elastin fibers tended to align in the circumferential direction in SML, but often formed a longitudinally network structure in Els [126]. Collagen fibers

were observed more in ELs than in SMLs, and ELs comprise elastin and collagen fibers. Collagen fibers have a diameter of 3 μm and average segment length of 13-17 μm. The diameter of elastin fibers is measured around 0.1 μm which placed in ELs with an interconnecting, fenestrated network.

3.4 **Arterial stiffness**

The stiffness of artery is directly related to the function of each component in the LU. Due to their higher elastic modulus, elastin and collagen fibers were classically considered as the main load bearing elements in LU. At physiological pressure, arterial stiffness was predominantly determined by elastin fibers, while wavy collagen fibers, without being straightened yet, did not bear much load. Then, the abnormally large mechanical load could straighten the collagen fibers, which were able to carry more load than elastin fibers. These sequential participation of elastin and collagen fibers in arterial stiffness led to non-linear stress-strain response of the arterial wall, while it was suggested that VSMCs have no contribution in the mechanical response of the artery [132], as illustrated in Figure 3-2.

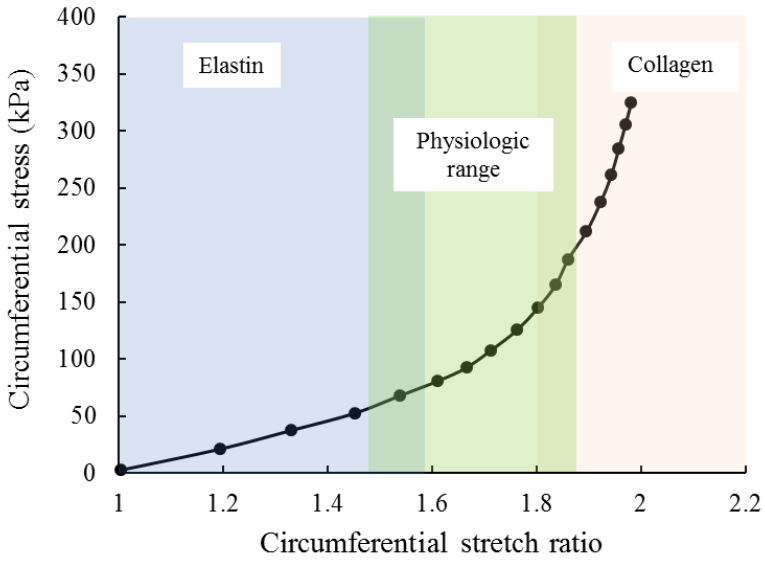

Figure 3-2 Representative circumferential stress–stretch relationship for the mouse ascending aorta.

Increased arterial stiffness is correlated with a larger collagen/elastin ratio in LU. Aging is associated with the defragmentation and discontinuity of elastin fibers. The damaged elastic fibers are generally not replaced, because elastin expression is turned off in adult species. This damage alone will weaken the artery. Then the arterial remodeling lead to more collagen fibers production, and usually increase the arterial stiffness [133, 134]. It has been reported that blood pressure and arterial stiffness are inversely related to elastin's amount in the media layer [129, 135-138]. Many cardiovascular disease, specifically hypertension, are related to high stiffness of artery induced by elastin reduction and collagen fiber production [129]. Advanced glycation end-products (AGEs), which accumulate slowly with normal aging or in diabetes at a faster rate, has been considered as a major index factor for arterial wall stiffening [139, 140]. This was attributed to the increased protein–protein crosslinks on the collagen molecule [141, 142] and implied that collagen/elastin components alone are not the only inclusive parts to

determine the arterial stiffness in certain situations. Using hypertensive rat models, several groups observed minimal changes in collagen content of artery [143-146]. Instead, reduced collagen content were reported in some cases [147, 148]. Hu et al. [149] monitored over 8 weeks of ECM content in a coarctated mini-pig aorta. They observed that relative collagen content was increased at 2 weeks of hypertension, stayed at this high lever for 4 weeks, and then declined to the baseline level at 6 weeks. The relative elastin content decreased at 2 weeks and remained at a similar level thereafter. The incongruous observations in the literature might be due to the variations in experimental protocols, including measurement methods of arterial collagen content, the hypertension degree, and the location of harvested artery [145].

Apart from the variation of collagen/elastin fibers content and ECM in general, VSMCs might have a contribution to arterial wall stiffness. Sehgel et al. [150] suggested to look into the contribution of VSMC to arterial stiffness since variation in elastin density was not enough to induce a major change in aortic stiffness. Animal studies (spontaneously hypertensive monkeys [51, 151] and rats [152]) showed that VSMC in the aortic media layer is stiffer in the arteries with higher stiffness caused by hypertension or aging. These observations indicated that VSMC alone might contribute to arterial stiffness but has not been measured yet.

3.5 **VSMC**

Stiffness measurement of vascular smooth muscle cells are challenging due to its sensitivity to phenotypic switching in response of the environment. It has been reported that cultured VSMC on substrate might change their phenotype to synthetic [153]. VSMCs are aligned circumferentially in the media layer and undergo large deformations in

physiological conditions. When the artery enlarges due to the hemodynamic pressures, VSMCs stretch along their major axis. However, AFM technique is only able to measure the elastic properties of local regions of cells under small deformations and cannot not provide enough information associated with the tensile properties of whole VSMC in physiological strain range (median strain of 25-50 %). Due to the aforementioned reasons, it is vital to obtain tensile properties of the cells freshly isolated from the artery wall. In this regard, different methods for gripping the VSMC and performing tensile test have been suggested. Knotting [154], aspiration [155], adhesion on pipette [156], plate [157] and micropillar array substrate [71] are among the popular cell gripping methods for the tensile testing of VSMCs.

3.6 Mechanical contribution of arterial constituents

3.6.1 Experimental studies

There is a range of techniques to quantify the mechanical behaviors of cells, such as Atomic Force Microscopy (AFM) [145, 150-152]. The contraction response of VSMC can be measured directly by AFM tests, or in an indirect way by comparing the expression of primary SMC-specific contractile markers such as SM α-actin. It is well known that by phenotype changing of VSMCs to synthetic type, the number of stress fibers decreases, and the number of organelles increases which prepare the cell to proliferate and generate ECM proteins. These changes in the cytoskeleton decrease contractility and stiffness of VSMCs (by one-third or one-fourth). Thus, the initiation of cell proliferation can be counted as an indicator of relaxed VSMCs. Hu et al. [149] reported that cell proliferation occurred at 2, 4, and 6 weeks, but not at 8 weeks of hypertension. The highest proliferation

rate was captured at 2 weeks of hypertension. Xu et al. [158] found that proliferation of medial VSMCs was induced rapidly within 3 days after acute coarctation of the rat aorta and continued for 2 weeks. In addition, In addition, fluctuations in VSMCs stiffness was detected over 8 weeks of high tension loading of rat aorta [159]. Tosun and McFetridge [160] used cardiac output to define frequency profile of cyclic stretch of human VSMCs which was against with the previous in vitro models which were stimulated with constant pulse frequencies. It was revealed that the phenotypic outcome may be more dependent on the variation in the stimuli, rather than specific amplitude of change.

These studies indicate that VSMC's stiffness could decrease sharply at the early stages of hypertension because of their dedifferentiation. However, it is reported that medial VSMCs expressing contractile proteins could also proliferate and actively synthesize ECM proteins [149]. On the other hand, the dedifferentiated cells express low levels of contractile markers and high levels of signaling molecules associated with cell growth, migration, fibrosis, and inflammation [161]. Matsumoto et al. [159] investigated the effects of hypertension on morphological, contractile and mechanical properties of rat aortic VSMCs. They found that the density of SFs and the stiffness of each SF may dependent on the intensity and duration of hypertension. The contraction and stiffness of VSMCs increased to its maximum at 8 weeks of hypertension and decreased thereafter. However, these observations were not correlated with the previous studies. The potential explanation could be the level of hypertension, measurement techniques, level of VSMCs tension and VSMCs alignment.

The mechanical properties of elastin fiber network in the media layer were evaluated under uniaxial or biaxial tension [162-166]. Weisbecker et al. [167] compared the

mechanical behavior of elastase and collagenase treated media from human thoracic aorta to untreated control specimens. VSMCs were still visible after elastase treatment and it was noted that their passive response might slightly affect the anisotropy of the tissue. One limitation of this work was neglecting the dependency of the mechanical properties on age or on the location of the artery. Martinez and Han [168] showed that collagenase treatment (collagen content decreased by 15%) caused an enhancement in the axial deformation but not in the circumferential deformation. This was explained by the dominating circumferential alignment of collagen in the vessel wall. While collagenase treatment may equally break the collagen fibers aligned in both the axial and circumferential directions, the ratio of change in the circumferential direction would be much smaller due to the large amount of collagen at the baseline [168]. However, Dorbin et al. [169] observed a considerable reduction in the arterial wall stiffness in the circumferential direction of collagenase treated dog arteries. The difference might be associated with the type of species, the density of collagenase used, or the implemented testing conditions [170]. Moreover, compared to elastase treatment, collagenase treatment seemed had less effect on the physiological pressures as that collagen is not fully engaged in the bearing arterial wall stresses. Reportedly, a decrease VSMC content by 11± 7 % in porcine carotid arteries was associated with enlargement of arterial wall at pressures up to 120 mmHg and mechanical stiffening of the arterial wall at higher pressures [171]. Despite the valuable results, the conducted researches had limitations such as being performed under static loading conditions, and the collagen fibers or VSMCs were partially removed in the treated specimens.

Although there have been many experiments to quantify the contribution of medial fibrous matrix in mechanical properties of the artery, the load sharing capacity of VSMCs has been underestimated. Previous studies about determining the stiffness and contraction of VSMCs in hypertension provided valuable information but sometimes are inconsistent which makes it difficult to evaluate the mechanical contribution of VSMCs in normotension and hypertension arteries. In addition, the load sharing capacity of VSMCs in LU is still not clear. Heterogeneity of LU and different mechanical properties of each component are the problematic issues to determine the portion of load taken by each constituent when the artery is exposed to hemodynamic pressures.

3.6.2 Computational methods

Numerical simulations have been implemented for many years to study the mechanical behavior of arteries. In the previous developed models, the arterial wall has been modeled as a single layer [172], two or three layers [173, 174]. The applied constitutive relations to the arterial wall have been formulated by hyperelastic material with orthotropic, transverse isotropic, and isotropic behavior [175-179]. The main concern about these models was to predict the macroscopic mechanical properties of the artery and evaluate its deformation [180-183]. Considering the highly heterogeneous microstructure of the arterial layers has been challenging in these studies.

Furthermore, micromechanical modeling approach has been employed to include clearly distinguishable constituents inherited different material properties. The goal was to predict the anisotropic response of the heterogeneous material on the basis of the geometries and properties of the individual constituents, a task known as homogenization [184]. Application of micromechanical modeling in arterial mechanics is vast. Capturing

the responses of hyperelastic tissues with multiple families of collagen fibers [185], elucidating the interaction between collagen and non-fibrillar matrix [186], strain hardening of collagen-I gel and realignment of the network [187] can be counted as the micromechanical modeling applications associated with the behavior of fiber matrix. Thunes et al. [123] developed a micromechanical model to detect the stress field of the fiber matrix after collagen recruitment. The VSMCs were simplified and replaced by a homogenous medium as the non-fibrous part.

In order to study the VSMC contraction effects in the media tunica and stress distribution through the thickness of artery, Lukes and Rohan [188] proposed a 3D micromechanical model, which consisted of a hyperelastic matrix (ECM), an incompressible inclusion (VSMC), and contractile bars (SFs). The micro-scale model was then coupled with a 2D macro-scale model of the arterial wall consisted of two layers of tunica media and tunica adventitia.

Nakamachi et al. [108] constructed a multi-scale FE model for stress and strain evaluation of VSMC of the human artery. Their micro-scale model was based on a Representative Volume Element (RVE) model and consisted of a VSMC embedded in a homogenous matrix, Figure 3-3. Despite of the novelty of the developed model, the simplified ECM structure and neglecting the distribution of collagen/elastin fibers could be influential on the obtained results. Moreover, there were lack of discussion about mechanical contribution of the constituents in the arterial wall.

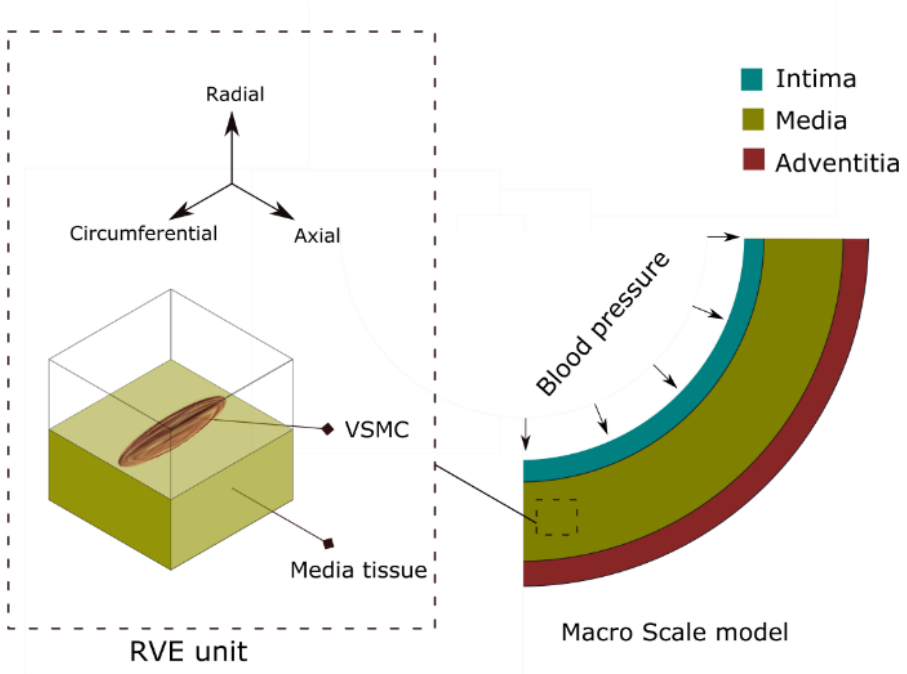

Figure 3-3 macro scale model of the arterial wall with three layers (right); arterial VSMC and RVE model (left)

It has been found that the microstructure of ECM can vary by some diseases. Collagen disposition and cross-link disruption has been observed in the arteries with Marfan syndrome [189]. Moreover, Marfan aortic samples are histologically characterized by the fragmentation of elastic laminae (almost 50 per cent lower [190-192]), which leads to the formation of aneurysms. Therefore, considering the heterogeneous structure of ECM will allow to detect the ongoing mechanisms behind the arterial disease which change the properties of ECM and VSMC state.

3.7 **Summary**

This review summarized the mechanical contribution of VSMCs to the arterial stiffness with focus on the load sharing of collagen/elastin fibers and contracted/relaxed VSMCs in the media layer of artery. In view of VSMCs cytoskeleton, it was noted that stress fibers have the major contribution in VSMCs contraction, however, microtubules and

intermediate filaments can indirectly affect contractility of the cells. In addition, the cytoskeleton responses are strongly related to the interaction of integrin receptors and extracellular matrix.

VSMCs alter their proliferation and contractility or change their phenotype with respect to the mechanical environment, such as 2D or 3D ECM, and level of cyclic strains. Specifically, the cultured VSMCs change their phenotype compared with in vivo conditions. The responses of VSMCs subjected to cyclic loading is dependent on the time period of the applied load.

The mechanics of VSMCs could be better delineated using numerical simulation. The interaction between collagen and non-fibrillar matrix, alignment and recruitment of collagen fibers and induced stresses in VSMCs during extension have been elucidated. However, the load sharing capacity of VSMCs in Lamellar unit as well as the influence of phenotype changing on the VSMCs contribution in arterial stiffness remained to be determined.

Chapter 4: Multi-scale modeling of lamellar unit in tunica media of artery

Introduction

Cardiovascular disease accounts for 17.3 million deaths globally and one of every four deaths in the United States each year [193]. Hypertension and aging are both recognized to increase arterial stiffness which causes major common chronic diseases, such as heart failure, myocardial infarction, stroke, vascular dementia, and chronic kidney disease [194]. Vascular stiffening is considered one of the pathophysiological mechanisms contributing to the development of hypertension [195].

The stiffness of the arterial wall is strongly dependent on the structure and integrity of lamellar units (LU) (i.e., vascular smooth muscle cells [VSMCs] encompassed by elastic lamellae and interposed with a collagen fiber network) [125]. Collagen deposition and elastin breakdown in the extra cellular matrix (ECM) has been widely considered as the predominant mechanism of arterial stiffening [196]. However, it was also reported that these changes of the ECM were not consistently observed in hypertensive arteries [197]. In some cases, clinical hypertension measurements detected a reduction in vascular collagen content [148].

Structural variations in the artery may be attributed to the VSMC [198], while controversy exists regarding the contribution of VSMCs [199]. Bank and Kaiser [200] claimed that VSMCs' relaxation can potentially occur in concert with an increase, a decrease, or no change in vascular wall stiffness. It has been hypothesized that VSMCs' relaxation decreases arterial stiffness by reducing tension generated by the VSMC itself.

However, VSMCs' relaxation has been counted to increase the arterial stiffness by engaging stiff collagen fibers. Moreover, it was observed that the total arterial stiffness was directly related to the VSMC's stiffness [201]. In contrast, it was demonstrated that adaptation of the hypertensive artery and thickening of the vascular wall were caused by changing the phenotype of VSMCs from contractile to synthetic and producing more collagen fibers. In the synthetic phenotype, the stiffness of VSMCs is lower than that for the contractile phenotype, while the total arterial stiffness is higher than for normal conditions [195]. This research reported an inverse relation of the VSMC's stiffness and the arterial wall stiffness. Though, the arterial stiffening has been well documented in humans and animal models over a century, the contribution of the VSMC among the LU components in arterial stiffness has not been quantified yet.

Due to the complexity of the LU micro-structure, nonlinear properties of the fibrous network, and interaction between the VSMC and ECM, the in vitro studies are unable to meticulously reassemble the vascular wall to detect the contribution of VSMCs in arterial stiffness. When cultured on a substrate, the cells change their phenotype from contractile to synthetic [153], and their cytoplasm contains few filament bundles but a large amount of organelles, and hardly contract in response to contractile agonists. Therefore, the captured responses based on 2D experiments can be different with the in vivo behavior of VSMCs embedded in the ECM.

Several structurally motivated constitutive models for the arterial wall have been recently developed [202-206]. Nakamachi et al. created a multi-scale model in which the LU was modeled by a representative volume element (RVE) consisting of a VSMC embedded in a homogenous ECM [108].The developed model illustrated the stresses and

strains of the VSMC under tension; however, the heterogeneity of the fibrous part of the LU, the waviness of collagen fibers, and the constituent's volume fractions, were neglected.

In this work, a novel multi-scale model has been developed to characterize the load sharing capacity of the VSMC in the LU and the corresponding aortic wall deformation. An RVE model was constructed by considering the architecture of collagen fibers per their volume fraction and distribution, and the nonlinear response in tension. The obtained mechanical response of the RVE was imported to a macro-scale model of the aortic wall to capture its deformation subject to the physiological blood pressure. The developed model allowed us to incorporate the micro-structural variation of the LU induced by aging and the resulting changes in aortic mechanical behavior.

4.1 Materials and Methods

4.1.1 Micro-mechanical modeling

We constructed a 3D representative volume element (RVE) to simulate the biomechanical response of a single lamellar unit. An average lamella thickness of 1.5 μm and an interlamellar (IL) spacing of 10 μm were chosen [207]. We exploited the LU symmetry in the circumferential and radial directions and considered a VSMC embedded in the ECM. The volume fraction of elastin fibers within the lamella has been measured as 85 % [208]. The orientation histogram revealed that planar dispersion of the elastin fibers in the longitudinal-circumferential plane is approximately uniform figure 4-1.

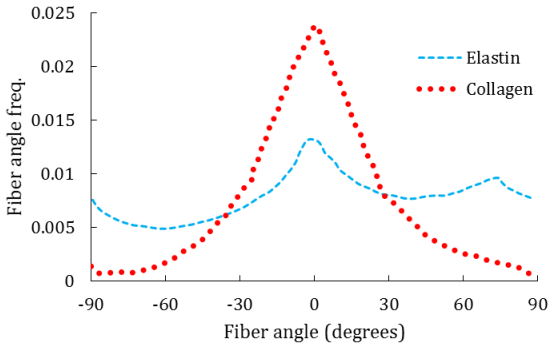

Figure 4-1 Distribution of collagen and elastin in LU; Angle of 0 means circumferential direction and 90^{o} is along the length of artery [208]

Therefore, in our model, lamella was treated as a homogenous solid section attached to the interlamellar space (Figure 4-2). The volume fractions and dimensions are listed in table 4-1.

Table 4-1 the volume fraction and geometry of RVE constituents

Component	Volume fraction (%) [201]	Geometry (Units are in μm)
VSMC	47	Major radius = 20 [207] Minor radius = 4.5
Elastin laminate	13	Thickness = 1.5 [123]
Collagen fiber	12	Diameter = 3 [209] Length = 9
Ground substance	28	Length × Width × Height = 10 × 10 × 40

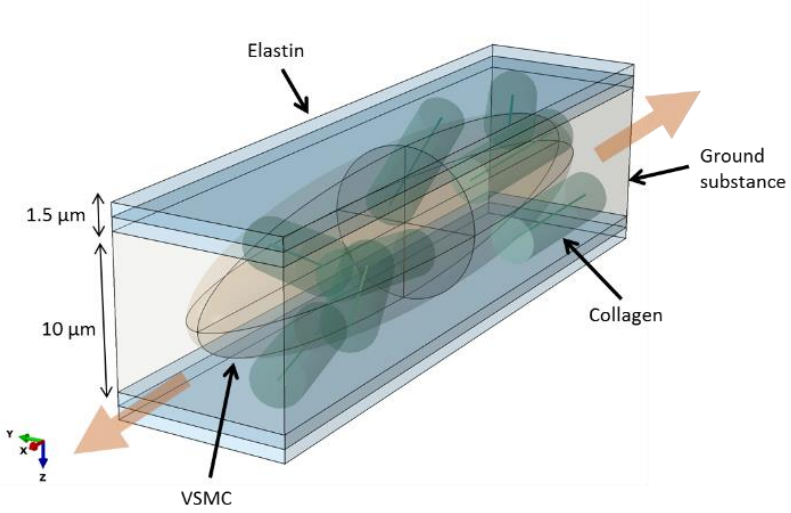

Figure 4-2 the developed RVE model of lamellar unit (LU)

For collagen fibers, a bilinear constitutive response was considered to capture the effect of the fiber waviness [128]:

$$\sigma = \begin{cases} 0 & ,\lambda < \lambda_{Collagen} \\ E_{Collagen}(\lambda - \lambda_{Collagen}) & ,\lambda \geq \lambda_{Collagen} \end{cases} \quad (1)$$

where λ is the current stretch ratio of fibers, $\lambda_{Collagen}$ is the recruitment stretch criteria, and $E_{Collagen}$ is the elastic modulus of the fiber. Collagen fibers with $\lambda < \lambda_{Collagen}$ do not sustain any loading. The bundle of collagen fibers had a diameter of 3 µm [209]. Table 4-2 summarizes the mechanical properties used in the RVE model.

Table 4-2 Mechanical properties of RVE

Role	Parameter	Fitted value
VSMC	E_{VSMC}	0.0881 MPa (Contracted) [127] 0.0148 MPa (Relaxed) [127]
Elastin laminate	$E_{Elastin}$	0.6 MPa [210]
	$\lambda_{Elastin}$	1
Collagen fiber	$E_{Collagen}$	80 MPa [211]
	$\lambda_{Collagen}$	1.4 [212]
Ground substance	E_{GS}	0.0001 MPa

The RVE was subjected to an applied stretch of λ = 1.5 in the circumferential direction. The stress-strain response of LU was imported into the model described below to predict the macro-mechanical behavior of the media layer of the aorta.

4.1.2 Macro-mechanical modeling

A 2D model of the aortic cross section was generated considering its three-layer structure (i.e., intima, media, and adventitia). Due to the axial symmetry of the aorta, only ¼ of the cross section was modeled as shown in Figure 4-3.

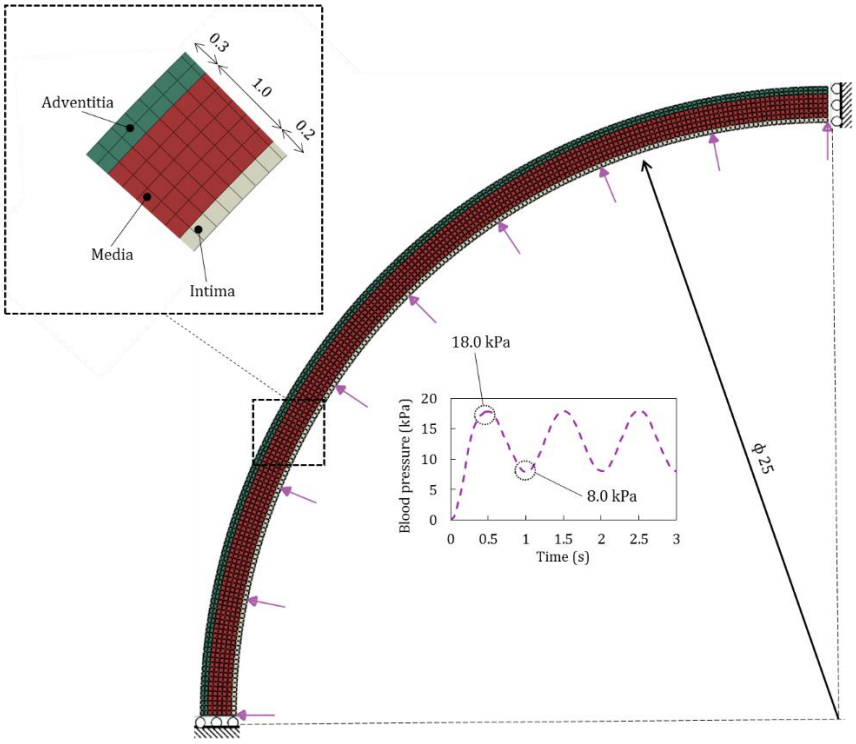

Figure 4-3 Macro finite element model of the human blood vessel, dimensions (unit: mm) and loading condition.

The inner diameter of the aorta was 25 mm with a total thickness of 1.5 mm. After mesh sensitivity analyses, the model was discretized with 1608 CPS4R elements. The cyclic internal pressure profile was applied to mimic the physiological blood load.

The aforementioned three-layer aorta model is an improved version from the two-layer model by Nakamachi et al. [108]. The accuracy of the calculated displacement, strain, and stress depends on the accuracy of the modelled layer-specific stress-free geometry, constitutive equations, and boundary condition.

The hyperelastic behaviors of the intima and adventitia layers were extracted from the published experimental datasets [213], which were fitted using the reduced polynomial constitutive equation below:

$$U = \sum_{i,j=1}^{3} C_{ij}(I_1 - 3)^i (I_2 - 3)^j \quad (2)$$

where, I_1 and I_2 are the first and second invariants of the Cauchy-Green tensor. The obtained material coefficients by using curve fitting are listed in Table 4-3.

Table 4-3 Material coefficients of both adventitia and intima layers

Layer	Coefficient
Adventitia	C_{10} = -1.1373 C_{01} = 1.206 C_{20} = 6.5364 C_{11} = -17.819 C_{02} = 12.870
Intima	C_{10} = -0.7699 C_{01} = 0.8235 C_{20} = 2.623 C_{11} = -7.5097 C_{02} = 5.8136

While for the media layer, we extracted the extension response of the RVE model and compared it with the uniaxial test data [45] of the media layer to verify the micro-mechanical model and then to assign the obtained behavior to the aorta model.

Figure 4-4 reveals the comparison between the obtained results and the experimental data. It can be seen that the trend of variation was identical and could break in the soft portion associated with the physiological pressure level and the stiff portion in response to the higher blood pressure levels where collagen fibers engaged in load bearing.

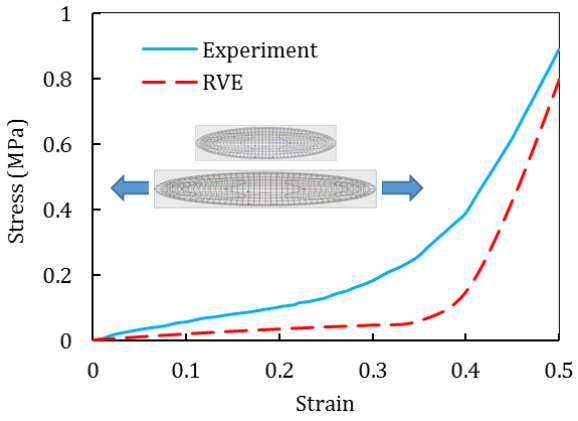

Figure 4-4 Stress-strain response of the media layer

Alternatively, the difference between the finite element model and the experimental data can be addressed by various causes, such as conditions of the in vitro-treated specimen and the selected arterial segment. Moreover, the RVE model is an idealized representation of the LU structure of the media layer, although it has been reported that separating the media layer from adventitia/intima layers during in vitro tests has some complexities that might affect the obtained response [214].

By implementing the multi-scale modeling, we could characterize the VSMC's contribution in load sharing of the arterial wall in different stretch levels and various contraction states. Moreover, the effect of aging through deposition of collagen fibers and fragmentation of elastin fibers could be studied.

4.2 **Results and Discussion**

Our micro-scale model, as a representation of the lamellar unit of the human aortic media, directly included the structural features of the ECM. The developed model could recapitulate the circumferential constitutive response of the media layer successfully. The load shared by VSMCs was calculated by integration of all nodal forces along the loading direction. Figure 4-5 illustrates the load sharing contribution of the ECM and VSMC in the LU exposed uniaxial tension. The VSMCs at lower stretch levels had a higher contribution in load sharing. However, at larger stretch levels collagen fibers came into play and took more loads which muted the contribution of the VSMCs.

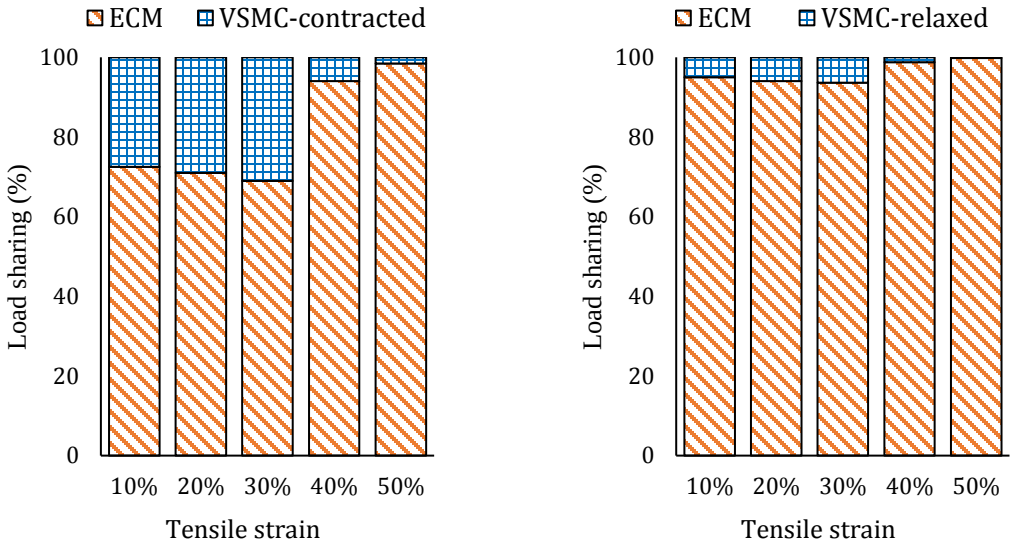

Figure 4-5 the contribution of VSMC and ECM in load sharing in a healthy carotid aorta LU

In the case of the contracted VSMCs, load sharing of 30 % was detected at normal tension levels, while this value decreased to 1.5 % in hypertensive conditions (tensile strain

40 % and higher). In contrast, the relaxed VSMCs did not play a significant role in LU stiffness and could not take more than 6 % of the tensile load. These values could be altered with respect to the LU micro-structure and the volume fraction of its constituents. It has been claimed that VSMCs' static stiffness varies according to their position in the arterial tree. Based on the confocal images regarding the VSMC shape and actin stress-fiber orientation, VSMCs from arteries with fewer elastic fibers (femoral and renal) are considered to be stiffer compared with the thoracic aorta VSMCs [201].

Hereby, we studied the effect of fiber fragmentation due to aging effects. Therefore, a range of fiber loss from 10 % to 50 % was considered and the equivalent stiffness of the LU was computed for each case. Figure 4-6 depicts the loss of stiffness versus the fragmentation of elastin or collagen fibers.

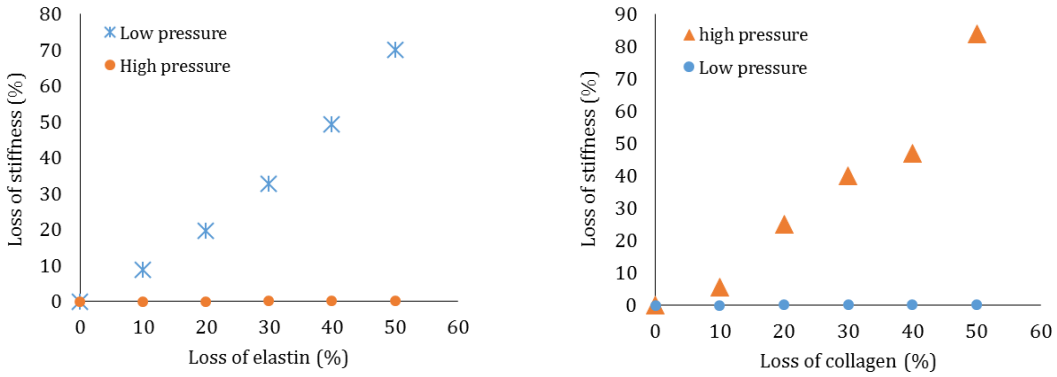

Figure 4-6 the influence of Collagen disruption and elastin fragmentation on the LU stiffness

It is clear that at low pressure levels (tensile strain is less than 40 %) the elastin loss decreased the stiffness considerably. In more detail, 50 % fragmentation of the elastin layer caused 75 % loss of stiffness. However, collagen fiber loss showed its dominant influence in high pressure levels (tensile strain is more than 40 %) where collagen fibers were

straightened. By comparing these curves, the contribution of fibers in total stiffness of the LU can be distinguished. Moreover, it has been reported that during the process of arterial aging, and after the loss of the fibrous part of the LU, VSMCs produce more collagen fibers as a remedy to the lack of elastin fibers. By considering the waviness of these fibers and our obtained results, it can be concluded that even deposition of collagen fibers cannot contribute to arterial stiffness at normal tension conditions. Therefore, the paradigm of age-related arterial stiffness has recently shifted from elastin/collagen content to cell-ECM interactions and VSMC tone as the principal determinants of arterial wall stiffness [215]. On the other side, it has been claimed that the environmental changes caused by aging derive a switch from a contractile phenotype to a synthetic phenotype of VSMCs. The latter phenotype is characterized by reduced expression of contractile proteins meaning lower stiffness. Therefore, in this condition, the lack of arterial stiffness is addressed by the thickening of the arterial wall and geometric remodeling.

Differentiated phenotypes (contractile) of VSMCs can be evaluated by morphology studies from which VSMCs are spindle shaped. In this study, we derived the variation of the VSMCs' section-area for different levels of tension, Figure 4-7.

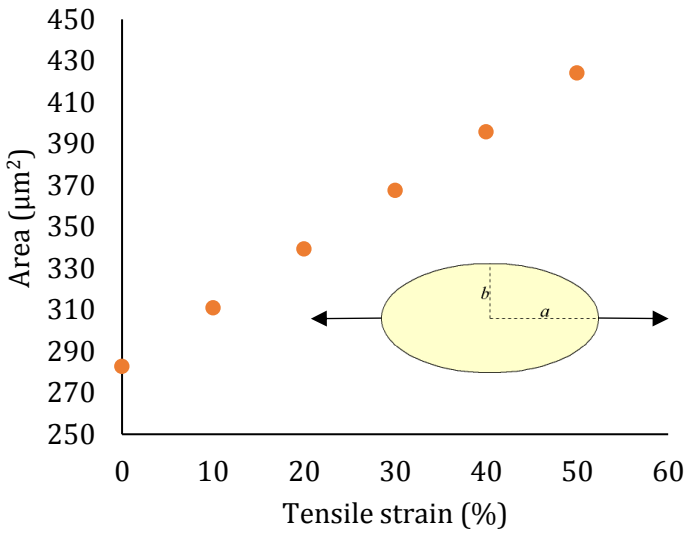

Figure 4-7 the calculated area of VSMC with respect to the stretch level

Dinardo et al. [201] measured the major axis/minor axis ratio of VSMCs located in different arterial beds. This parameter was counted as an indicator of the cell elongation and then interpreted as the contraction level of VSMCs. They observed that VSMCs from femoral and coronary arteries were more elongated than that of other vessels and concluded that the VSMCs from former arteries have higher contraction (static rigidity). On the other hand, they observed that femoral and coronary arteries have the lowest content of elastin and ECM/VSMC ratio. According to our results, the higher volume fraction of VSMC means it had a larger contribution in load sharing and more elongation. These physical variations occurred even if the contractility of VSMCs remained at a fixed value. As we observed, the ratio of the major axis/minor axis and therefore the VSMCs' area was directly related to the tensile strain caused by hemodynamic loads. Moreover, it has been observed that the contraction of 2D cultured VSMCs and the ratio of the major axis/minor axis is inversely related. Therefore, the elongation of VSMCs cannot be an appropriate parameter

to detect the contraction level. However, comparing this parameter can provide useful information about the phenotype of the cell and the load sharing of VSMCs.

At the next step, we modeled aging effects on the aortic expansion in different tension levels. Figure 4-8 shows the recorded expansion of the aorta for various collagen/elastin ratios and each VSMC's status. For higher values of the collagen/elastin ratio the expansion of the aorta decreased drastically. This variation happens by collagen deposition caused by aging. The largest decrease in aortic expansion for high tension levels was 20 %, while in normal tension levels the relation of collagen deposition and arterial expansion was insignificant. Hereby, we did not change the volume fraction of elastin. As a result, at a normal tension level the expansion fluctuation is minimal.

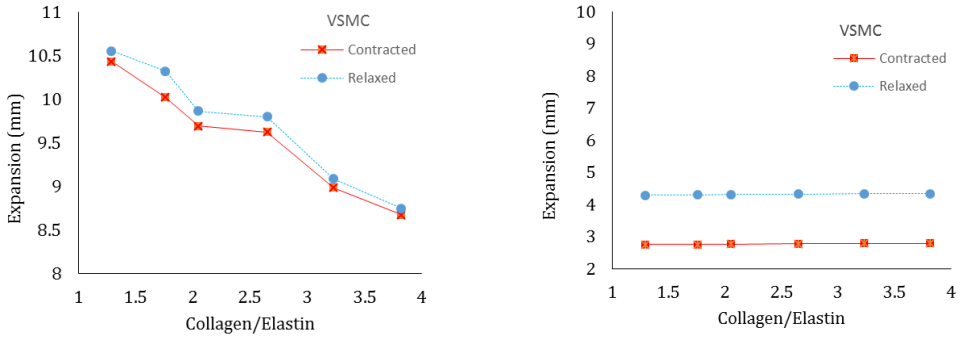

Figure 4-8 arterial expansion with respect to the different VSMC status and collagen/elastin ratios; Normal tension (right), hypertension (left).

Moreover, at a normal tension level the expansion of the aorta was distinguishable for each VSMC status. However, for high pressure levels, the response of contracted and relaxed VSMCs converged. This result showed that in hypertension and where collagen deposition occurs, variation of VSMCs' stiffness cannot change the aortic stiffness and expansion. On the other hand, it could be seen that if material remodeling happens, but the

aorta still works under a normal pressure level, VSMCs' contraction/relaxation can considerably affect the arterial dilation. It has been reported that the mechanical phenotype correlates with the composition of ECM and can be modulated by the stretching imposed on VSMCs by blood flow circumferential stress [201]. In this study, we saw when aging occurred and more collagen fibers were produced in the ECM, then the mechanical variation of VSMCs could be meaningful only in a normal tension level.

4.3 **Conclusion**

In this paper, we have developed an RVE model based on the lamellar unit of the media layer in the aortic wall. The developed model helped us to distinguish the load sharing capacity of fibrous and non-fibrous parts of the LU. In addition, micro-structural variation of the LU was analyzed, and the corresponding macro-structural behavior was studied through multi-scale modeling of the aortic wall. Our results showed that the VSMC can take up to 30 % of the applied load when contracted. It is known that the relaxed VSMC is around 10 times softer than the contracted one, which affects its contribution in load sharing of the LU. On the other side, the contribution of collagen fibers at low stretch levels was negligible but became predominant when straightened in high stretches. The obtained uniaxial response of the LU was validated against the previous experimental data. The macro-scale model of the aorta allowed us to evaluate the arterial expansion with respect to the micro-structural variation of the lamellar unit. Finally, aging effects by collagen deposition was modeled and aortic dilation was estimated. It was revealed that stiffening of the VSMC when the aorta is exposed to high pressure does not affect the aortic stiffness but is mainly controlled by collagen fibers. Our findings can shed some light about the contribution of VSMCs in arterial stiffness which has been under debate in recent years.

Chapter 5: Characterization of mechanical properties of 3D-printed PLLA/Steel particle composite

5.1 Introduction:

The 3D printing is gaining increased attention by fabricating, usually layer by layer, complex structures with the minimal waste of raw materials. The printed pure polymer products are limited by its lower strength and functionality, and then the polymer composites reinforced by fibers and particles have been considered [216]. For example, metallic particles as the reinforcement of 3D printed polymer composites were investigated in terms of their mechanical, thermal, and electric properties. Nikzad et al. [217] developed Iron/ABS and Copper/ABS 3D printed particle composites to achieve higher stiffness. Boparai et al. [218] examined systematically tribological characteristics of a composite material with Al and Al_2O_3 particles embedded in Nylon6 matrix. As a result, higher wear resistance, thermal stability, and stiffness was attained. Impact resistance and tensile strength as well as electromagnetic characterization of a 3D Printable Tungsten–Polycarbonate polymer matrix composite for space-based applications has been studied experimentally[219]. However, the nanoscale mechanical characterization of 3D printed particle composites was lacking.

Existing researches focused on the effect of particle size [220], distribution [221], and shape [222] on the mechanical properties of composites without considering the contribution of interphase layer. Nonetheless, the interphase properties and interface strength play an important role in the mechanical properties provided by the particle composites [223]. A well-designed interphase can significantly enhance the strength and toughness of particle composites. Therefore, characterization of interphase mechanical

properties, which varies with respect to the distance from the particles, should be studied meticulously. The problems in finding an accurate description of interphase properties are mainly due to the inhomogeneity of the material, i.e. the high stiffness ratio between particles and matrix [224]. Analytical models were developed to encompass the influence of interphase layer. The earliest models [225] assumed that the two components are both homogeneous, and are perfectly bonded across a sharp and distinct interface. Hashin and Rosen [226] developed a model for particle composites in which a thin layer existed outside of each particle. The elastic moduli were uniform within this layer, but different from those in the matrix or particles. Afterwards, others have attempted to account for smooth variation of the moduli with radius. Lutz and Zimmerman [227] modeled the moduli outside of the inclusion with a constant term plus a power-law term, thereby allowing a smooth transition between the interphase layer and the matrix. Despite the capability of analytical models to calculate bulk properties of composites, determining the local microstructure parameters such as the effective interphase thickness and fluctuations of elastic modulus is not feasible by this approach. Hereby, quasi-static nano-indentation has become the standard technique used for nano-mechanical characterization of materials.

Nano-indentation measurement has broad application across the physical sciences [228], and there are several researches on the implementation of this method for property extraction. In [229] nano-indentation tests were employed in order to investigate the material properties of the interphase region in phenolic/glass and polyester/glass systems. Moreover, local mechanical property variation in the interphase of E-glass fibre reinforced epoxy resin and E-glass fibre reinforced modified polypropylene (PPm) matrix composites was conducted by using this method [230]. Urena et al. [231] measured the mechanical

properties of the generated interphase by reaction between aluminum matrix and SiO_2 coating. Hardness and Young modulus of the interphase between matrix and reinforcement of Al 2014 matrix composites reinforced with $(Ni_3Al)_p$ was determined by Torralba et al. [232]. However, the studies on polylactide (PLLA) and especially particle reinforced PLLA composites are scarce [233]. Moreover, there is no research associated with nano-mechanical characterization and property extraction of PLLA polymer composite reinforced with steel particles.

The objective of this study was to characterize the mechanical properties of 3D printed PLLA /Steel particle composites by using nano-indentation tests. And to accurately extract the interphase properties, and finally extract the bulk mechanical properties of PLLA /steel composite through a homogenization analysis. Homogenization analysis is a method for obtaining mechanical properties at the macro-scale from the obtained responses of nano- or micro-scale structures. Nano or micro-scale stress and strain distribution for each component material in composite materials can be visualized by localization analysis [234]. At the first step, fused filament fabrication (FFF) were employed to manufacture PLLA /Steel composites. Moreover, nano-indentation tests were performed to determine the Young's modulus of the matrix and particles and variation of Young's modulus at the interphase layer. Secondly, a micro-scale finite element model was developed by using a generated subroutine code to encompass the mechanical properties of interphase layer and then homogenization analysis was performed to obtain the bulk mechanical properties of PLLA /steel composite.

5.2 Experimental procedure

5.2.1 3D printing method

Fused filament fabrication (FFF), also known as fused deposition modeling (FDM), is one of the most commonly used additive manufacturing (AM) technologies. A continuous filament of amorphous thermoplastic material is extruded through a heated nozzle and deposited in a single track. Typically, a raster pattern is used to form a single layer by moving the printing head (nozzle) horizontally (X-Y). Deposited material promptly solidifies and adheres with adjacent tracks of material to form the required geometry. The process is repeated as the platform moves vertically (Z) to enable deposition of another layer. Commonly used materials for FFF include acrylonitrile butadiene styrene (ABS) and polylactic acid (PLLA). One of the main advantages of AM compared to other traditional manufacturing process is access to each layer for modifying material properties.

PLLA 420SS composite samples were printed by fused filament fabrication (FFF) on a Hyrel Hydra 645 (Figure 5-1a). A schematic of FFF indicating interlayer particle deposition is shown in Figure 5-1b. Physical and mechanical properties of the PLLA and 420SS are provided in Table 5-1. The PLLA filament from 3D4MAKERS (Netherlands) had a natural color and a diameter of 1.75 mm. Micro-melt 420LC stainless steel powder from Carpenter Powder Products (USA) had a diameter between 45 µm and 105 µm. The 420SS powder was randomly deposited between printed layers using two layer deposition frequencies: every fifth (L5) and every eighth layer (L8)., A total of 25 layers were printed for each sample at a layer thickness of 0.2 mm, 90% infill density, and a rectilinear infill pattern with a 45º infill angle. The L5 and L8 samples had powder deposited on five layers

and three layers, respectively. The amount of powder deposited on each layer was approximately 0.5 g (low concentration) or 1.0 g (high concentration). At 220 ºC, the nozzle temperature was above the glass transition temperature of PLLA and allowed for smooth material flow for deposition. The build plate was heated to 55 ºC to promote adhesion with the part. The travel speed of the nozzle was 50 mm/s. The dimensions of each sample were 50 mm by 12.7 mm by 5 mm (Figure 5-2). A brim of 4 mm was also printed to help secure the edges of the part to prevent warping and improve layer adhesion to the build platform. The produced ample is depicted in Figure 5-3.

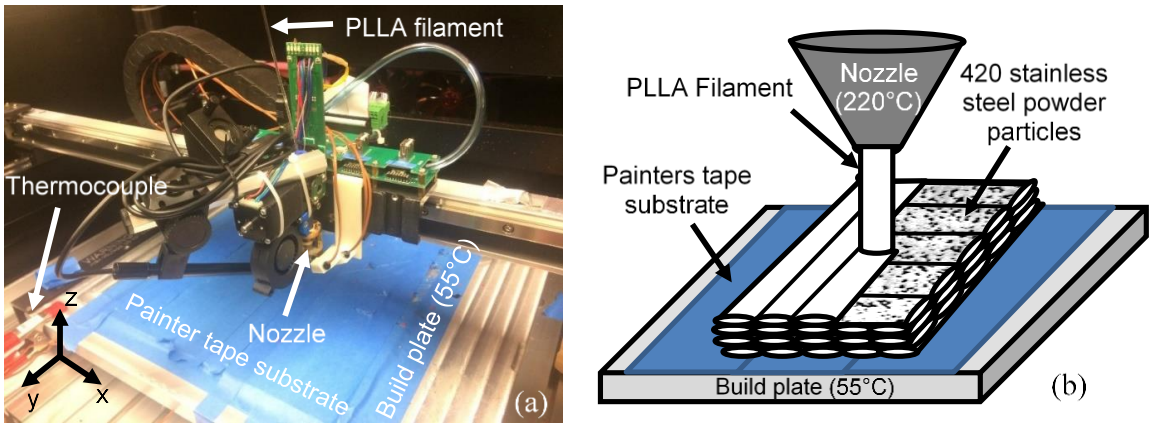

Figure 5-1 Equipment and schematic of 3D printing PLLA Steel composite, (a) FFF Hyrel Hydra 645 3D printer, (b) FFF process schematic

Table 5-1 Physical and Mechanical Properties of PLLA and 420 Stainless Steel

	Density	Tensile Strength	Flexural Modulus
	(g /cm^3)	(MPa)	(GPa)
PLLA	1.26	71	3.31
420 Stainless Steel	7.72	1793	199.95

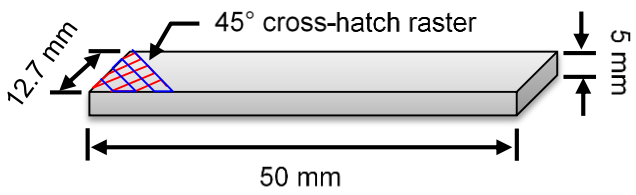

Figure 5-2 Sample geometry of fused filament fabricated PLLA-SS420 composites

Figure 5-3 the 3D printed ample with 3 % of particle volume fraction

5.2.2 Nano-indentation tests

5.2.3 Sample preparation

Using Buehler ISOMet 1000 Precision Saw, the sample is cut along the cross-section. By using Keyence laser scanning microscope VK-X200K, the SS420 particle is the bright part and PLLA matrix is the dark part in Figure 5-4. In order to study the effect of surface roughness another sets of samples were polished by Buehler MiniMet 1000 Grinder-polisher.

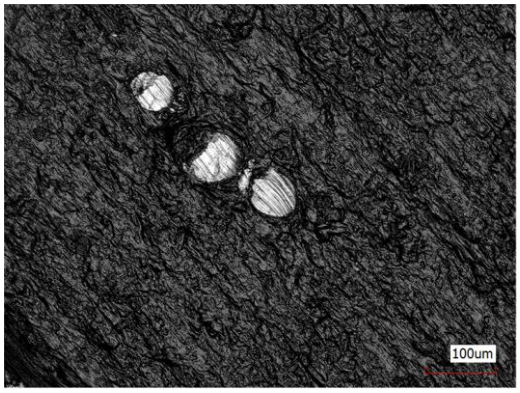

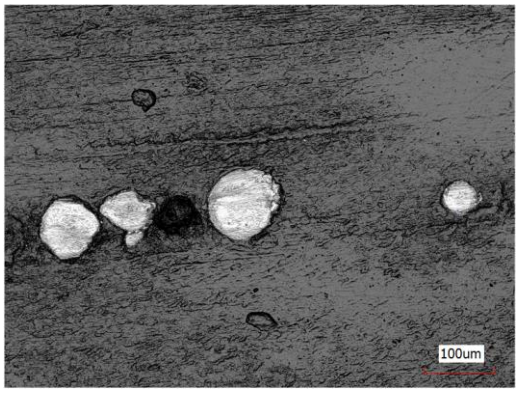

Figure 5-4 PLLA-SS420 composite under 20X microscope lens: before polish (left) & after polish (right)

5.2.4 Nano Indentation Probe

The Hysitron TI 950 TriboIndenter is used to test the interphase mechanical property. The experiment setup is shown in Figure 5-5.

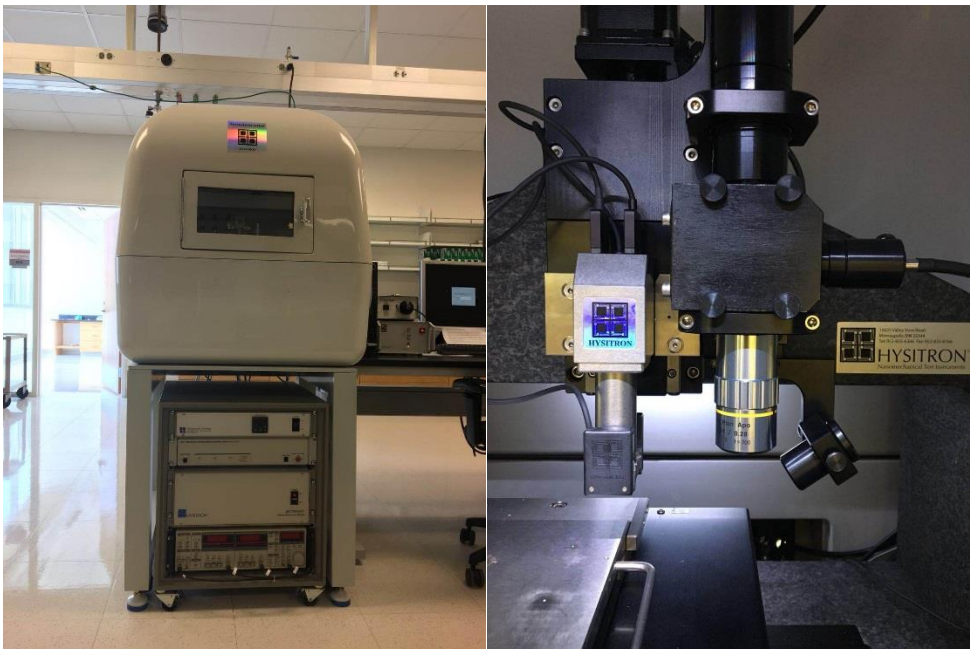

Figure 5-5 Hysitron TI 950 Triboindenter

In the experiment, cube corner probe is used. The geometric parameters of probe are listed in Table 5-2 Probe's Parameters. The surface morphology of probes indentation is shown in Figure 5-6.

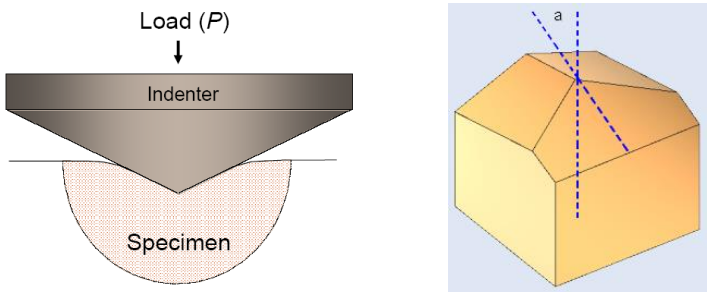

Figure 5-6 Nano Indentation schematic (left), Three-side pyramidal probe schematic (right)

Table 5-2 Probe's Parameters

Probe	Cube Corner
Included angle	90°
Half angle	35.26°
Radius of Curvature	~40-100 nm
Material	Diamond

In the following indentation test, 200 nm displacement control is used to test local mechanical property. And the distance between testing point is set to be 1 μm, make sure the current testing area don't overlap with the previous indentation. Thus, the resolution of the interphase thickness is 1 μm.

5.3 **Finite element modeling**

A micromechanical representative volume element (RVE) model was created by suing Digimat/FE package and then imported to ABAQUS. The steel particles were randomly distributed in the PLLA polymer matrix with the same volume fraction of experimental samples. Steel particle size and RVE size is depicted in Figure 5-7. Perfect bonding was considered for the interface of particles and interphases by using tie constraint. Moreover, to study the effect of bonding strength, imperfect bonding was considered by introducing contact constraint between interphase and matrix.

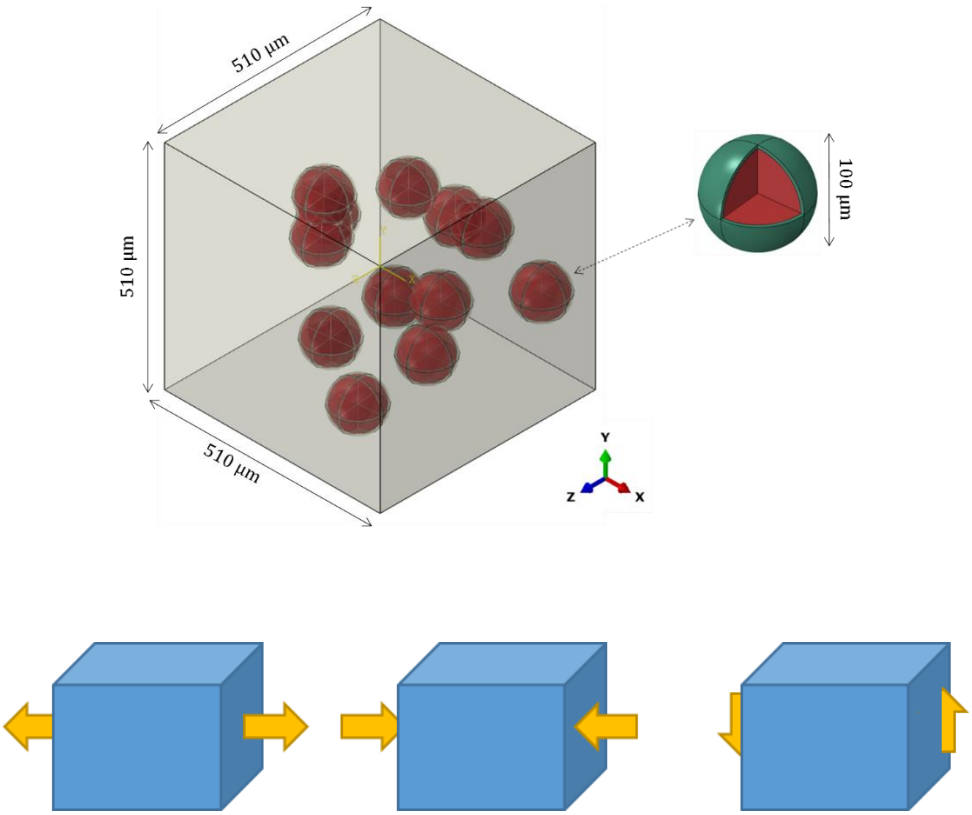

Figure 5-7 the generated RVE model and loading scenarios

The volume fraction of particles was set to 3 %, 5% and 10% to evaluate the load sharing effect of steel particles inside the PLLA polymeric matrix. The number of elements varies approximately from 89000 to 251000 depending on the volume fraction of particles. Mesh sensitivity analysis suggests that the meshes are fine enough to produce accurate results compared to a mesh with twice as many elements, with a difference within 0.2% in terms of stress level. Periodic boundary condition, which developed by a user-specified Python script, was enforced in all directions to extend the RVE periodically, i.e., considering the interaction between the RVE with its mirrored images. The periodic boundary condition was expressed in terms of the displacement vector u, which related the displacements between the opposite edges according to

$$u(x, y, 0) - u_z = u(x, y, L)$$

$$u(x, 0, z) - u_y = u(x, L, z)$$

$$u(0, y, z) - u_x = u(L, y, z)$$

where L was the length of the RVE; x, y, and z stood for the coordinate axes of the three edges of the RVE; andu_x, u_y, and u_z depended on the particular loading applied to the RVE. Three loading scenarios are considered in this study which are shown in Figure 5-7.

5.4 Results and discussion

5.4.1 Experimental results

Nano indentation test has been used to extract elastic modulus, hardness, and yield stress from indentation force-depth curve. Most of the previous studies on nano indentation have been concentrated on materials with a smooth surface [235, 236]. Our observations of the surface of samples showed that cutting process has created roughness and it has been reported that the characteristic size of roughness may have a significant influence on the test [237]. Therefore, it is crucial to investigate the effects of surface roughness on Nano indentation. Based on our measurements the height of defects was in rage of 300-500 nm which is decreased to 60-100 nm after polishing. We conducted nano indentations starting adjacent the edge of particle toward the center of particle. For each type we obtained load-displacement responses of 6 different particles.

It is worthy to mention that the variation of elastic modulus for unpolished sample was sporadic for all studied particles. It can be seen the captured values or unpolished sample has a significant fluctuation which is against our understanding of interphase mechanical properties. On the other hand, the magnitude of elastic modulus is gradually increasing from the edge of the particle to the center. Therefore, the polished samples were used for further studies.

5.4.2 Converge study of Indent Depth

After the surface is polished, the roughness is less than 100 nm. However, it is still necessary to study the convergence of measured mechanical property (Reduced Modulus, Hardness, etc.). The modulus of sample is generated by curve fitting during unloading. The roughness on the surface could influence the Nano indentation load-displacement curve. After the indentation depth is larger than the surface roughness, the roughness on the surface couldn't influence the unloading curve, the modulus should be consistent. And the consistent modulus is considered to be the modulus of test material. Therefore, it is meaningful to study the modulus convergence as indent depth increases. By using displacement control, Reduced Modulus is chosen to study the convergence as the indent depth increases. Cube Corner probe is used, and 6 different indent depths are chosen, 30 nm, 60 nm, 100 nm, 150 nm, 200 nm, and 250 nm. Then indents are performed at the exact same location, from lower depth to higher depth. The result is shown in Figure 5-8.

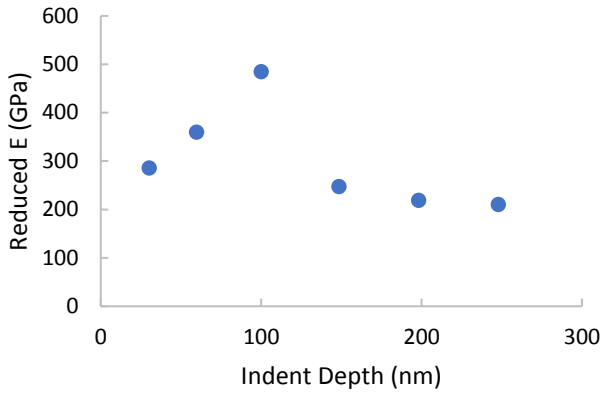

Figure 5-8 Converge study of indent depth

After indentation test, the surface morphology is shown in Figure 5-9. The total scan area is 10μm×10μm and the dimension of indentation area is around 1 μm, as marked in Figure 5-9. It is important to make sure that next indent point is not in the current indentation area. Because the current indentation area has plastic deformation. If next indent point is in this zone, the modulus measured will be affected. Therefore, the distance between indentation points in this study is 1 μm.

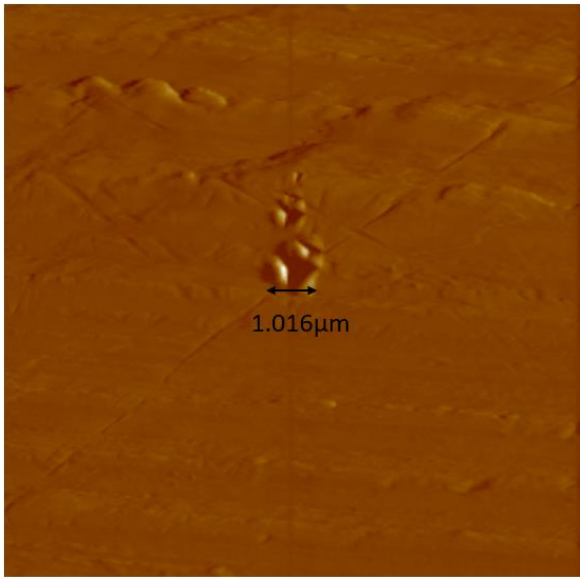

Figure 5-9 Surface scanned after convergence study

Based on the result shown in Figure 5-8, the reduced modulus converges after the indent depth reaches 150 nm. In the following indentation test, 200 nm displacement control is used to test local mechanical property. And the distance between testing point is set to be 1 μm, make sure the current testing area don't overlap with the previous indentation. Thus, the resolution of the interphase thickness is 1 μm.

5.4.3 Mechanical characterization of phases

At the next step, the elastic modulus for each phase was extracted by performing multi point nano indentation on each phase. Therefore, 9 point on the surface of a particle was considered and the average value of elastic modulus was attained. In a same way, but with 5 points of indentation, elastic modulus of PLLA was extracted. Figure 5-10 illustrated the track of indentation for each phase.

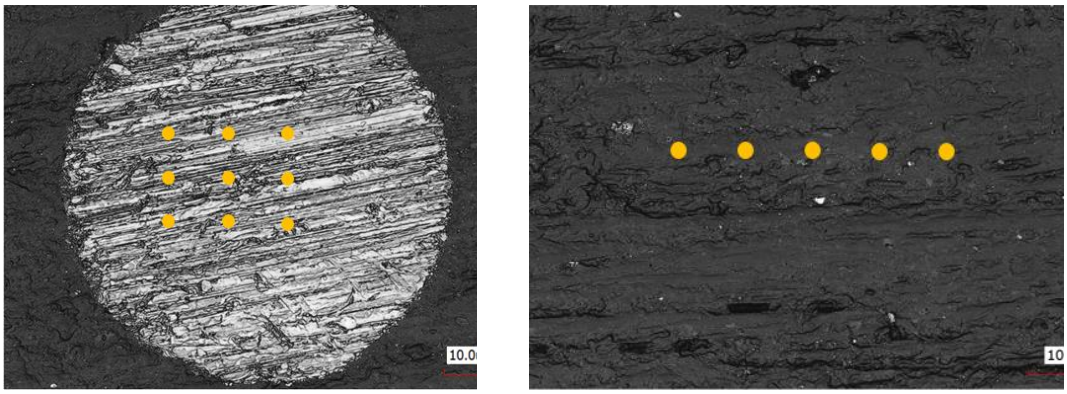

Figure 5-10 Indentation pattern on steel particle (left) and PLLA matrix (right)

Depending on the strain rate, elastic modulus measured by nano indentation can match those measured by tensile or compressive tests or dynamic mechanical analysis (DMA). However, it has been reported that for particle composites the obtained values by the mentioned methods might be different. Cifuentes et al. [238] compared the mechanical

characterization of PLLA/Mg particle composites by compression tests and nano indentation analysis. The former one provided almost identical elastic modulus for the composite but not sensitive to the different volume fractions. On the other hand, the predicted values by nano indentation was directly related to the number of particles in the matrix which was in accordance with composite definition.

Indentation and compression testing diverges in terms of testing geometry and the principle of measurement [239]. The load direction in nano indentation radially evolves from the first contact point, but for compression testing is unidirectional. In indentation testing a combination of compressive, tensile and shear forces are exerted on the material but in compression testing mainly compression stresses are applied [240]. Moreover, high resolution indentation allows to track the variation of elastic modulus for interphase layer.

Microscopic interphases can dramatically alter the macroscopic constitutive response of particle reinforced composites and strongly related to the manufacturing process. According to our knowledge, there is no research about determination of interphase thickness of 3D printed metallic particle composite. In the assumption, the interphase is defined as the transition zone between particle and matrix. Therefore, the mechanical properties (Young's Modulus, Hardness, etc.) of the interphase zone should be lower than particle and higher than the matrix. Because of the aforementioned reason, Young's Modulus is used to find the interphase zone. The Young's Modulus of interphase should converge to Young's modulus of the particle, as testing point approaches to the particle. By using Hysitron TI 950 Triboindenter, we can see the sample through an optical microscope and find the edge, as shown in Figure 5-11. After doing Nano indentation on

the edge point, we measure more points' Modulus towards particle center, as shown by the grey arrow in Figure 5-11.

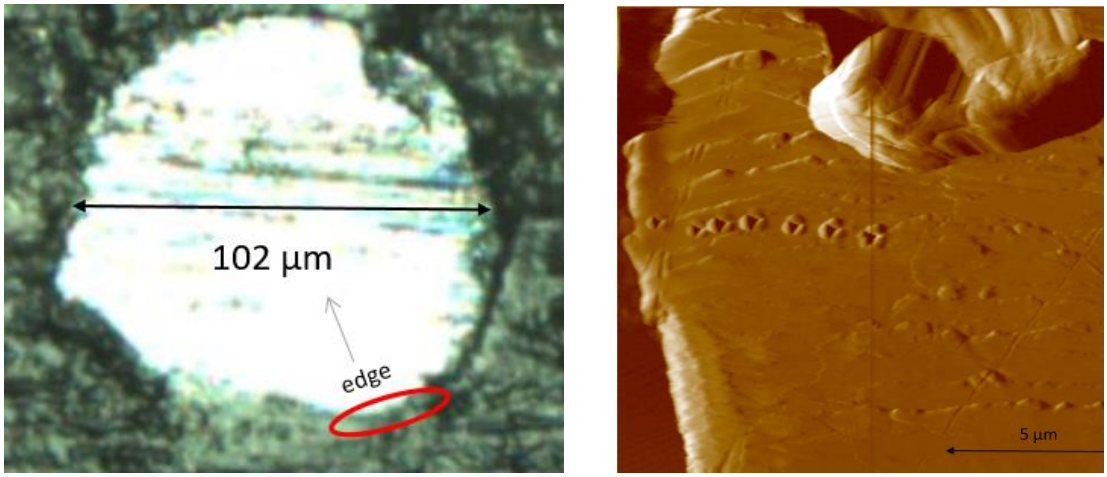

Figure 5-11 SS420 particle under an optical microscope (left); Surface scanned after Nano indent by 15µm× 15µm (right)

The performance of composites is significantly influenced by interactions between the filler particles and the matrix. The interaction term includes bonding strength between the particles and the matrix and also the characteristics of interphase layer. Through our microscopic observations, we did not find any debonding at the interface of particles. However, it is reported that in other manufacturing processes in which the particles are heated, there will be a large deterioration of polymer adjacent to the particles [241]. Therefore, increasing volume fraction of particles, which is supposed to enhance the mechanical response of polymer, accumulate the imperfect bonding and decrease the stiffness of composites.

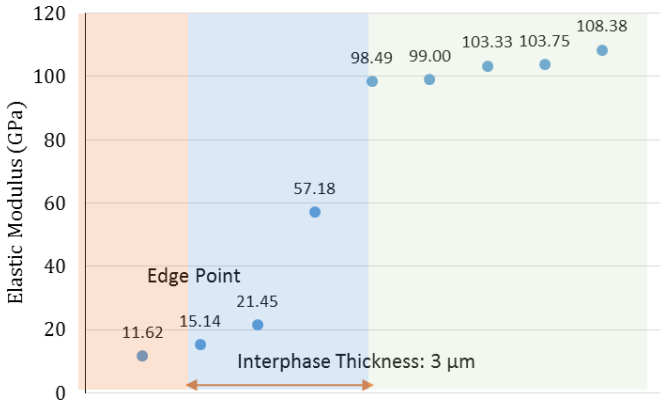

Figure 5-12 Nano indentation response at a region close to the particle's edge

5.4.4 Homogenization of the PLLA /steel composite

The mechanical properties of PLLA/Steel composite can be achieved by homogenization of the RVE model. After examining the elastic modulus of the composite phases, the obtained values were imported into the finite element model, and numerical simulations were conducted.

The role of particles in strengthening of PLLA matrix can be demonstrated by comparing the load sharing of the composites. The load shared by each phase was calculated by integration of all nodal forces along the loading direction, Figure 5-13. Results showed that the load shared by the steel particle increased by 21 % when volume fraction varied from 3 % to 10 %. The contribution of interphase was insignificant which mainly because of the low thickness of this layer.

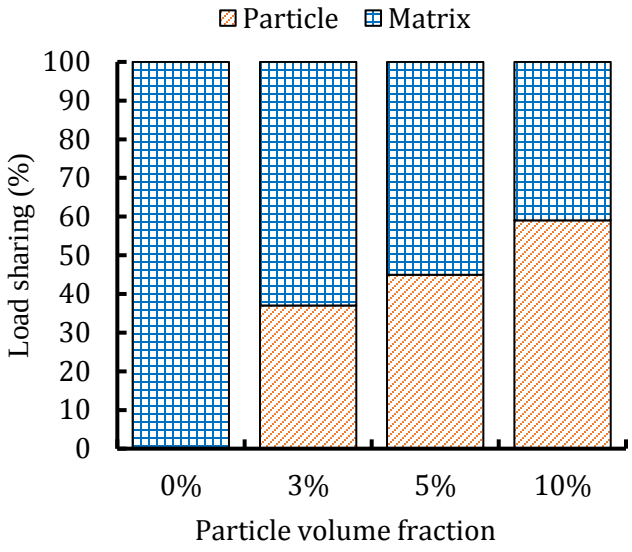

Figure 5-13 Load sharing capacity of the PLLA/steel composites

Degradation of the matrix after a while can cause deterioration of the interphase layer and then debonding of the particles [242]. Existence of the interfacial debonding can lower the strength of the composites and initiate progressive internal damage [243]. Although, we did not observe any debonding of particles for the 3D printed composites, due to the degradability of PLLA polymer over time, we studied the effect of interfacial defects on the performance of 3D printed PLLA/steel composite. In many of the previous studies about debonding and the mechanical properties of composites only one specific loading circumstance has been considered [243-247]. However, this defect might affect differently with respect to the applied loading conditions. In this section the authors have studied the contribution of particle bonding strength in different loading scenarios.

In Figure 5-14, it can be seen that as the particle volume fraction increased to 10 %, the effective elastic modulus of the composite increased by 31 %. Moreover, it can be seen that under this loading condition, debonding of the particles tremendously reduce the

elastic modulus and loading capacity. It is depicted that the obtained values for imperfect bonded particles for all the specimens are lower than that for pure PLLA polymer. This can reveal the importance of manufacturing process of the metallic particle composites and the strength of particle attachments can determine the strength of produced composites. A comparison of the composite with 10 % of particles shows that bonding defects can reduce its elastic modulus by 70 %, while this difference for PLLA/steel with 5 % and 3 % of particles is 29 %, and 17 %, respectively. This proves when degradation of PLLA occurs those composites with higher initial elastic modulus will be the weakest ones which can be accounted as a limitation for embedding higher volume fraction of particles [242].

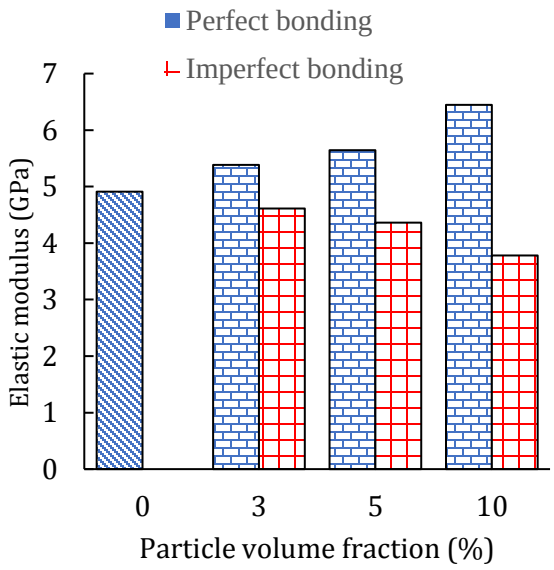

Figure 5-14 the effective elastic modulus of composite under tensile loading

The obtained values of Elastic modulus under uniaxial compressive load is depicted in Figure 5-15. As it is expected, imperfect bonding condition plays a minimal role in variation of elastic modulus. Comaretively, all the PLLA/steel composites have higher elastic modulus than pure PLLA. The largest reduction of elastic modulus can be seen for PLLA/steel with 10 % of particles which is 7.2 %. This results show when the 3D printed

particle composite exposed to the compressive loads, even when PLLA polymer degradation occures, the sustainability of the structure is not affected largely.

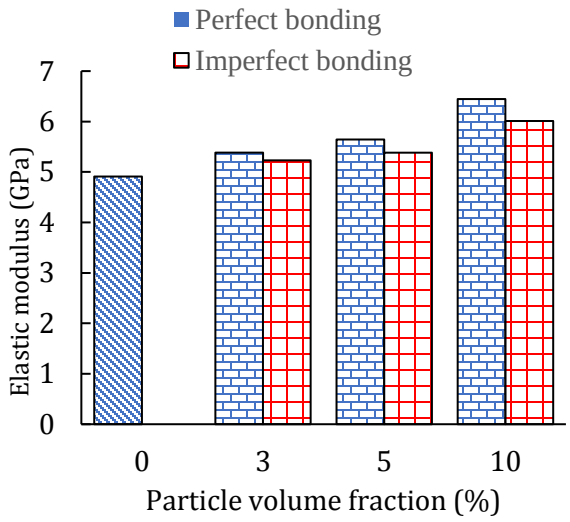

Figure 5-15 the effective elastic modulus of composite under compressive loading

Figure 5-16 shows the Elastic modulus for the PLLA/steel composites under shear loading. The stiffness degradation is also demonstrated which is directly related to the number of particles in PLLA matrix. It can be seen that PLLA/steel with 10 % of particle fraction increased the shear modulus of PLLA polymer up to 26%. In addition, in the worst case, debonding of particles could decrease the shear modulus down to 36 %.

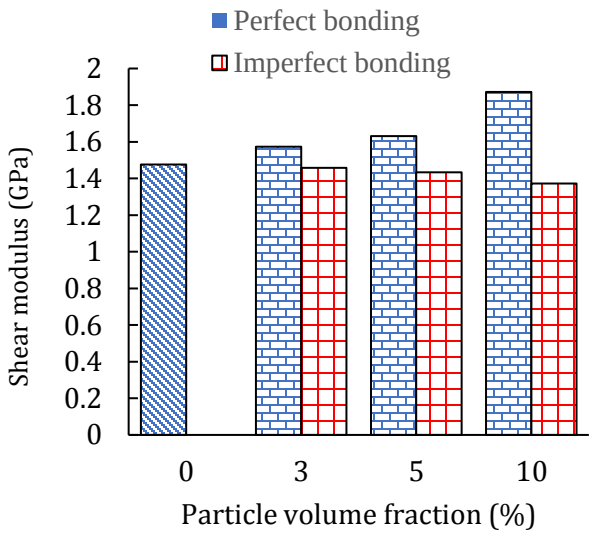

Figure 5-16 the effective elastic modulus of composite under shear loading

In order to have a sharper understanding of the contribution of bonding strength of particles faced different loading conditions, we plotted the stress distribution for the PLLA/steel composite with volume fraction of 3 %, Figure 5-17. It can be seen that when the specimen is exposed tensile load, the induced stresses on sides of the particles dropped considerably and as a result the structure's stiffness decreased and could not withstand the imposed load. On the other hand, in the midst of compression the contact between particles and matrix transmit the applied load throughout the specimen, although there is a small drop of stress values on top and bottom of the particles due to the debonding. Finally, for the shear deformation, detachment of particles at the angle of 45 and 275 with respect to X axis is observable.

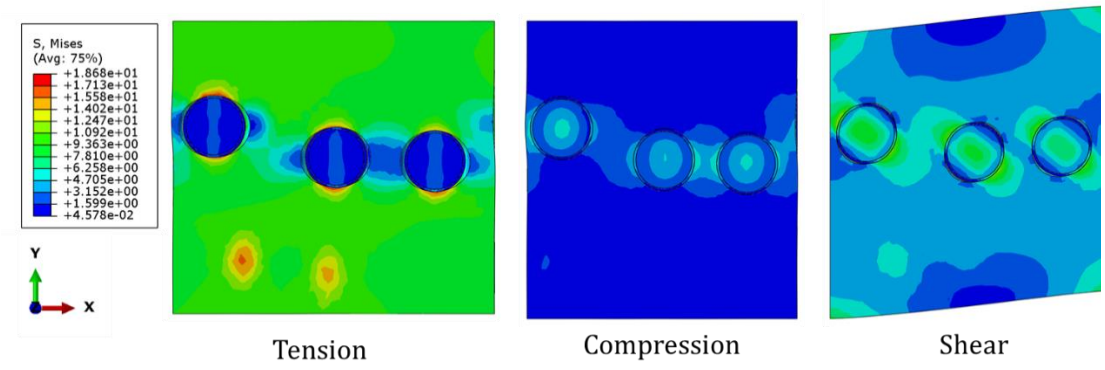

Figure 5-17 Stress distribution of PLLA/steel composite with volume fraction of 3% under different loading scenarios (imperfect bonding)

5.5 Conclusion

In this paper we manufactured a 3D printed PLLA/steel particle composite by using fused filament fabrication method. At the next step, nano-indentation tests were conducted in order to characterize the mechanical properties of the composite. At the last step, a RVE model was generated to determine the elastic modulus of the composite. The following conclusions can be extracted:

- The elastic modulus of 3D printed composite with 10 % of particles was 31 % higher than that for the pure PLLA polymer.
- Perfect bonding of particles was observed for almost all of the samples which stem from the 3D printing method.
- The measured thickness of interphase was considerably lower than the diameter of particles, and a sharp variation of the elastic modulus was observed around the particle's edge.

- The sharing load of particles in the composite with 10 % of particles is approximately 60 %, whereas this value for the composites with less than 10 % of particles is lower than 50 %.
- Degradation of interphase can reduce the elastic modulus of the composite by 70 % and 7% under tensile and compressive loads, respectively.
- Shear modulus of the composite with 10 % of particles decreases by 36 % when debonding occurs. In this case the shear modulus of the composites is lower than that for the pure PLLA polymer.

Chapter 6: Micromechanical Analysis of Bioresorbable PLLA/Mg composites coated with MgO: effects of particle weight fraction, particle/matrix interface bonding strength and interphase

6.1 Introduction

Bioresorbable polymers, such as poly-L-lactic acid (PLLA), has been extensively used in biomedical applications because of its resorption. Specifically the PLLA are attracting increased attention for vascular stent [1]. The first-generation bioresorbable coronary stent was released by Abbott vascular in 2016. However, the disadvantages of these polymers are the inferior mechanical performance, compared to conventional stents made of stainless steel or other metallic materials. Relatively low stiffness of the PLLA stent resulted in a bulky strut profile, which might affect the occurrence of complications following stenting [2]. Kastrati et al. showed that the stent with a thinner strut was associated with a significant reduction in angiographic and clinical restenosis after coronary artery stenting [3].

The particle reinforced composites offer the potential to overcome the low stiffness of bioresorbable polymers [4]. Misra et al. developed a poly-L-caprolactone (PCL) stent reinforced with graphene nanoparticles [2]. It was reported that the presence of 4 wt% graphene nano plates enhanced the Young's modulus of the PCL polymer by 53 %. Jang et al. fabricated the PLGA composite reinforced by magnesium hydroxide particles $Mg(OH)_2$ with various shapes [5]. It was found that $Mg(OH)_2$ fiber provided much more mechanical strength due to the large aspect ratio and surface area, which would enhance the molecular interactions and chemical reactivity. Osman et al. also showed that particles

with large aspect ratio could boost the mechanical properties [6]. On the other hand, bioresorbable reinforcements with a larger surface area to volume ratio would promote the degradation rate and cause detrimental effects on the mechanical properties of composite [7].

The PLLA polymer reinforced by Mg particles have drawn attentions due to desirable mechanical enhancement [8]. However, the PLLA/Mg composites with 10 % of weight fraction exhibited a lower stiffness than the pure PLLA after 28 days of placement, due to the faster degradation of Mg particles than the pure PLLA [9]. When the Mg was used as reinforcement, its fast degradation rate was generally inhibited by various surface modification methods [10], such as the deposition of a coating by microarc oxidation treatment [11], polycaprolactone coating [12], calcium phosphate (CaP) [13], [14]. A systematic study on the role of Mg, especially its coating was needed for designing a desirable biodegradable PLLA/Mg stent.

In this work, we combine the computational the Mori-Tanaka approach [15] with the local characterization of the finite element method [16] to quantify the micromechanical behavior of the PLLA/Mg composites. A 3D representative volume element (RVE) containing randomly distributed Mg particles was developed to estimate the local and global response of PLLA/Mg composites. The influences of particle weight fraction, imperfect bonding between particle and polymer matrix, and MgO coating will be examined in terms of effective Young's modulus and yield strength of the composites as well as the local mechanics.

6.2 Material and Methods

Micromechanical analysis can provide researchers with a range of information on the local and global properties of composite materials [17]. In FEA of randomly reinforced composites, generating homogenous and isotropic RVEs is the main factor in estimating the behavior of models accurately [18, 19]. Hereby, the configuration of the PLLA/Mg composite was represented by a three-dimensional RVE with a length of 123 μm each side, as shown in Figure 1. The Mg particles were randomly distributed within the PLLA polymer matrix. The spherical shape of Mg particles with a radius of 12.3 μm were adopted from the published measurements using a Malvern 2000 laser-scattering particle size analyzer [7]. The Young's modulus of the Mg particle was 44 GPa and Poisson's ratio was 0.35 [20]. The MgO coating between Mg particles and PLLA matrix had the Young's modulus of 330 GPa and a Poisson's ratio of 0.37[21]. The relative coating thickness, i.e., coating thickness vs. Mg radius, were varied from 0.2 to 0.5 in an increment of 0.1. The PLLA polymer had a Young's modulus of 2.26 GPa and a Poisson's ratio of 0.3 [22]. A range of weight fraction from 1% to 15 % was considered to evaluate the load sharing capacity of Mg reinforcements.

The model was meshed with quadratic tetrahedral elements and the element size of 2 μm were chosen. Uniaxial compression in Y-direction was applied by a displacement of 10 μm. A Periodic boundary condition was adopted [23]. Perfect bonding was considered at the interface between the Mg and the MgO. The imperfect bonding was assumed with a tangential sliding with the friction coefficient of 0.2 in other cases.

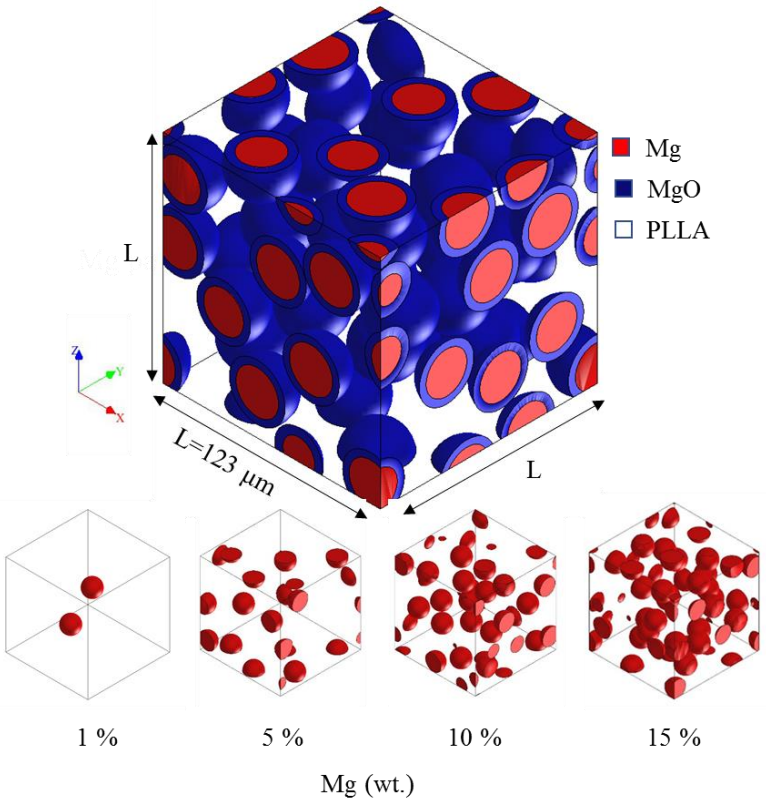

Figure 6-1 Three-dimensional representative volume element at different weight fractions of Mg particles.

6.3 Results

6.3.1 Model validation

The effective Young's modulus of the PLLA/Mg composite obtained from our RVE models was compared against the results from the published indentation testing results [9] as well as the analytical solution from the Mori-Tanaka approach [15].

The principle of the Mori-Tanaka approach is that the average strain in the particles of a two-phase material could be estimated by the solution for a single particle embedded in an infinite medium subjected to a remote uniform stain within the matrix [24]. The

effective Young's modulus (E_e) for a composite reinforced by spherical particles was calculated as the following:

$$E_e = \frac{9\tilde{K}_c\tilde{G}_c}{3\tilde{K}_c + \tilde{G}_c} \quad (1)$$

$$\tilde{K}_c = \tilde{K}_m + \frac{V_p\tilde{K}_m(\tilde{K}_p - \tilde{K}_m)}{\tilde{K}_m + \beta_2(1 - V_p)(\tilde{K}_p - \tilde{K}_m)} \quad (2)$$

$$\tilde{G}_c = \tilde{G}_m + \frac{V_p\tilde{G}_m(\tilde{G}_p - \tilde{G}_m)}{\tilde{G}_m + \beta_1(1 - V_p)(\tilde{G}_p - \tilde{G}_m)} \quad (3)$$

$$\beta_1 = \frac{2(4-5\nu_m)}{15(1-\nu_m)}, \beta_2 = 3 - 5\beta_1 \quad (4)$$

where $\tilde{K}$ and $\tilde{G}$ denote the bulk modulus and shear modulus. The subscripts "m" and "p" stand for the matrix and particles, respectively. Also, V_p is the volume fraction of particle, i.e., the weight fraction multiplied by the ratio of the matrix to particle density. ν is the Poisson's ratio.

Figure 6-2 depicts the comparison among our RVE models, published experiments, and the analytical solution from the Mori-Tanaka approach. It is clear that our model predictions are congruous with the experimental data as well as the analytical derivations. The maximum variation among three different approaches was less than 9 %, which occurred at the Mg weight fraction of 15%. Moreover, as the Mg weight fraction increased from 1% to 15%, the effective Young's modulus of the composites increased by 28.9 %.

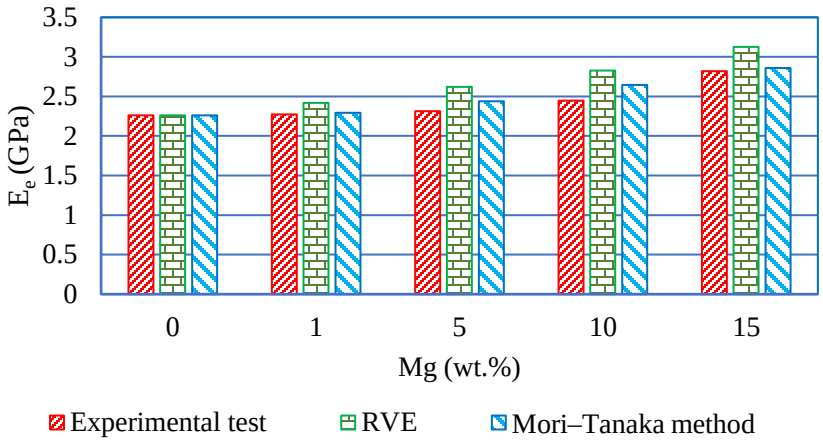

Figure 6-2 Comparison of the effective Young's modulus (E_e) obtained from the representative volume element model, experimental data, and the analytical derivations from the Mori-Tanaka approach.

6.3.2 Effect of bonding condition at the PLLA/Mg interface

During the fabrication process of PLLA/Mg composites, There existed thermal degradation and hydrolysis of PLLA [9] and potential deterioration of bonding strength between PLLA and Mg. Two bonding conditions at the PLLA/Mg interface were then considered. One was with the perfect bonding, and the other allowed tangential sliding with a friction coefficient of 0.2, hereby referred to as the imperfect bonding.

The effective Young's modulus and yield strength were obtained as shown in Figure 6-3. A profound enhancement of effective Young's modulus was observed for PLLA/Mg with the perfect bonding. However, the imperfect bonding between Mg particles and PLLA matrix resulted in a diminished modulus. Specifically, the effective Young's modulus of the composite with 15 wt% of Mg, compared with the one with 1 wt% of Mg, increased approximately 28.9 % and 15.24 % for the perfect and imperfect bonding conditions, respectively. Moreover, the imperfect bonding reduced caused 2.7 % decrease in the yield strength of the composites as the wt% of Mg increased from 1% to 15%. On the contrary,

the perfect bonding condition enhanced the composite's yield strength. The 15 wt% of Mg could strengthen the yield strength of the composites by 9.5 %.

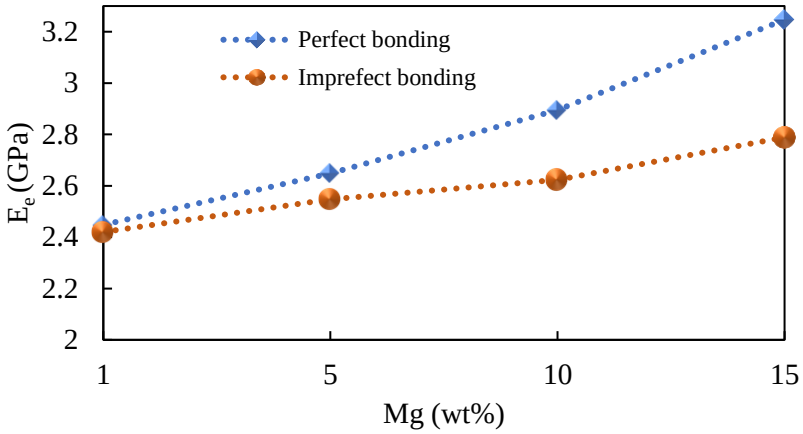

(a)

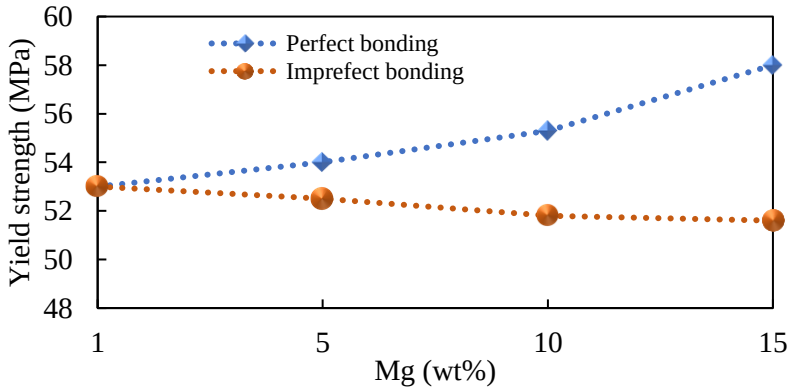

(b)

Figure 6-3 The effect of bonding intensity on (a) Effective Young's modulus; (b) and yield strength of PLLA/Mg composites.

The observed responses of the composite for different bonding conditions was further illustrated by contour plots of von Mises stress at the PLLA/Mg interface (Figure 6-4). A continuous stress distribution from the matrix to the inclusion was observed for the perfect bonding condition. The peak of the stress was 0.112 GPa, located at the center of

the particle. Much smaller stresses were observed in the Mg particle for the imperfect bonding, especially at the edge of the particle. The peak von Mises stress at the center of the particle was 0.083 GPa, which is 35 % less than that for perfect bonding. Moreover, debonding was clearly visualized at the interface between the Mg particle and the PLLA matrix. This led to the abrupt changes of von Mises stress at the interface. At the same time, the peak von Mises stress in the matrix was 0.055 GPa, compared to the 0.050 GPa for the perfect bonding case. This indicate that the PLLA matrix undertook more loads.

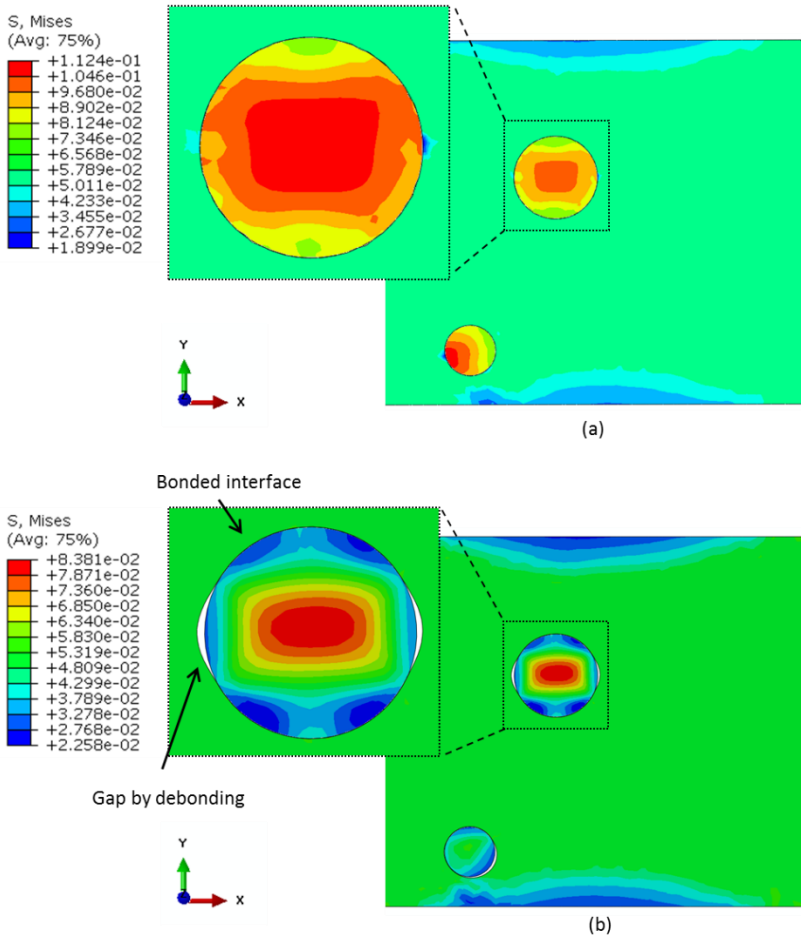

Figure 6-4 Contour plots of Mises stresses (GPa) of PLLA/Mg with Mg (wt. 1%) for perfect and imperfect bonding conditions

The role of bonding strength on the load-sharing capacity of the PLLA matrix and Mg particles was illustrated in Figure 6-5. The load shared by each phase was calculated by the integration of all nodal forces along the loading direction (Y-axis). Results demonstrated that the load shared by the Mg particles increased 52 %, when Mg weight fraction varied from 1 to 15 wt% with the perfect bonding condition. The matrix undertook almost the entire loading at 1 wt% of Mg. However, for the imperfect bonding condition, the loading sharing capacity of the Mg particles was less efficient, and the matrix have to undertake more load. Specifically, the load shared by the 15 wt% of Mg was 61 % considering the perfect bonding, while it decreased to 47.5 % for the imperfect bonding condition.

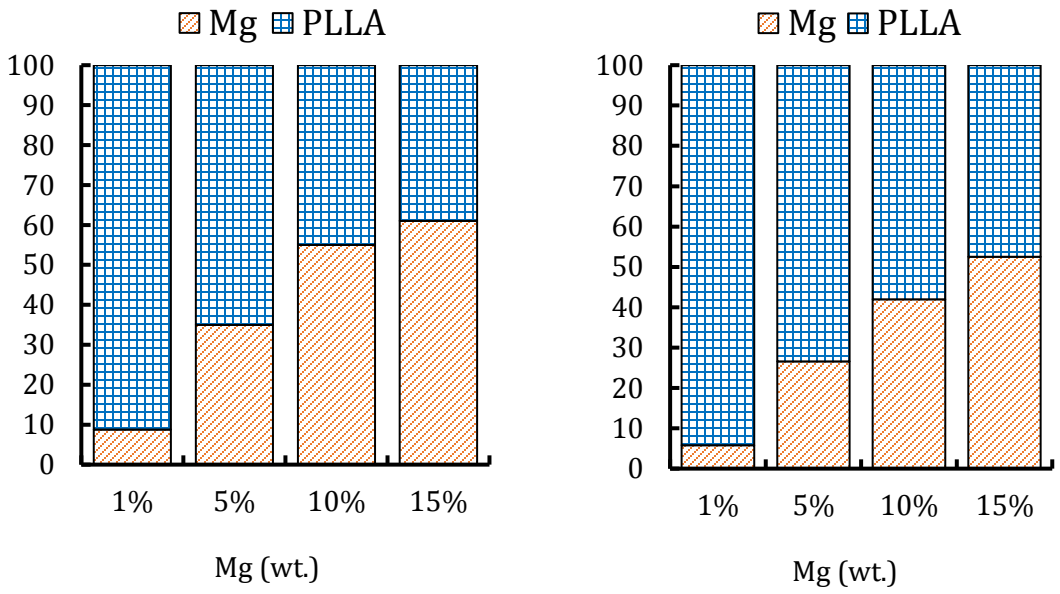

Figure 6-5 Effect of bonding strength on the load-sharing capacity of the PLLA/Mg composites, left) Perfect bonding; right) Imperfect bonding

6.3.3 Effect of MgO interphase

The MgO interphase is a region of finite size between PLLA matrix and Mg particles, and it has a different property than two main phases [20]. It was responsible for transferring

load from matrix to particle inclusions. The effect of MgO interphase on the effective Young's modulus of the composite was evaluated for different relative thickness (0.2, 0.3, 0.4, 0.5), as shown in Figure 6-6. The perfect bonding condition at all interfaces was considered. It was clear that the MgO interphase layer significantly boosted the stiffness of the composites. For the 15 wt% of Mg, the effective Young's modulus of the PLLA/Mg-MgO (0.5) was 5.38 GPa, which is 65.6 % larger than that without interphase, and 138% larger than that of pure PLLA polymer. The MgO interphase had a much larger influence on the composite with a higher weight fraction of Mg.

The yield strength of the composite was also enhanced with the consideration of MgO interphase (Figure 6-7). For the 15 wt% of Mg, the yield strength of PLLA/Mg-MgO (0.5) is 139 MPa and approximately 139 % higher than that without considering the interphase. Compared to the pure PLLA polymer, the MgO interphase could boost the yield strength of the composite up to 170 %.

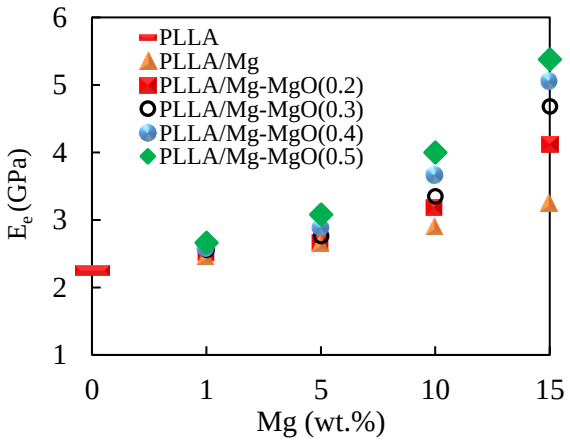

Figure 6-6 the influence of MgO coating layer on effective Young's modulus of the composites with different Mg weight fractions.

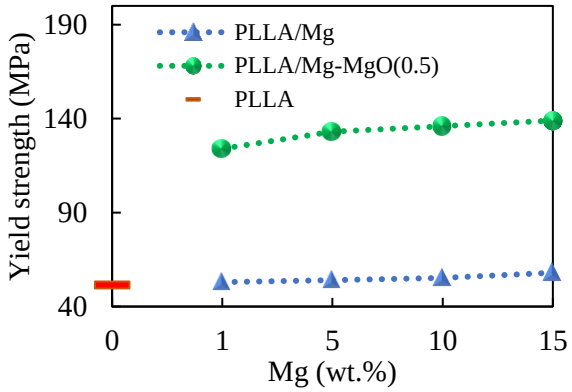

Figure 6-7 the influence of MgO coating layer on the yield strength of the composites with different Mg weight fractions.

6.4 **Discussions**

In this work, the effect of Mg particle reinforcement on the PLLA polymer was studied through micromechanical modeling. It was well known that particle reinforced composites exhibit relatively isotropic properties compared to short fiber or whisker reinforced composites. The properties of these composites can be tailored by adjusting fabrication techniques with various parameters such as reinforcement particle properties, size, distribution, weight or volume fraction, and/or matrix properties [25]. Cifuentes et al. [26] fabricated a variety of PLLA/Mg composites and characterized that particle strengthening effect decreased with a larger weight fraction of Mg particles. It was speculated that during the fabrication process of the composites, Mg particles promote certain degree of thermal degradation of PLLA molecules, which counterbalance with the strengthening effect of particle weight fraction. For the PLLA/Mg composites with less than 5 wt% of Mg, the particle strengthening effect exceeded the thermal degradation effect, which strengthen the composites. However, for the PLLA/Mg composites with more than 5 wt% of Mg, the thermal degradation effect surpasses the particle strengthening effect, and thus a decrease

in the effective modulus of the PLLA/Mg composite. It is necessary to regulate the thermal degradation of Mg particles during the fabrication process. The recent work from the same group [9] addressed the deterioration effect of Mg particles based on the temperature dependency of each phase and demonstrated an improved stiffness for the PLLA/Mg composites with more than 5 wt% of Mg.

In this study, our computational models were developed based on the published experimental evidence [9]. We have considered two level of bonding strength between Mg particles and PLLA. The weak bonding mimicked the thermal deterioration effect during fabrication process. Our results have shown that the compressive yield strength and effective Young's modulus of the composites with imperfect bonding decreased around 12.4 % and 16 %, respectively, compared with the perfect bonding conditions. Moreover, the imperfect bonding decreases the level of variation of effective Young's modulus with respect to the weight fraction of particles. This agree with the work by Hua et al. [23], which stated that a perfect bonding assumption could lead to an overestimation of the effective Young's modulus of composites.

Fast degradation rate of magnesium particles is a serious concern for composites with more than 10 wt% of Mg. To overcome this drawback, several surface modification techniques, including the chemical deposition and microarc oxidation techniques, have been introduced to control the degradation rate of Mg [27]. The long-term in vitro degradation behavior of the composites was further examined through the immersion in SBF solution for different time periods. It is well known that the overall corrosion reaction of magnesium in aqueous solution at its corrosion potential is directly related to the released hydrogen gas, caused by chemical reactions. Figure 6-8 shows the cumulative

hydrogen gas evolution diagrams for uncoated, MgO-coated and Si/MgO-coated microcomposites.

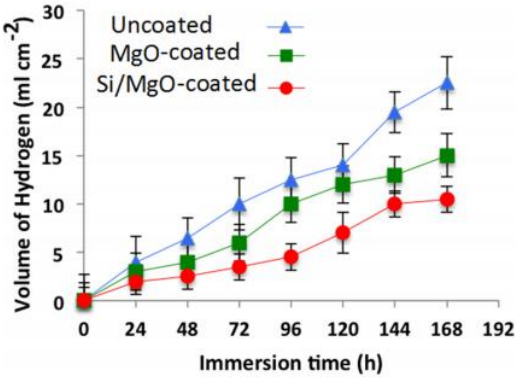

Figure 6-8 Hydrogen evolution during immersion of uncoated, MgO-coated and Si/MgO-coated in SBF solution for duration of 168 h [28].

The coating layers exhibited its efficiency to decrease the hydrogen evolution significantly and thus the degradation rate of Mg particles. Zamani et al. studied biodegradable Mg microcomposite coated with MgO in terms of corrosion rate, surface characterization, and biocompatibility [28].

The documented data on the MgO coating focused on the quantification of its role on regulating the degradation and corrosion of Mg, our results on the load sharing effect of MgO coating provided new insights on the mechanical properties of PLLA/Mg composite. Due to its rigidity, it was observed that adding MgO coating with a relative thickness of 0.5 could increase the effective Young's modulus of the composite with 15 wt% of Mg particles by 138 %. In addition, the yield strength of PLLA/Mg-MgO with 15 wt% of Mg particles and a relative thickness of 0.5 is 139 % and 170 % higher than that of PLLA/Mg and neat PLLA, respectively.

6.5 Conclusions

The micromechanical analysis of PLLA/Mg composite were performed to quantify the effects of particle weight fraction, particle/matrix interface bonding strength, and MgO interphase on the mechanical properties of the biodegradable composite. The model was validated by the published indentation tests [9] as well as the analytical solution [15]. The computational results towards the optimal design of PLLA/Mg composites were summarized as:

- Imperfect bonding of Mg particles could drastically weaken the mechanical properties of PLLA/Mg composite. The yield strength was reduced by 12 %. This indicated the importance of the fabrication process.
- The MgO coating or interphase layer between PLLA and Mg was intent to mitigate the degradation rate of Mg particles. In addition, it also enhanced the effective Young's modulus and yield strength of the composites by 65.6 %, and 139 %, respectively.
- The PLLA polymer reinforced with coated Mg particles can benefit from 138 % and 170 % enhancement of its effective Young's modulus and yield strength, respectively.

Conclusion and future work

Formation of arterial plaque and stenosis is one of the main cardiovascular disease risk factors. Stenting is a popular approach to increase the inner diameter of artery and provide an acceptable lumen gain. This is achieved by applying internal pressure to the arterial wall. Despite the desirable outcomes of this procedure there are complexities and challenges that are being discussed among scholars in this area. Occurring restenosis is one of the complications in which smooth muscles cell start proliferation and remodeling in response of induced mechanical stresses. Another important point of view is the placement of stent and possible migration due to the continuous deformation and special contact situation between tissue and stent struts. Finally, the mechanical properties of stent and application of novel material in order to excel its performance are the critical topics that also have been elaborated in the current research work through different chapters. In the present work, the relative movement of the braided wires was constrained to mimic the covering effect commonly used in commercial esophageal stents. The anatomical details of the esophagus including the stellate appearance of the inner esophageal layer was simplified as an esophagus tube with a friction coefficient. A range of friction coefficients were used depending on relative movement between the stent and the esophageal wall. A larger friction coefficient was commonly associated with the less migration risk. The feasibility of the model was validated in our previous work. The esophagus was modeled as a one-layer tube, although it is assumed as two layer or three-layer wall depending on the aim of the study. The detailed configurations of esophageal wall could alter our results in terms of magnitudes, but the comparative results between two stent designs was

expected to be the same. The material properties of the esophagus and cancerous tissue were assumed to be homogeneous isotropic materials, although they are anisotropic. The perfect plasticity for cancerous tissue was assumed due to lack of experimental data. More realistic models considering patient-specific geometry and anisotropic three-layered esophageal wall properties would change the contact force and the migration resistance force. The existence of pre-stretch along axial and circumferential directions at physiological conditions as well as the esophageal muscle contraction were not explicitly incorporated in our model, we speculate that the both pre-stretch and wall contraction were associated with the reduced friction between stent and esophagus, and thus a higher migration rate. Despite these simplifications, this work demonstrated the importance of the stent design on the risk of migration, which might have significant clinical implications. This work could be used to provide a fundamental understanding of the behavior and impact of stent design on the esophageal wall, provide guidance for optimizing stent shape and surface profiles, and illuminate the possibilities for exploiting their potential to prevent migration.

Another complication about stenting is restenosis which can be related to the mechanical response of VSMC. In view of VSMCs cytoskeleton, it was noted that stress fibers have the major contribution in VSMCs contraction, however, microtubules and intermediate filaments can indirectly affect contractility of the cells. In addition, the cytoskeleton responses are strongly related to the interaction of integrin receptors and extracellular matrix. VSMCs alter their proliferation and contractility or change their phenotype with respect to the mechanical environment, such as 2D or 3D ECM, and level of cyclic strains. Specifically, the cultured VSMCs change their phenotype compared with

in vivo conditions. The responses of VSMCs subjected to cyclic loading is dependent on the time period of the applied load. The mechanics of VSMCs could be better delineated using numerical simulation. The interaction between collagen and non-fibrillar matrix, alignment and recruitment of collagen fibers and induced stresses in VSMCs during extension have been elucidated. However, the load sharing capacity of VSMCs in Lamellar unit as well as the influence of phenotype changing on the VSMCs contribution in arterial stiffness remained to be determined. The focus of this review work was on the tunica media as this layer is the thickest one and has the greatest contribution on the arterial stiffness. However, the contribution of tunica adventitia and intima, which are placed on the outer and inner sides of the tunica media, should not be neglected. Adventitia is the strong outer coverage which composed of connective tissue as well as collagen and elastin fibers. These fibers prevent the arterial wall from overexpansion. The most abundant cell type in adventitia is the fibroblast, which synthesize the extracellular matrix and collagen fibers. The stiffness of fibroblast cell has been measured between 1-27 kPa. This range is comparable with VSMCs in relaxed state; however, the number of fibroblasts is much smaller than VSMCs in arterial wall (due to the large thickness of tunica media) which decreases their contribution in the total arterial stiffness. One the other side, intima is composed of an elastic membrane lining and endothelium (an exceedingly thin single sheet of endothelial cells). The mechanical contribution of endothelium is not significant (stiffness between 1-2 kPa), however, endothelial cell signaling plays an important role in contraction and relaxation of VSMCs and arterial stiffness.

Moreover, we have developed an RVE model based on the lamellar unit of the media layer in the aortic wall. The developed model helped us to distinguish the load sharing

capacity of fibrous and non-fibrous parts of the LU. In addition, micro-structural variation of the LU was analyzed, and the corresponding macro-structural behavior was studied through multi-scale modeling of the aortic wall. Our results showed that the VSMC can take up to 30 % of the applied load when contracted. It is known that the relaxed VSMC is around 10 times softer than the contracted one, which affects its contribution in load sharing of the LU. On the other side, the contribution of collagen fibers at low stretch levels was negligible but became predominant when straightened in high stretches. The obtained uniaxial response of the LU was validated against the previous experimental data. The macro-scale model of the aorta allowed us to evaluate the arterial expansion with respect to the micro-structural variation of the lamellar unit. Finally, aging effects by collagen deposition was modeled and aortic dilation was estimated. It was revealed that stiffening of the VSMC when the aorta is exposed to high pressure does not affect the aortic stiffness but is mainly controlled by collagen fibers. Our findings can shed some light about the contribution of VSMCs in arterial stiffness which has been under debate in recent years.

In addition, we manufactured a 3D printed PLLA/steel particle composite by using fused filament fabrication method. At the next step, nano-indentation tests were conducted in order to characterize the mechanical properties of the composite. At the last step, a RVE model was generated to determine the elastic modulus of the composite. The elastic modulus of 3D printed composite with 10 % of particles was 31 % higher than that for the pure PLLA polymer. Also, Perfect bonding of particles was observed for almost all of the samples which stem from the 3D printing method. The measured thickness of interphase was considerably lower than the diameter of particles, and a sharp variation of the elastic modulus was observed around the particle’s edge. The sharing load of particles in the

composite with 10 % of particles is approximately 60 %, whereas this value for the composites with less than 10 % of particles is lower than 50 %. Degradation of interphase can reduce the elastic modulus of the composite by 70 % and 7% under tensile and compressive loads, respectively. Shear modulus of the composite with 10 % of particles decreases by 36 % when debonding occurs. In this case the shear modulus of the composites is lower than that for the pure PLLA polymer.

The micromechanical analysis of PLLA/Mg composite were performed to quantify the effects of particle weight fraction, particle/matrix interface bonding strength, and MgO interphase on the mechanical properties of the biodegradable composite. The model was validated by the published indentation tests as well as the analytical solution. Imperfect bonding of Mg particles could drastically weaken the mechanical properties of PLLA/Mg composite. The yield strength was reduced by 12 %. This indicated the importance of the fabrication process. The MgO coating or interphase layer between PLLA and Mg was intent to mitigate the degradation rate of Mg particles. In addition, it also enhanced the effective Young's modulus and yield strength of the composites by 65.6 %, and 139 %, respectively. The PLLA polymer reinforced with coated Mg particles can benefit from 138 % and 170 % enhancement of its effective Young's modulus and yield strength, respectively.

References

1. Stewart, J., G. Manmathan, and P. Wilkinson, *Primary prevention of cardiovascular disease: A review of contemporary guidance and literature.* JRSM cardiovascular disease, 2017. **6**: p. 2048004016687211-2048004016687211.
2. Thoenes, M., et al., *Patient screening for early detection of aortic stenosis (AS)-review of current practice and future perspectives.* Journal of thoracic disease, 2018. **10**(9): p. 5584-5594.
3. Balk, E., et al., *Effectiveness of Management Strategies for Renal Artery Stenosis: A Systematic ReviewComparative Effectiveness of Management Strategies for Renal Artery Stenosis.* Annals of Internal Medicine, 2006. **145**(12): p. 901-912.
4. Chimowitz, M.I., et al., *Stenting versus Aggressive Medical Therapy for Intracranial Arterial Stenosis.* New England Journal of Medicine, 2011. **365**(11): p. 993-1003.
5. Kuntz, R.E., et al., *Novel approach to the analysis of restenosis after the use of three new coronary devices.* Journal of the American College of Cardiology, 1992. **19**(7): p. 1493-1499.
6. Azevedo, L.C.P., et al., *Oxidative stress as a signaling mechanism of the vascular response to injury: The redox hypothesis of restenosis.* Cardiovascular Research, 2000. **47**(3): p. 436-445.
7. Ward Michael, R., et al., *Arterial Remodeling.* Circulation, 2000. **102**(10): p. 1186-1191.
8. Bennett, M.R. and M. O'Sullivan, *Mechanisms of angioplasty and stent restenosis: implications for design of rational therapy.* Pharmacology & Therapeutics, 2001. **91**(2): p. 149-166.
9. Li, C. and Q. Xu, *Mechanical stress-initiated signal transductions in vascular smooth muscle cells.* Cellular Signalling, 2000. **12**(7): p. 435-445.
10. Diller, R., et al., *Stent migration necessitating surgical intervention.* Surgical Endoscopy And Other Interventional Techniques, 2003. **17**(11): p. 1803-1807.
11. Shim, C.S., et al., *Fixation of a Modified Covered Esophageal Stent: Its Clinical Usefulness for Preventing Stent Migration.* Endoscopy, 2001. **33**(10): p. 843-848.
12. Mai, Y.-W. and Z.-Z. Yu, *Polymer nanocomposites*. 2006: Woodhead publishing.
13. Shaikh, M., et al., *Engineering stent based delivery system for esophageal cancer using docetaxel.* Molecular pharmaceutics, 2015. **12**(7): p. 2305-2317.
14. Sjoquist, K.M., et al., *Survival after neoadjuvant chemotherapy or chemoradiotherapy for resectable oesophageal carcinoma: an updated meta-analysis.* The lancet oncology, 2011. **12**(7): p. 681-692.
15. Jin, Z., et al., *A PTX/nitinol stent combination with temperature-responsive phase-change 1-hexadecanol for magnetocaloric drug delivery: Magnetocaloric drug release and esophagus tissue penetration.* Biomaterials, 2018. **153**: p. 49-58.
16. Lazaraki, G., I. Pilpilidis, and P. Katsinelos, *Polyflex stents for malignant esophageal strictures: An overview.* Annals of Gastroenterology, 2010. **23**(1): p. 17-23.
17. Park, J.-H., et al., *Migration of retrievable expandable metallic stents inserted for malignant esophageal strictures: incidence, management, and prognostic factors in 332 patients.* American Journal of Roentgenology, 2015. **204**(5): p. 1109-1114.
18. Hindy, P., et al., *A Comprehensive Review of Esophageal Stents.* Gastroenterology & Hepatology, 2012. **8**(8): p. 526-534.

19. Homann, N., et al., *Delayed Complications after Placement of Self-Expanding Stents in Malignant Esophageal Obstruction: Treatment Strategies and Survival Rate.* Digestive Diseases and Sciences, 2008. **53**(2): p. 334-340.
20. Wu, W.C., et al., *Silicone-covered self-expanding metallic stents for the palliation of malignant esophageal obstruction and esophagorespiratory fistulas: Experience in 32 patients and a review of the literature.* Gastrointestinal Endoscopy. **40**(1): p. 22-33.
21. Vanbiervliet, G., et al., *The role of clips in preventing migration of fully covered metallic esophageal stents: a pilot comparative study.* Surgical Endoscopy, 2012. **26**(1): p. 53-59.
22. Franco, K.L. and J.B. Putnam, *Advanced therapy in thoracic surgery*. 2nd ed. 2005, Hamilton: B.C. Decker Inc. xiii, 548 p.
23. Sharma, P. and R. Kozarek, *Role of esophageal stents in benign and malignant diseases.* The American journal of gastroenterology, 2010. **105**(2): p. 258.
24. Kajzer, W., M. Kaczmarek, and J. Marciniak, *Biomechanical analysis of stent–oesophagus system.* Journal of Materials Processing Technology, 2005. **162-163**: p. 196-202.
25. Peirlinck, M., et al., *An in silico biomechanical analysis of the stent–esophagus interaction.* Biomechanics and Modeling in Mechanobiology, 2018. **17**(1): p. 111-131.
26. Zhao, S., X. Liu, and L. Gu, *The Impact of Wire Stent Fabrication Technique on the Performance of Stent Placement.* Journal of Medical Devices-Transactions of the Asme, 2012. **6**(1).
27. García, A., E. Peña, and M.A. Martínez, *Influence of geometrical parameters on radial force during self-expanding stent deployment. Application for a variable radial stiffness stent.* Journal of the Mechanical Behavior of Biomedical Materials, 2012. **10**(Supplement C): p. 166-175.
28. De Beule, M., et al., *Realistic finite element-based stent design: The impact of balloon folding.* Journal of Biomechanics, 2008. **41**(2): p. 383-389.
29. Lally, C., F. Dolan, and P.J. Prendergast, *Cardiovascular stent design and vessel stresses: a finite element analysis.* Journal of Biomechanics, 2005. **38**(8): p. 1574-1581.
30. Yassi, R., et al., *Modeling of the Mechanical Function of the Human Gastroesophageal Junction Using an Anatomically-Realistic Three-Dimensional Model.* Journal of biomechanics, 2009. **42**(11): p. 1604-1609.
31. Liao, D., et al., *Two-layered quasi-3D finite element model of the oesophagus.* Medical Engineering and Physics, 2004. **26**(7): p. 535-543.
32. Yang, W., et al., *Finite element simulation of food transport through the esophageal body.* World Journal of Gastroenterology: WJG, 2007. **13**(9): p. 1352.
33. Zhao, S., L. Gu, and S.R. Froemming, *Performance of Self-Expanding Nitinol Stent in a Curved Artery: Impact of Stent Length and Deployment Orientation.* Journal of Biomechanical Engineering, 2012. **134**(7): p. 071007-071007-6.
34. Zhao, S., L. Gu, and S.R. Froemming, *Finite Element Analysis of the Implantation of a Self-Expanding Stent: Impact of Lesion Calcification.* Journal of Medical Devices, 2012. **6**(2): p. 021001-021001-6.
35. Rebelo, N., N. Walker, and H. Foadian. *Simulation of implantable nitinol stents*. in *Abaqus user's conference*. 2001.
36. Natali, A.N., E.L. Carniel, and H. Gregersen, *Biomechanical behaviour of oesophageal tissues: Material and structural configuration, experimental data and constitutive analysis.* Medical Engineering & Physics, 2009. **31**(9): p. 1056-1062.
37. Lu, X. and H. Gregersen, *Regional distribution of axial strain and circumferential residual strain in the layered rabbit oesophagus.* Journal of Biomechanics, 2001. **34**(2): p. 225-233.

38. Lin, C.X., et al., *Friction behavior between endoscopy and esophageal internal surface.* Wear, 2017. **376-377**: p. 272-280.
39. Tan, L., et al., *A method for investigating the mechanical properties of intracoronary stents using finite element numerical simulation.* International Journal of Cardiology, 2001. **78**(1): p. 51-67.
40. Zhao, S., X. Liu, and L. Gu, *The Impact of Wire Stent Fabrication Technique on the Performance of Stent Placement.* Journal of Medical Devices, 2012. **6**(1): p. 011007-011007-4.
41. Van der Heiden, K., et al., *The effects of stenting on shear stress: relevance to endothelial injury and repair.* Cardiovascular Research, 2013. **99**(2): p. 269-275.
42. Saranovic, D., et al., *Fluoroscopically guided insertion of self-expandable metal esophageal stents for palliative treatment of patients with malignant stenosis of esophagus and cardia: comparison of uncovered and covered stent types.* Diseases of the Esophagus, 2005. **18**(4): p. 230-238.
43. Song, H.-Y., et al., *Covered, expandable esophageal metallic stent tubes: experiences in 119 patients.* Radiology, 1994. **193**(3): p. 689-696.
44. Verschuur, E.M., et al., *A new esophageal stent design (Niti-S stent) for the prevention of migration: a prospective study in 42 patients.* Gastrointestinal endoscopy, 2006. **63**(1): p. 134-140.
45. R., J.M. and C.C. O., *A study of the geometrical and mechanical properties of a self-expanding metallic stent—theory and experiment.* Journal of Applied Biomaterials, 1993. **4**(1): p. 77-85.
46. Stavropoulou, E.A., Y.F. Dafalias, and D.P. Sokolis, *Biomechanical behavior and histological organization of the three-layered passive esophagus as a function of topography.* Proceedings of the Institution of Mechanical Engineers, Part H: Journal of Engineering in Medicine, 2012. **226**(6): p. 477-490.
47. Mughal, M.M., M. Marples, and J. Bancewicz, *Scintigraphic assessment of oesophageal motility: what does it show and how reliable is it?* Gut, 1986. **27**(8): p. 946-953.
48. Kou, W., et al., *A fully resolved active musculo-mechanical model for esophageal transport.* Journal of computational physics, 2015. **298**: p. 446-465.
49. Kou, W., et al., *Simulation studies of circular muscle contraction, longitudinal muscle shortening, and their coordination in esophageal transport.* American Journal of Physiology - Gastrointestinal and Liver Physiology, 2015. **309**(4): p. G238-G247.
50. Liu, J., et al., *A novel biodegradable esophageal stent: results from mechanical and animal experiments.* American Journal of Translational Research, 2016. **8**(2): p. 1108-1114.
51. Qiu, H., et al., *Vascular Smooth Muscle Cell Stiffness as a Mechanism for Increased Aortic Stiffness with Aging.* Circulation research, 2010. **107**(5): p. 615-619.
52. Zhao, S., L. Gu, and S.R. Froemming, *Experimental investigation of the stent–artery interaction.* Journal of Medical Engineering & Technology, 2013. **37**(7): p. 463-469.
53. Zhao, J., et al., *Biomechanical properties of esophagus during systemic treatment with epidermal growth factor in rats.* Annals of biomedical engineering, 2003. **31**(6): p. 700-709.
54. Fan, Y., H. Gregersen, and G.S. Kassab, *A two-layered mechanical model of the rat esophagus. Experiment and theory.* Biomedical engineering online, 2004. **3**(1): p. 40.
55. Yang, W., et al., *Instability of the two-layered thick-walled esophageal model under the external pressure and circular outer boundary condition.* Journal of biomechanics, 2007. **40**(3): p. 481-490.

56. Sokolis, D.P., *Structurally-motivated characterization of the passive pseudo-elastic response of esophagus and its layers.* Computers in Biology and Medicine, 2013. **43**(9): p. 1273-1285.
57. Yang, W., et al., *3D Mechanical properties of the layered esophagus: experiment and constitutive model.* Journal of biomechanical engineering, 2006. **128**(6): p. 899-908.
58. Tang, D.D. and B.D. Gerlach, *The roles and regulation of the actin cytoskeleton, intermediate filaments and microtubules in smooth muscle cell migration.* Respiratory Research, 2017. **18**(1): p. 54.
59. Huber, F., et al., *Emergent complexity of the cytoskeleton: from single filaments to tissue.* Advances in physics, 2013. **62**(1): p. 1-112.
60. Ingber, D.E., *Fibronectin controls capillary endothelial cell growth by modulating cell shape.* Proceedings of the National Academy of Sciences of the United States of America, 1990. **87**(9): p. 3579-3583.
61. Collinsworth, A.M., et al., *Apparent elastic modulus and hysteresis of skeletal muscle cells throughout differentiation.* American Journal of Physiology-Cell Physiology, 2002. **283**(4): p. C1219-C1227.
62. Jacob, J.A., J.M.M. Salmani, and B. Chen, *Magnetic nanoparticles: mechanistic studies on the cancer cell interaction.* Nanotechnology Reviews, 2016. **5**(5): p. 481-488.
63. Pelling, A.E. and M.A. Horton, *An historical perspective on cell mechanics.* Pflügers Archiv - European Journal of Physiology, 2008. **456**(1): p. 3-12.
64. Chen, C.S., et al., *Geometric Control of Cell Life and Death.* Science, 1997. **276**(5317): p. 1425.
65. Mohammad, F., et al., *Targeted hyperthermia-induced cancer cell death by superparamagnetic iron oxide nanoparticles conjugated to luteinizing hormone-releasing hormone.* Nanotechnology Reviews, 2014. **3**(4): p. 389-400.
66. Katoh, K., et al., *Isolation and Contraction of the Stress Fiber.* Molecular Biology of the Cell, 1998. **9**(7): p. 1919-1938.
67. Deguchi, S., T. Ohashi, and M. Sato, *Tensile properties of single stress fibers isolated from cultured vascular smooth muscle cells.* Journal of Biomechanics, 2006. **39**(14): p. 2603-2610.
68. Liu, X. and G.H. Pollack, *Mechanics of F-actin characterized with microfabricated cantilevers.* Biophysical Journal, 2002. **83**(5): p. 2705-2715.
69. Tsuda, Y., et al., *Torsional rigidity of single actin filaments and actin–actin bond breaking force under torsion measured directly by in vitro micromanipulation.* Proceedings of the National Academy of Sciences of the United States of America, 1996. **93**(23): p. 12937-12942.
70. Etienne-Manneville, S., *Actin and Microtubules in Cell Motility: Which One is in Control?* Traffic, 2004. **5**(7): p. 470-477.
71. Nagayama, K. and T. Matsumoto, *Dynamic Change in Morphology and Traction Forces at Focal Adhesions in Cultured Vascular Smooth Muscle Cells During Contraction.* Cellular and Molecular Bioengineering, 2011. **4**(3): p. 348-357.
72. Nagayama, K. and T. Matsumoto, *Contribution of actin filaments and microtubules to quasi-in situ tensile properties and internal force balance of cultured smooth muscle cells on a substrate.* American Journal of Physiology-Cell Physiology, 2008. **295**(6): p. C1569-C1578.
73. Nogales, E., *Structural Insights into Microtubule Function.* Annual Review of Biochemistry, 2000. **69**(1): p. 277-302.

74. Gittes, F., et al., *Flexural rigidity of microtubules and actin filaments measured from thermal fluctuations in shape.* The Journal of Cell Biology, 1993. **120**(4): p. 923.
75. Reilein, A. and W.J. Nelson, *APC is a component of an organizing template for cortical microtubule networks.* Nature Cell Biology, 2005. **7**(5): p. 463-473.
76. Goldman, R.D., *THE ROLE OF THREE CYTOPLASMIC FIBERS IN BHK-21 CELL MOTILITY : I. Microtubules and the Effects of Colchicine.* The Journal of Cell Biology, 1971. **51**(3): p. 752-762.
77. Kato, K., et al., *Microtubule-dependent balanced cell contraction and luminal-matrix modification accelerate epithelial tube fusion.* Nature Communications, 2016. **7**: p. 11141.
78. Zhang, D., et al., *Influence of microtubules on vascular smooth muscle contraction.* Journal of Muscle Research & Cell Motility, 2000. **21**(3): p. 293-300.
79. Liu, B.P., M. Chrzanowska-Wodnicka, and K. Burridge, *Microtubule depolymerization induces stress fibers, focal adhesions, and DNA synthesis via the GTP-binding protein Rho.* Cell adhesion and communication, 1998. **5**(4): p. 249-255.
80. Chang, L. and R.D. Goldman, *Intermediate filaments mediate cytoskeletal crosstalk.* Nature Reviews Molecular Cell Biology, 2004. **5**: p. 601.
81. Li, Q.-F., et al., *Critical role of vimentin phosphorylation at Ser-56 by p21-activated kinase (PAK) in vimentin cytoskeleton signaling.* The Journal of biological chemistry, 2006. **281**(45): p. 34716-34724.
82. Fuchs, E. and K. Weber, *Intermediate Filaments: Structure, Dynamics, Function and Disease.* Annual Review of Biochemistry, 1994. **63**(1): p. 345-382.
83. Wede, O.K., et al., *Mechanical function of intermediate filaments in arteries of different size examined using desmin deficient mice.* The Journal of Physiology, 2002. **540**(Pt 3): p. 941-949.
84. Guzmán, C., et al., *Exploring the Mechanical Properties of Single Vimentin Intermediate Filaments by Atomic Force Microscopy.* Journal of Molecular Biology, 2006. **360**(3): p. 623-630.
85. Wang, N. and D. Stamenovic, *Contribution of intermediate filaments to cell stiffness, stiffening, and growth.* American Journal of Physiology-Cell Physiology, 2000. **279**(1): p. C188-C194.
86. Green, K.J., et al., *The relationship between intermediate filaments and microfilaments before and during the formation of desmosomes and adherens-type junctions in mouse epidermal keratinocytes.* The Journal of cell biology, 1987. **104**(5): p. 1389-1402.
87. Humphrey, J.D., E.R. Dufresne, and M.A. Schwartz, *Mechanotransduction and extracellular matrix homeostasis.* Nature reviews Molecular cell biology, 2014. **15**(12): p. 802.
88. Raines, E.W., *The extracellular matrix can regulate vascular cell migration, proliferation, and survival: relationships to vascular disease.* International Journal of Experimental Pathology, 2000. **81**(3): p. 173-182.
89. Bendeck, M.P., et al., *Smooth muscle cell matrix metalloproteinase production is stimulated via αvβ3 integrin.* Arteriosclerosis, thrombosis, and vascular biology, 2000. **20**(6): p. 1467-1472.
90. Hedin, U. and J. Thyberg, *Plasma fibronectin promotes modulation of arterial smooth-muscle cells from contractile to synthetic phenotype.* Differentiation, 1987. **33**(3): p. 239-246.
91. Sazonova, O.V., et al., *Extracellular matrix presentation modulates vascular smooth muscle cell mechanotransduction.* Matrix Biology, 2015. **41**: p. 36-43.

92. Isenberg, B.C., et al., *Vascular Smooth Muscle Cell Durotaxis Depends on Substrate Stiffness Gradient Strength.* Biophysical Journal, 2009. **97**(5): p. 1313-1322.
93. Wong, J.Y., et al., *Directed movement of vascular smooth muscle cells on gradient-compliant hydrogels.* Langmuir, 2003. **19**(5): p. 1908-1913.
94. Hartman, C.D., et al., *Vascular smooth muscle cell durotaxis depends on extracellular matrix composition.* Proceedings of the National Academy of Sciences, 2016. **113**(40): p. 11190.
95. Timraz, S.B.H., et al., *Stiffness of Extracellular Matrix Components Modulates the Phenotype of Human Smooth Muscle Cells in Vitro and Allows for the Control of Properties of Engineered Tissues.* Procedia Engineering, 2015. **110**: p. 29-36.
96. Qin, H., et al., *Effects of Extracellular Matrix on Phenotype Modulation and MAPK Transduction of Rat Aortic Smooth Muscle Cells in Vitro.* Experimental and Molecular Pathology, 2000. **69**(2): p. 79-90.
97. Morrow, D., et al., *Cyclic strain inhibits Notch receptor signaling in vascular smooth muscle cells in vitro.* Circulation research, 2005. **96**(5): p. 567-575.
98. Ritchie, A.C., et al., *Dependence of alignment direction on magnitude of strain in esophageal smooth muscle cells.* Biotechnology and Bioengineering, 2008. **102**(6): p. 1703-1711.
99. Lin, S., et al., *Eigenstrain as a mechanical set-point of cells.* Biomechanics and Modeling in Mechanobiology, 2018. **17**(4): p. 951-959.
100. Floren, M. and W. Tan, *Three-dimensional, soft neotissue arrays as high throughput platforms for the interrogation of engineered tissue environments.* Biomaterials, 2015. **59**: p. 39-52.
101. Svenja, H., et al., *In vitro elastogenesis: instructing human vascular smooth muscle cells to generate an elastic fiber-containing extracellular matrix scaffold.* Biomedical Materials, 2015. **10**(3): p. 034102.
102. Katja, H., et al., *Bioink properties before, during and after 3D bioprinting.* Biofabrication, 2016. **8**(3): p. 032002.
103. Chen, L.J., S.Y. Wei, and J.J. Chiu, *Mechanical regulation of epigenetics in vascular biology and pathobiology.* Journal of cellular and molecular medicine, 2013. **17**(4): p. 437-448.
104. Lin, S., et al., *Fluid-Structure Interaction in Abdominal Aortic Aneurysm: Effect of Modeling Techniques.* BioMed Research International, 2017. **2017**: p. 10.
105. Schad, J.F., et al., *Cyclic strain upregulates VEGF and attenuates proliferation of vascular smooth muscle cells.* Vascular Cell, 2011(1): p. 21%V 3.
106. Birukov, K.G., et al., *Stretch affects phenotype and proliferation of vascular smooth muscle cells.* Molecular and Cellular Biochemistry, 1995. **144**(2): p. 131-139.
107. Leung, D.Y., S. Glagov, and M.B. Mathews, *Cyclic stretching stimulates synthesis of matrix components by arterial smooth muscle cells in vitro.* Science, 1976. **191**(4226): p. 475.
108. Nakamachi, E., et al., *Multi-scale finite element analyses for stress and strain evaluations of braid fibril artificial blood vessel and smooth muscle cell.* International Journal for Numerical Methods in Biomedical Engineering, 2014. **30**(8): p. 796-813.
109. Colombo, A., et al., *Cyclic strain amplitude dictates the growth response of vascular smooth muscle cells in vitro: role in in-stent restenosis and inhibition with a sirolimus drug-eluting stent.* Biomechanics and Modeling in Mechanobiology, 2013. **12**(4): p. 671-683.
110. Reusch, P., et al., *Mechanical strain increases smooth muscle and decreases nonmuscle myosin expression in rat vascular smooth muscle cells.* Circulation research, 1996. **79**(5): p. 1046-1053.

111. Qu, M.J., et al., *Frequency-Dependent Phenotype Modulation of Vascular Smooth Muscle Cells under Cyclic Mechanical Strain.* Journal of Vascular Research, 2007. **44**(5): p. 345-353.
112. Sharifpoor, S., et al., *Functional characterization of human coronary artery smooth muscle cells under cyclic mechanical strain in a degradable polyurethane scaffold.* Biomaterials, 2011. **32**(21): p. 4816-4829.
113. Sharifpoor, S., et al., *A study of vascular smooth muscle cell function under cyclic mechanical loading in a polyurethane scaffold with optimized porosity.* Acta Biomaterialia, 2010. **6**(11): p. 4218-4228.
114. Stegemann, J.P. and R.M. Nerem, *Phenotype Modulation in Vascular Tissue Engineering Using Biochemical and Mechanical Stimulation.* Annals of Biomedical Engineering, 2003. **31**(4): p. 391-402.
115. Tock, J., et al., *Induction of SM-α-actin expression by mechanical strain in adult vascular smooth muscle cells is mediated through activation of JNK and p38 MAP kinase.* Biochemical and Biophysical Research Communications, 2003. **301**(4): p. 1116-1121.
116. Solan, A., S.L.M. Dahl, and L.E. Niklason, *Effects of Mechanical Stretch on Collagen and Cross-Linking in Engineered Blood Vessels.* Cell Transplantation, 2009. **18**(8): p. 915-921.
117. Bono, N., et al., *Unraveling the role of mechanical stimulation on smooth muscle cells: A comparative study between 2D and 3D models.* Biotechnology and Bioengineering, 2016. **113**(10): p. 2254-2263.
118. Matsumoto, T. and K. Nagayama, *Tensile properties of vascular smooth muscle cells: Bridging vascular and cellular biomechanics.* Journal of Biomechanics, 2012. **45**(5): p. 745-755.
119. Lin, S., et al., *Active stiffening of F-actin network dominated by structural transition of actin filaments into bundles.* Composites Part B: Engineering, 2017. **116**: p. 377-381.
120. Barreto-Ortiz, S.F., et al., *Fabrication of 3-dimensional multicellular microvascular structures.* The FASEB Journal, 2015. **29**(8): p. 3302-3314.
121. Baker, B.M., et al., *Cell-mediated fibre recruitment drives extracellular matrix mechanosensing in engineered fibrillar microenvironments.* Nature materials, 2015. **14**(12): p. 1262.
122. Ding, Y., et al., *Biomimetic soft fibrous hydrogels for contractile and pharmacologically responsive smooth muscle.* Acta Biomaterialia, 2018. **74**: p. 121-130.
123. Thunes, J.R., et al., *A structural finite element model for lamellar unit of aortic media indicates heterogeneous stress field after collagen recruitment.* Journal of Biomechanics, 2016. **49**(9): p. 1562-1569.
124. Phillippi, J.A., et al., *Mechanism of aortic medial matrix remodeling is distinct in patients with bicuspid aortic valve.* The Journal of Thoracic and Cardiovascular Surgery, 2014. **147**(3): p. 1056-1064.
125. Beenakker, J.-W.M., et al., *Mechanical properties of the extracellular matrix of the aorta studied by enzymatic treatments.* Biophysical journal, 2012. **102**(8): p. 1731-1737.
126. O'Connell, M.K., et al., *The Three-Dimensional Micro- and Nanostructure of the Aortic Medial Lamellar Unit Measured Using 3D Confocal & Electron Microscopy Imaging.* Matrix biology : journal of the International Society for Matrix Biology, 2008. **27**(3): p. 171-181.
127. Nagayama, K. and T. Matsumoto, *Mechanical Anisotropy of Rat Aortic Smooth Muscle Cells Decreases with Their Contraction (Possible Effect of Actin Filament Orientation).* JSME International Journal Series C Mechanical Systems, Machine Elements and Manufacturing, 2004. **47**(4): p. 985-991.

128. Roeder, B.A., et al., *Tensile Mechanical Properties of Three-Dimensional Type I Collagen Extracellular Matrices With Varied Microstructure.* Journal of Biomechanical Engineering, 2002. **124**(2): p. 214-222.
129. Wagenseil, J.E. and R.P. Mecham, *Elastin in Large Artery Stiffness and Hypertension.* Journal of Cardiovascular Translational Research, 2012. **5**(3): p. 264-273.
130. Sugita, S. and T. Matsumoto, *Multiphoton microscopy observations of 3D elastin and collagen fiber microstructure changes during pressurization in aortic media.* Biomechanics and Modeling in Mechanobiology, 2017. **16**(3): p. 763-773.
131. Lin, S. and L. Gu, *Contribution of Fiber Undulation to Mechanics of Three-Dimensional Collagen-I Gel.* Macromolecular Symposia, 2016. **365**(1): p. 112-117.
132. Carta, L., et al., *Discrete contributions of elastic fiber components to arterial development and mechanical compliance.* Arteriosclerosis, thrombosis, and vascular biology, 2009. **29**(12): p. 2083.
133. Szabo, Z., et al., *Aortic aneurysmal disease and cutis laxa caused by defects in the elastin gene.* Journal of Medical Genetics, 2006. **43**(3): p. 255-258.
134. Zhao, S. and L. Gu, *Implementation and Validation of Aortic Remodeling in Hypertensive Rats.* Journal of Biomechanical Engineering, 2014. **136**(9): p. 091007-091007-8.
135. Faury, G., et al., *Developmental adaptation of the mouse cardiovascular system to elastin haploinsufficiency.* The Journal of clinical investigation, 2003. **112**(9): p. 1419-1428.
136. Hirano, E., et al., *Functional rescue of elastin insufficiency in mice by the human elastin gene: implications for mouse models of human disease.* Circulation research, 2007. **101**(5): p. 523-531.
137. Wagenseil, J.E., et al., *Elastin-insufficient mice show normal cardiovascular remodeling in 2K1C hypertension despite higher baseline pressure and unique cardiovascular architecture.* American Journal of Physiology-Heart and Circulatory Physiology, 2007. **293**(1): p. H574-H582.
138. Wagenseil, J.E., et al., *Effects of elastin haploinsufficiency on the mechanical behavior of mouse arteries.* American Journal of Physiology-Heart and Circulatory Physiology, 2005. **289**(3): p. H1209-H1217.
139. Aronson, D., *Cross-linking of glycated collagen in the pathogenesis of arterial and myocardial stiffening of aging and diabetes.* Journal of Hypertension, 2003. **21**(1): p. 3-12.
140. Konova, E., et al., *Age-related changes in the glycation of human aortic elastin.* Experimental Gerontology, 2004. **39**(2): p. 249-254.
141. Lin, S., et al., *Towards Tuning the Mechanical Properties of Three-Dimensional Collagen Scaffolds Using a Coupled Fiber-Matrix Model.* Materials (Basel, Switzerland), 2015. **8**(8): p. 5376-5384.
142. Lin, S. and L. Gu, *Influence of Crosslink Density and Stiffness on Mechanical Properties of Type I Collagen Gel.* Materials (Basel, Switzerland), 2015. **8**(2): p. 551-560.
143. Bezie, Y., et al., *Connection of smooth muscle cells to elastic lamellae in aorta of spontaneously hypertensive rats.* Hypertension, 1998. **32**(1): p. 166-169.
144. Koffi, I., et al., *Prevention of arterial structural alterations with verapamil and trandolapril and consequences for mechanical properties in spontaneously hypertensive rats.* European journal of pharmacology, 1998. **361**(1): p. 51-60.
145. Sehgel, N.L., et al., *Augmented vascular smooth muscle cell stiffness and adhesion when hypertension is superimposed on aging.* Hypertension, 2015. **65**(2): p. 370.

146. van Gorp, A.W., et al., *In spontaneously hypertensive rats alterations in aortic wall properties precede development of hypertension.* American Journal of Physiology-Heart and Circulatory Physiology, 2000. **278**(4): p. H1241-H1247.
147. Cox, R.H., *Basis for the altered arterial wall mechanics in the spontaneously hypertensive rat.* Hypertension, 1981. **3**(4): p. 485-495.
148. Mizutani, K., et al., *Biomechanical properties and chemical composition of the aorta in genetic hypertensive rats.* Journal of hypertension, 1999. **17**(4): p. 481-487.
149. Hu, J.-J., et al., *Time Courses of Growth and Remodeling of Porcine Aortic Media During Hypertension: A Quantitative Immunohistochemical Examination.* Journal of Histochemistry and Cytochemistry, 2008. **56**(4): p. 359-370.
150. Sehgel, N.L., S.F. Vatner, and G.A. Meininger, *"Smooth Muscle Cell Stiffness Syndrome"—Revisiting the Structural Basis of Arterial Stiffness.* Frontiers in Physiology, 2015. **6**(335).
151. Sehgel, N.L., et al., *Increased vascular smooth muscle cell stiffness: a novel mechanism for aortic stiffness in hypertension.* American Journal of Physiology-Heart and Circulatory Physiology, 2013. **305**(9): p. H1281-H1287.
152. Zhu, Y., et al., *Temporal analysis of vascular smooth muscle cell elasticity and adhesion reveals oscillation waveforms that differ with aging.* Aging cell, 2012. **11**(5): p. 741-750.
153. Campbell, G.R. and J.H. Campbell, - *Development of the Vessel Wall: Overview*, in *The Vascular Smooth Muscle Cell*, S.M. Schwartz and R.P. Mecham, Editors. 1995, Academic Press: San Diego. p. 1-15.
154. Warshaw, D.M., et al., *Pharmacology and force development of single freshly isolated bovine carotid artery smooth muscle cells.* Circ Res, 1986. **58**(3): p. 399-406.
155. Matsumoto, T., et al., *Smooth muscle cells freshly isolated from rat thoracic aortas are much stiffer than cultured bovine cells: possible effect of phenotype.* JSME International Journal Series C Mechanical Systems, Machine Elements and Manufacturing, 2000. **43**(4): p. 867-874.
156. Smith, P.G., et al., *Selected contribution: mechanical strain increases force production and calcium sensitivity in cultured airway smooth muscle cells.* Journal of applied physiology, 2000. **89**(5): p. 2092-2098.
157. Thoumine, O. and A. Ott, *Time scale dependent viscoelastic and contractile regimes in fibroblasts probed by microplate manipulation.* Journal of cell science, 1997. **110**(17): p. 2109-2116.
158. Xu, C., et al., *Molecular mechanisms of aortic wall remodeling in response to hypertension.* Journal of Vascular Surgery, 2001. **33**(3): p. 570-578.
159. Matsumoto, T., et al., *Effects of hypertension on morphological, contractile and mechanical properties of rat aortic smooth muscle cells.* Cellular and Molecular Bioengineering, 2011. **4**(3): p. 340-347.
160. Tosun, Z. and P.S. McFetridge, *Variation in Cardiac Pulse Frequencies Modulates vSMC Phenotype Switching During Vascular Remodeling.* Cardiovascular Engineering and Technology, 2015. **6**(1): p. 59-70.
161. Owens, G.K., M.S. Kumar, and B.R. Wamhoff, *Molecular regulation of vascular smooth muscle cell differentiation in development and disease.* Physiological reviews, 2004. **84**(3): p. 767-801.
162. Gundiah, N., M. B Ratcliffe, and L. A Pruitt, *Determination of strain energy function for arterial elastin: Experiments using histology and mechanical tests.* Journal of Biomechanics, 2007. **40**(3): p. 586-594.
163. Gundiah, N., M.B. Ratcliffe, and L.A. Pruitt, *The biomechanics of arterial elastin.* Journal of the Mechanical Behavior of Biomedical Materials, 2009. **2**(3): p. 288-296.

164. Lillie, M.A., R.E. Shadwick, and J.M. Gosline, *Mechanical anisotropy of inflated elastic tissue from the pig aorta.* Journal of Biomechanics, 2010. **43**(11): p. 2070-2078.
165. Zou, Y. and Y. Zhang, *An Experimental and Theoretical Study on the Anisotropy of Elastin Network.* Annals of Biomedical Engineering, 2009. **37**(8): p. 1572-1583.
166. Zou, Y. and Y. Zhang, *The orthotropic viscoelastic behavior of aortic elastin.* Biomechanics and Modeling in Mechanobiology, 2011. **10**(5): p. 613-625.
167. Weisbecker, H., et al., *The role of elastin and collagen in the softening behavior of the human thoracic aortic media.* Journal of Biomechanics, 2013. **46**(11): p. 1859-1865.
168. Martinez, R. and H.-C. Han, *THE EFFECT OF COLLAGENASE ON THE CRITICAL BUCKLING PRESSURE OF ARTERIES.* Molecular & cellular biomechanics : MCB, 2012. **9**(1): p. 55-75.
169. Dobrin, P.B. and T.R. Canfield, *Elastase, collagenase, and the biaxial elastic properties of dog carotid artery.* American Journal of Physiology-Heart and Circulatory Physiology, 1984. **247**(1): p. H124-H131.
170. Dobrin, P.B., T. Schwarcz, and W. Baker, *Mechanisms of arterial and aneurysmal tortuosity.* Surgery, 1988. **104**(3): p. 568-571.
171. Kochová, P., et al., *The contribution of vascular smooth muscle, elastin and collagen on the passive mechanics of porcine carotid arteries.* Physiological Measurement, 2012. **33**(8): p. 1335.
172. Kiousis, D.E., et al., *A Methodology to Analyze Changes in Lipid Core and Calcification Onto Fibrous Cap Vulnerability: The Human Atherosclerotic Carotid Bifurcation as an Illustratory Example.* Journal of Biomechanical Engineering, 2009. **131**(12): p. 121002-121002-9.
173. Kock, S.A., et al., *Mechanical stresses in carotid plaques using MRI-based fluid–structure interaction models.* Journal of biomechanics, 2008. **41**(8): p. 1651-1658.
174. Holzapfel, G.A. and R.W. Ogden, *Modelling the layer-specific three-dimensional residual stresses in arteries, with an application to the human aorta.* Journal of The Royal Society Interface, 2009.
175. Delfino, A., et al., *Residual strain effects on the stress field in a thick wall finite element model of the human carotid bifurcation.* Journal of Biomechanics, 1997. **30**(8): p. 777-786.
176. Holzapfel, G.A., T.C. Gasser, and R.W. Ogden, *A new constitutive framework for arterial wall mechanics and a comparative study of material models.* Journal of elasticity and the physical science of solids, 2000. **61**(1-3): p. 1-48.
177. Kural, M.H., et al., *Planar biaxial characterization of diseased human coronary and carotid arteries for computational modeling.* Journal of biomechanics, 2012. **45**(5): p. 790-798.
178. Taber, L.A. and J.D. Humphrey, *Stress-modulated growth, residual stress, and vascular heterogeneity.* Journal of biomechanical engineering, 2001. **123**(6): p. 528-535.
179. Yamada, H., et al., *Age-related distensibility and histology of the ascending aorta in elderly patients with acute aortic dissection.* Journal of biomechanics, 2015. **48**(12): p. 3267-3273.
180. Masson, I., et al., *Carotid artery mechanical properties and stresses quantified using in vivo data from normotensive and hypertensive humans.* Biomechanics and modeling in mechanobiology, 2011. **10**(6): p. 867-882.
181. Peterson, S. and R. Okamoto, *Effect of residual stress and heterogeneity on circumferential stress in the arterial wall.* Journal of biomechanical engineering, 2000. **122**(4): p. 454-456.
182. Sommer, G. and G.A. Holzapfel, *3D constitutive modeling of the biaxial mechanical response of intact and layer-dissected human carotid arteries.* Journal of the mechanical behavior of biomedical materials, 2012. **5**(1): p. 116-128.

183. Von Maltzahn, W.-W., D. Besdo, and W. Wiemer, *Elastic properties of arteries: a nonlinear two-layer cylindrical model.* Journal of Biomechanics, 1981. **14**(6): p. 389-397.
184. Hudson, J., *Overall properties of heterogeneous material.* Geophysical journal international, 1991. **107**(3): p. 505-511.
185. Oren, T., *Analytical and numerical analyses of the micromechanics of soft fibrous connective tissues.* Biomechanics and modeling in mechanobiology, 2013. **12**(1): p. 151-166.
186. Lake, S.P., et al., *Mechanics of a Fiber Network Within a Non-Fibrillar Matrix: Model and Comparison with Collagen-Agarose Co-gels.* Annals of Biomedical Engineering, 2012. **40**(10): p. 2111-2121.
187. Stein, A.M., et al., *The micromechanics of three-dimensional collagen-I gels.* Complexity, 2010. **16**(4): p. 22-28.
188. Lukeš, V. and E. Rohan, *Microstructure based two-scale modelling of soft tissues.* Mathematics and Computers in Simulation, 2010. **80**(6): p. 1289-1301.
189. Lindeman, J.H.N., et al., *Distinct defects in collagen microarchitecture underlie vessel-wall failure in advanced abdominal aneurysms and aneurysms in Marfan syndrome.* Proceedings of the National Academy of Sciences of the United States of America, 2010. **107**(2): p. 862-865.
190. López-Guimet, J., et al., *High-Resolution Morphological Approach to Analyse Elastic Laminae Injuries of the Ascending Aorta in a Murine Model of Marfan Syndrome.* Scientific Reports, 2017. **7**(1): p. 1505.
191. Abraham, P.A., et al., *Marfan syndrome. Demonstration of abnormal elastin in aorta.* The Journal of Clinical Investigation, 1982. **70**(6): p. 1245-1252.
192. Tsamis, A., J.T. Krawiec, and D.A. Vorp, *Elastin and collagen fibre microstructure of the human aorta in ageing and disease: a review.* Journal of The Royal Society Interface, 2013. **10**(83).
193. Mozaffarian, D., et al., *Heart disease and stroke statistics—2016 update: a report from the American Heart Association.* Circulation, 2015: p. CIR. 0000000000000350.
194. Touyz, R.M., et al., *Vascular smooth muscle contraction in hypertension.* Cardiovascular Research, 2018. **114**(4): p. 529-539.
195. Steucke, K.E., et al., *Empirically Determined Vascular Smooth Muscle Cell Mechano-Adaptation Law.* Journal of Biomechanical Engineering, 2017. **139**(7): p. 0710051-0710059.
196. Tsamis, A., J.T. Krawiec, and D.A. Vorp, *Elastin and collagen fibre microstructure of the human aorta in ageing and disease: a review.* Journal of the Royal Society Interface, 2013. **10**(83): p. 20121004.
197. van Gorp, A.W., et al., *In spontaneously hypertensive rats alterations in aortic wall properties precede development of hypertension.* American Journal of Physiology-Heart and Circulatory Physiology, 2000. **278**(4): p. H1241-H1247.
198. Scott, D., et al., *High pulsatility flow stimulates smooth muscle cell hypertrophy and contractile protein expression.* American Journal of Physiology - Lung Cellular and Molecular Physiology, 2013. **304**(1): p. L70-L81.
199. Wagenseil, J.E. and R.P. Mecham, *Vascular Extracellular Matrix and Arterial Mechanics.* Physiological reviews, 2009. **89**(3): p. 957-989.
200. Bank, A.J. and D.R. Kaiser, *Smooth muscle relaxation: effects on arterial compliance, distensibility, elastic modulus, and pulse wave velocity.* Hypertension, 1998. **32**(2): p. 356-359.

201. Dinardo, C.L., et al., *Variation of mechanical properties and quantitative proteomics of VSMC along the arterial tree.* American Journal of Physiology-Heart and Circulatory Physiology, 2013. **306**(4): p. H505-H516.
202. Holzapfel, G.A., T.C. Gasser, and R.W. Ogden, *Comparison of a Multi-Layer Structural Model for Arterial Walls With a Fung-Type Model, and Issues of Material Stability.* Journal of Biomechanical Engineering, 2004. **126**(2): p. 264-275.
203. Wan, W., J.B. Dixon, and Rudolph L. Gleason, *Constitutive Modeling of Mouse Carotid Arteries Using Experimentally Measured Microstructural Parameters.* Biophysical Journal, 2012. **102**(12): p. 2916-2925.
204. Weisbecker, H., M.J. Unterberger, and G.A. Holzapfel, *Constitutive modelling of arteries considering fibre recruitment and three-dimensional fibre distribution.* Journal of The Royal Society Interface, 2015. **12**(105): p. 20150111.
205. Gasser, T.C., R.W. Ogden, and G.A. Holzapfel, *Hyperelastic modelling of arterial layers with distributed collagen fibre orientations.* Journal of The Royal Society Interface, 2006. **3**(6): p. 15.
206. Ferruzzi, J., D.A. Vorp, and J.D. Humphrey, *On constitutive descriptors of the biaxial mechanical behaviour of human abdominal aorta and aneurysms.* Journal of The Royal Society Interface, 2011. **8**(56): p. 435.
207. O'Connell, M.K., et al., *The three-dimensional micro- and nanostructure of the aortic medial lamellar unit measured using 3D confocal and electron microscopy imaging.* Matrix Biology, 2008. **27**(3): p. 171-181.
208. Chow, M.-J., et al., *Arterial Extracellular Matrix: A Mechanobiological Study of the Contributions and Interactions of Elastin and Collagen.* Biophysical Journal, 2014. **106**(12): p. 2684-2692.
209. Koch, R.G., et al., *A custom image-based analysis tool for quantifying elastin and collagen micro-architecture in the wall of the human aorta from multi-photon microscopy.* Journal of Biomechanics, 2014. **47**(5): p. 935-943.
210. Fung, C., *Biomechanics'. Mechanical Properties of Living Tissue. Springer: Berlin, 1981.*
211. Miyazaki, H. and K. Hayashi, *Tensile Tests of Collagen Fibers Obtained from the Rabbit Patellar Tendon.* Biomedical Microdevices, 1999. **2**(2): p. 151-157.
212. Zulliger, M.A. and N. Stergiopulos, *Structural strain energy function applied to the ageing of the human aorta.* Journal of Biomechanics, 2007. **40**(14): p. 3061-3069.
213. Pasta, S., et al., *Difference in hemodynamic and wall stress of ascending thoracic aortic aneurysms with bicuspid and tricuspid aortic valve.* Journal of Biomechanics, 2013. **46**(10): p. 1729-1738.
214. Esmaeili Monir, H., H. Yamada, and N. Sakata, *Finite element modelling of the common carotid artery in the elderly with physiological intimal thickening using layer-specific stress-released geometries and nonlinear elastic properties.* Computer Methods in Biomechanics and Biomedical Engineering, 2016. **19**(12): p. 1286-1296.
215. Lacolley, P., V. Regnault, and A.P. Avolio, *Smooth muscle cell and arterial aging: basic and clinical aspects.* Cardiovascular Research, 2018. **114**(4): p. 513-528.
216. Wang, X., et al., *3D printing of polymer matrix composites: A review and prospective.* Composites Part B: Engineering, 2017. **110**: p. 442-458.
217. Nikzad, M., S.H. Masood, and I. Sbarski, *Thermo-mechanical properties of a highly filled polymeric composites for Fused Deposition Modeling.* Materials & Design, 2011. **32**(6): p. 3448-3456.

218. Boparai, K., R. Singh, and H. Singh, *Comparison of tribological behaviour for Nylon6-Al-Al2O3 and ABS parts fabricated by fused deposition modelling.* Virtual and Physical Prototyping, 2015. **10**(2): p. 59-66.
219. Shemelya, C.M., et al., *Mechanical, Electromagnetic, and X-ray Shielding Characterization of a 3D Printable Tungsten–Polycarbonate Polymer Matrix Composite for Space-Based Applications.* Journal of Electronic Materials, 2015. **44**(8): p. 2598-2607.
220. Fu, S.-Y., et al., *Effects of particle size, particle/matrix interface adhesion and particle loading on mechanical properties of particulate–polymer composites.* Composites Part B: Engineering, 2008. **39**(6): p. 933-961.
221. Segurado, J. and J. Llorca, *Computational micromechanics of composites: The effect of particle spatial distribution.* Mechanics of Materials, 2006. **38**(8): p. 873-883.
222. Tekce, H.S., D. Kumlutas, and I.H. Tavman, *Effect of Particle Shape on Thermal Conductivity of Copper Reinforced Polymer Composites.* Journal of Reinforced Plastics and Composites, 2007. **26**(1): p. 113-121.
223. Zhang, W.X., L.X. Li, and T.J. Wang, *Interphase effect on the strengthening behavior of particle-reinforced metal matrix composites.* Computational Materials Science, 2007. **41**(2): p. 145-155.
224. Reddy, A.C. *Effect of CTE and Stiffness Mismatches on Interphase and Particle Fractures of Zirconium Carbide/AA5050 Alloy Particle-Reinforced Composites*. in *3rd International Conference on Composite Materials and Characterization, Chennai, India*. 2001.
225. *The determination of the elastic field of an ellipsoidal inclusion, and related problems.* Proceedings of the Royal Society of London. Series A. Mathematical and Physical Sciences, 1957. **241**(1226): p. 376-396.
226. Hashin, Z. and B.W. Rosen, *The Elastic Moduli of Fiber-Reinforced Materials.* Journal of Applied Mechanics, 1964. **31**(2): p. 223-232.
227. Lutz, M.P. and R.W. Zimmerman, *Effect of the Interphase Zone on the Bulk Modulus of a Particulate Composite.* Journal of Applied Mechanics, 1996. **63**(4): p. 855-861.
228. Cheng, Y.-T. and C.-M. Cheng, *Scaling, dimensional analysis, and indentation measurements.* Materials Science and Engineering: R: Reports, 2004. **44**(4): p. 91-149.
229. Hodzic, A., Z.H. Stachurski, and J.K. Kim, *Nano-indentation of polymer–glass interfaces Part I. Experimental and mechanical analysis.* Polymer, 2000. **41**(18): p. 6895-6905.
230. Gao, S.-L. and E. Mäder, *Characterisation of interphase nanoscale property variations in glass fibre reinforced polypropylene and epoxy resin composites.* Composites Part A: Applied Science and Manufacturing, 2002. **33**(4): p. 559-576.
231. Ureña, A., et al., *Oxidation treatments for SiC particles used as reinforcement in aluminium matrix composites.* Composites Science and Technology, 2004. **64**(12): p. 1843-1854.
232. Torralba, J.M., et al., *Mechanical behaviour of the interphase between matrix and reinforcement of Al 2014 matrix composites reinforced with (Ni3Al)p.* Composites Part A: Applied Science and Manufacturing, 2002. **33**(3): p. 427-434.
233. P., M.A., O. Kristiina, and S. Mohini, *Mechanical properties of biodegradable composites from poly lactic acid (PLA) and microcrystalline cellulose (MCC).* Journal of Applied Polymer Science, 2005. **97**(5): p. 2014-2025.
234. Yamaguchi, S., et al., *Multi-scale analysis of the effect of nano-filler particle diameter on the physical properties of CAD/CAM composite resin blocks.* Computer Methods in Biomechanics and Biomedical Engineering, 2017. **20**(7): p. 714-719.
235. Shan, D., L. Yuan, and B. Guo, *Multiscale simulation of surface step effects on nanoindentation.* Materials Science and Engineering: A, 2005. **412**(1): p. 264-270.

236. Klinger, L. and E. Rabkin, *Theory of nanoindentation creep controlled by interfacial diffusion.* Scripta Materialia, 2003. **48**(10): p. 1475-1481.
237. Jiang, W.-G., J.-J. Su, and X.-Q. Feng, *Effect of surface roughness on nanoindentation test of thin films.* Engineering Fracture Mechanics, 2008. **75**(17): p. 4965-4972.
238. Cifuentes, S.C., et al., *Assessment of mechanical behavior of PLA composites reinforced with Mg micro-particles through depth-sensing indentations analysis.* Journal of the Mechanical Behavior of Biomedical Materials, 2017. **65**: p. 781-790.
239. Díez-Pascual, A.M., et al., *Nanoindentation in polymer nanocomposites.* Progress in Materials Science, 2015. **67**: p. 1-94.
240. Monclus, M.A. and N.M. Jennett, *In search of validated measurements of the properties of viscoelastic materials by indentation with sharp indenters.* Philosophical Magazine, 2011. **91**(7-9): p. 1308-1328.
241. Cifuentes, S.C., et al., *Effect of Mg content on the thermal stability and mechanical behaviour of PLLA/Mg composites processed by hot extrusion.* Materials Science and Engineering: C, 2017. **72**: p. 18-25.
242. Cifuentes, S.C., et al., *Effect of Mg content on the thermal stability and mechanical behaviour of PLLA/Mg composites processed by hot extrusion.* Materials Science and Engineering: C, 2017. **72**: p. 18-25.
243. Yang, L., et al., *Micromechanical modelling and simulation of unidirectional fibre-reinforced composite under shear loading.* Journal of Reinforced Plastics and Composites, 2014. **34**(1): p. 72-83.
244. Chen, J.-k., et al., *Critical particle size for interfacial debonding in polymer/nanoparticle composites.* Composites Science and Technology, 2010. **70**(5): p. 861-872.
245. Kushch, V.I., et al., *Numerical simulation of progressive debonding in fiber reinforced composite under transverse loading.* International Journal of Engineering Science, 2011. **49**(1): p. 17-29.
246. Mori, T. and K. Tanaka, *Average stress in matrix and average elastic energy of materials with misfitting inclusions.* Acta Metallurgica, 1973. **21**(5): p. 571-574.
247. Tan, H., et al., *The uniaxial tension of particulate composite materials with nonlinear interface debonding.* International Journal of Solids and Structures, 2007. **44**(6): p. 1809-1822.